

Ultrafast Quantum-Classical Dynamics: Applications in X-ray Spectroscopy and Method Development

Dissertation
zur Erlangung des Doktorgrades
an der Fakultät für Mathematik, Informatik und Naturwissenschaften
Fachbereich Physik
der Universität Hamburg

vorgelegt von
Yashoj Shakya

Hamburg
2022

Eidesstattliche Versicherung / Declaration on oath

Hiermit versichere ich an Eides statt, die vorliegende Dissertationsschrift selbst verfasst und keine anderen als die angegebenen Hilfsmittel und Quellen benutzt zu haben.

Hamburg, den

Unterschrift des Doktoranden

Gutachtern der Dissertation:

Prof. Dr. Robin Santra

Dr. Ludger Inhester

Zusammensetzung der Prüfungskommission:

Prof. Dr. Robin Santra

Dr. Ludger Inhester

Prof. Dr. Jochen Küpper

Dr. Mariana Rossi

Prof. Dr. Arwen Pearson

Vorsitzende der Prüfungskommission:

Prof. Dr. Arwen Pearson

Datum der Disputation:

02.12.2022

Vorsitzender Fach-Promotionsausschuss PHYSIK:

Prof. Dr. Wolfgang J. Parak

Leiter des Fachbereichs PHYSIK:

Prof. Dr. Günter H. W. Sigl

Dekan der Fakultät MIN:

Prof. Dr.-Ing. Norbert Ritter

For my mom (nan) and dad.

Abstract

Recent advances in laser technologies such as x-ray free-electron lasers and high harmonic generation have led to ever-shorter light pulses that enable us to probe ultrafast nuclear and electronic dynamics in atoms and molecules. Theoretical quantum dynamics simulations are indispensable in gaining deeper insights into these ultrafast processes. However, treating both electrons and nuclei fully quantum mechanically is computationally not feasible for large systems. Hence, due to their computational efficiency, mixed quantum-classical dynamics methods such as Tully's fewest switches surface hopping (FSSH) have become popular, in spite of their limitations. In this thesis, I demonstrate how FSSH dynamics, combined with advanced statistical analysis techniques, can be used to understand ultrafast phenomena traced in experimental spectra such as time-resolved x-ray absorption spectra (TRXAS). Furthermore, I introduce a new method developed to improve FSSH to provide a better description of electronic coherences relevant in attosecond science.

With the aim of understanding the first steps of radiation damage in biomolecules, the first part of this thesis focuses on *ab initio* FSSH dynamics simulations of valence ionized urea monomer and dimer in vacuum as a prototypical example. Investigating the carbon, nitrogen, and oxygen K-edges in the simulated TRXAS reveals rich insights into the ultrafast processes. Further information is gained by applying machine learning techniques for statistical analysis which unravel uncorrelated collective motions that most influence the spectra. Extending these simulations to urea in aqueous solution, I show in the second part of this thesis how the effect of proton transfer between two hydrogen-bonded ureas and the subsequent electronic structure changes leave two distinct marks on the carbon K-edge of the TRXAS. This enables us to separate the effect of nuclear and electronic motion on the spectra. These liquid phase results are in good agreement with recent pump-probe experiments on aqueous urea.

In the last part, I present a new method, named ring polymer surface hopping - density matrix approach (RPSH-DM), developed to alleviate one of the shortcomings of FSSH, namely the so-called overcoherence problem, which manifests as a poor description of electronic coherence and decoherence phenomena. RPSH-DM combines FSSH with ring polymer molecular dynamics to incorporate decoherence effects by utilizing the spatial extent of the ring polymer, mimicking the width of the nuclear wave packet. By applying this method to a one-dimensional model system, I show how RPSH-DM can capture crucial decoherence mechanisms that are not present in FSSH. In future studies, employing RPSH-DM to investigate polyatomic systems can provide vital insights into ultrafast electronic processes occurring in attosecond experiments.

Zusammenfassung

Fortwährende Entwicklungen im Bereich der Lasertechnologie wie etwa Freie-Elektronen-Röntgenlaser oder die Generierung hoher Harmonischer (*high harmonic generation*) ermöglichen die Erzeugung immer kürzerer Lichtpulse zur Untersuchung ultraschneller nuklearer und elektronischer Dynamiken in Atomen und Molekülen. Numerische Quantendynamiksimulationen sind zum Verständnis dieser ultraschnellen Prozesse unerlässlich. Jedoch ist eine vollständige quantenmechanische Beschreibung sowohl der Elektronen als auch der Atomkerne aufgrund der hohen Komplexität und der für die numerische Simulation benötigten Rechenleistung für große Systeme nicht realisierbar. Methoden wie *Tully's Fewest Switches Surface Hopping* (FSSH) basieren daher auf einer Kombination von klassischer und quantenmechanischer Dynamik und bilden aufgrund ihrer numerischen Effizienz eine populäre, wenngleich mit Einschränkungen einhergehende Alternative. In dieser Arbeit zeige ich, wie die FSSH-Methode und moderne statistische Analysetechniken genutzt werden können, um ultraschnelle Phänomene in Molekülen zu verstehen, die experimentell mit Methoden wie zeitaufgelöster Röntgenabsorptionsspektroskopie (*Time-Resolved X-ray Absorption Spectroscopy*, TRXAS) verfolgt werden können. Darüber hinaus stelle ich eine neue Methode zur Verbesserung von FSSH vor, die eine genauere Beschreibung der in der Attosekundenphysik relevanten elektronischen Kohärenz ermöglicht.

Mit dem Ziel, die zu Strahlenschäden in Biomolekülen führenden initialen Prozesse zu verstehen, konzentriert sich der erste Teil dieser Arbeit exemplarisch auf *ab initio* Dynamiksimulationen mittels FSSH von valenzionisierten Ureamono- und -dimeren im Vakuum. Hierbei offenbaren Untersuchungen der K-Kanten in den simulierten TRXAS-Spektren von Kohlenstoff, Stickstoff und Sauerstoff umfassende Einblicke in die Dynamik der auftretenden ultraschnellen Prozesse. Des Weiteren ermöglicht die Anwendung von Methoden des maschinellen Lernens zur statistischen Analyse die Identifizierung unkorrelierter, kollektiver Bewegungen, die den größten Einfluss auf die simulierten Spektren haben. Durch Ausweitung der Simulationen auf Urea in wässriger Lösung zeige ich im zweiten Teil dieser Arbeit, wie Protonentransfer über eine Wasserstoffbrückenbindung zweier Ureamoleküle zu Änderungen der elektronischen Struktur und dadurch zur Ausprägung von zwei unterschiedlichen Charakteristika an der Kohlenstoff-K-Kante der TRXAS-Spektren führt. Dies ermöglicht eine separate Analyse der Auswirkungen von Kern- und elektronischer Dynamik auf die Spektren. Die erzielten Resultate stehen in guter Übereinstimmung mit entsprechenden Ergebnissen kürzlich *Pump-Probe*-Experimente.

Im letzten Teil stelle ich mit dem *Ring Polymer Surface Hopping - Density Matrix*-Ansatz (RPSH-DM) eine neu entwickelte Methode vor, die mit dem sogenannten Überkohärenzproblem, der fehlerhaften Beschreibung elektronischer Kohärenz- und Dekohärenzphänomene, eine der Schwächen von FSSH behebt. RPSH-DM kombiniert FSSH mit Ringpolymer-Molekulardynamik, um Dekohärenzeffekte einzubeziehen, indem die Breite des Kernwellenpakets durch die räumliche Ausdehnung des Ringpolymers berücksichtigt wird. Anhand eines eindimensionalen Modellsystems zeige ich, wie RPSH-DM im Gegensatz zu FSSH entscheidende Mechanismen der Dekohärenz erfassen kann. In Zukunft kann die Anwendung von RPSH-DM auf polyatomare Systeme wichtige Einblicke in ultraschnelle elektronische Prozesse in Attosekunden-Experimenten liefern.

Acknowledgements

This thesis would not have been possible without the help and support of all of these wonderful people. First of all, I'd like to express my deepest gratitude to my supervisors during my Ph.D.: Dr. Ludger Inhester, Dr. Ralph Welsch and Prof. Dr. Robin Santra for all of their guidance and teachings to finish this beast. And to my external supervisor Prof. Dr. Jochen Küpper for his words of wisdom which always calmed me down during this process. I was lucky to have such supportive colleagues in our extended CFEL-DESY Theory Division (including both groups of Prof. Dr. Robin Santra and Prof. Dr. Beata Ziaja-Motyka) for the rich discussions, helping me out with my issues and of course the friendship over the years. I thank all our group members, and in particular, Benoit Richard, Niels Breckwoldt, Konrad Kapcia, Iwona Ostrowska, Michal Stransky, Mayank Vashistha, Julia Schäfer, Caroline Arnold, Sang-Kil Son, Arturo Sopena and Berit Heiser. I also have to acknowledge the great effort undertaken by our experimental collaborators Dr. Zhong Yin, Dr. Tadas Balčiūnas, Yi-Ping Chang, Prof. Dr. Jean-Pierre Wolf and Prof. Dr. Hans Jakob Wörner for our very productive collaborative projects which quite some significant portion of this thesis is based on. I'm also grateful to Prof. Dr. Nina Rohringer for giving the opportunity to do some teaching, Gisa Günther for being the best and most patient German teacher I have had, our IMPRS graduate school coordinator Dr. Neda Lotfiomran for all the guidance from the start of my PhD and the International office team at DESY for helping an international settle here in Germany.

Now, moving on to my friends outside of our working group, I cannot express how much in debt I am to all of their support and friendship in both good and bad times during this journey, for all of the joyful moments, and simply being there during rough ones. Firstly to my girlfriend Maren Plöger for always making me smile. And now here's to all of my friends from DESY and MPSD/IMPRS: Alexandra Göbel, Mary-Leena Tchenkoue Djouom, Franco Bonafe, Maria Belen Banuelos, Philine van Vilet, Johannes Kaub, Krishna Saraswathula, Laura Silletti, Gaia Giovannetti, Sergey Ryabchuk, Marvin Reuner, Emily Thompson and Paolo Lazzaroni. And also friends from before my Ph.D. days for their continual support, whether it was from my time in Kathmandu, Bremen or Toronto: Aarju Shrestha, Maria Karcz, Sneha Singh, Eliuter Nderimo, Harsh Mahaseth and Christian Welp. Last, but not least, my rather large extended family for their encouragement to pursue my studies and my dreams. In particular, to my caring and supportive mom (whom I lovingly named "nan" when I was a kid and the name stuck now) and dad; thank you for all of your words to wisdom, love, support and sacrifices. This thesis is dedicated to the two of you.

List of publications

- Yashoj Shakya, Ludger Inhester, Caroline Arnold, Ralph Welsch, and Robin Santra, "Ultrafast time-resolved x-ray absorption spectroscopy of ionized urea and its dimer through ab initio nonadiabatic dynamics", *Structural Dynamics* **8**, 034102 (2021). <https://doi.org/10.1063/4.0000076>
- Zhong Yin*, Yi-Ping Chang*, Tadas Balčiūnas*, Yashoj Shakya*, Aleksa Djorović, Geoffrey Gaulier, Giuseppe Fazio, Robin Santra, Ludger Inhester, Jean-Pierre Wolf, and Hans Jakob Wörner, "Femtosecond proton transfer in urea solutions probed by X-ray spectroscopy", *Nature* (2023). <https://doi.org/10.1038/s41586-023-06182-6>
- Yashoj Shakya, Ralph Welsch, Ludger Inhester, and Robin Santra, "Capturing electronic decoherence in quantum-classical dynamics using the ring-polymer-surface-hopping-density-matrix approach", *Physical Review A* **107**, 062810 (2023). <https://doi.org/10.1103/PhysRevA.107.062810>

* Equal contribution

Contents

Abstract	vii
Zusammenfassung	ix
Acknowledgements	xi
List of publications	xiii
1 Introduction	1
1.1 About this thesis	5
2 Theoretical background	7
2.1 Nonadiabatic dynamics	7
2.1.1 Fewest switches surface hopping	10
2.1.2 Two-level system	12
2.2 Light matter interaction	13
2.2.1 Radiation field Hamiltonian	13
2.2.2 Electronic Hamiltonian	14
2.2.3 Interaction Hamiltonian	18
2.3 Quantum mechanics/molecular mechanics simulations	21
2.3.1 Molecular mechanics	21
2.3.2 Different QM/MM approaches	22
2.4 Path integral methods	23
2.4.1 Path Integral Molecular Dynamics	23
2.4.2 Ring polymer molecular dynamics	25
3 Ultrafast time-resolved x-ray absorption spectroscopy of ionized urea and its dimer in vacuum	27
3.1 Introduction	27
3.2 Computational method	29
3.3 Results	30
3.3.1 Urea	30
3.3.2 Urea dimer	35
3.4 Summary	43

4	Tracing ultrafast proton transfer dynamics in ionized aqueous urea	45
4.1	Introduction	45
4.2	Experimental setup and static spectra	47
4.3	Theoretical Computation Details	48
4.3.1	Initial MD setup	48
4.3.2	Ionized State Simulation	49
4.3.3	Theoretical TRXAS calculation	50
4.4	Results and Discussion	51
4.4.1	Urea aggregation	51
4.4.2	Molecular-orbital binding energies and deeper-valence hole state dynamics	52
4.4.3	Transient XAS	52
4.4.4	Analysing spectral features	55
4.4.5	Quantifying proton transfer	58
4.4.6	Revealing impact of proton transfer on XAS	60
4.4.7	Geometrical-parameter analysis for proton transfer	62
4.5	Summary	65
5	Capturing electronic decoherence in quantum-classical dynamics	67
5.1	Introduction	67
5.2	Theoretical background	69
5.2.1	Multistate path integral molecular dynamics	69
5.2.2	Previous ring polymer surface hopping variants	71
5.3	New ring polymer surface hopping-density matrix method	72
5.3.1	Hopping probability	73
5.3.2	Momentum rescaling	75
5.4	Application to Tully’s model potential	76
5.4.1	Simulation details and parameters	76
5.4.2	Results	77
5.5	Summary	85
6	Conclusion and outlook	87
A	Experimental details	91
A.1	Setup	91
A.2	Sample Preparation and Delivery	91
A.3	Energy Calibration	91
	Bibliography	93

List of Abbreviations

DOF	Degree of freedom
FSSH	Fewest switches surface hopping
HF	Hartree-Fock
HHG	High harmonic generation
HOMO	Highest occupied molecular orbital
MCTDH	Multi-configuration time-dependent Hartree
MD	Molecular dynamics
NAC	Nonadiabatic coupling
PES	Potential energy surfaces
PIMD	Path integral molecular dynamics
PLSR	Partial least square regression
PT	Proton transfer
QM/MM	Quantum mechanics/molecular mechanics
RPMD	Ring polymer molecular dynamics
RPSH	Ring polymer surface hopping
TRXAS	Time resolved x-ray absorption spectroscopy
XAS	X-ray absorption spectroscopy
XFEL	X-ray free-electron lasers

Chapter 1

Introduction

The world we live in is dynamic. People have been fascinated with understanding the dynamical processes around us, which has led to many innovations in this area. The first cameras using snapshot photography solved the famous galloping horse problem by capturing its motion at different times. Since then, technology has come a long way to the point where we can follow chemical reactions in real-time due to advances in laser technology to create femtosecond pulses [1-3]. The basic principle for this is to use pump-probe spectroscopy where a pump pulse initializes the dynamics by exciting or ionizing a system, which is then probed at certain time-delays with a probe pulse to gather information about the state of the system at that particular time. This has allowed following nuclear dynamics of molecules on excited state potential energy surfaces which occur in femtosecond timescale. For advancements in this field, termed femtochemistry, a Nobel prize was awarded to Ahmed Zewail in 1999 for his contributions to studying gas phase molecular dynamics [3].

Going to ever-shorter pulses in both time and wavelength is one of the central challenges in tracking the dynamics of atoms and molecules. Temporally short pulses are needed to instantaneously excite the system and also to resolve the ultrafast dynamics that follow. Nuclear vibrational motion and chemical reactions such as proton transfer and dissociation occur in femtosecond timescale, whereas electronic dynamics occur even faster in the attosecond regime. Initially, femtosecond pulses were in the infrared (IR), visible, and ultraviolet (UV) domain [4]. However, these are limited by their single optical cycle of about a few femtoseconds which has now been reached [5]. Going further to attoseconds in order to probe the dynamics of electrons requires x-ray pulses, which have shorter wavelengths of 10 pm to 10 nm to circumvent this limitation.

First discovered by Wilhelm Conrad Röntgen in 1895 [6], x-rays are now widely used to determine electronic properties and structure of varied systems from solid state to biological matter such as proteins and DNA [4]. Since x-rays have high enough energy to cause core level transitions, they can thus probe local environments and are element specific. Traditional x-ray pulses from synchrotrons lacked high temporal resolution though, reaching only up to a few tens of picoseconds [4], or up to a few tens or hundreds of femtoseconds using slicing techniques [7]. The advent of x-ray free-electron lasers (XFEL) such as European XFEL in Hamburg, Germany and LCLS

in California, USA has allowed shorter x-ray pulses of few femtoseconds [8–10], and recently even to few hundreds of attoseconds [11–13]. Advances in high harmonic generation (HHG) based x-ray sources have pushed this even further, reaching a few tens of attoseconds [14–16] with 43 as being the shortest pulse recorded to date [16]. HHG has the further advantage that it is a compact table-top setup that can be performed in laboratories, hence does not require large facilities such as those for synchrotron and XFEL experiments. However, the photon flux from it is rather low when compared to XFEL pulses [4].

Regarding how these ultrashort pulses can be used in experiments, multiple time-resolved techniques exist that can be used to probe different aspects of the dynamics or reveal information about molecular structure. Here, I only briefly introduce some of them that are done in a time-resolved manner in the x-ray domain, namely time-resolved x-ray absorption spectroscopy (TRXAS), time-resolved x-ray emission spectroscopy (TRXES), and time-resolved photoelectron spectroscopy (TRPES). For an elaborate review and application of these methods and others such as time-resolved resonant inelastic x-ray scattering (TRRIXS) [17] and high-harmonic spectroscopy (HHS) [18], see Refs. [19, 20]. Following initial excitation or ionization, TRXAS involves absorbing an x-ray photon to cause a transition from a core orbital to a vacant valence one or to the continuum above it. Based on the two different regions of absorption, TRXAS can be classified into x-ray absorption near-edge structure (XANES) spectroscopy for transitions from core to valence state and extended x-ray absorption fine structure (EXAFS) spectroscopy for core to continuum states [21]. XANES gives information about changes in the chemical environment that influence the core and valence levels over time [19]. As such, this has been used to probe from coherence electronic dynamics [22] in attosecond regime to femtosecond reaction dynamics such as electrocyclic ring-opening reaction [23] and photodissociation [24]. On the other hand, EXAFS gives information about molecular structure from intensity oscillations due to rescattering of the ejected photoelectron with the chemical environment. TRXES can provide complementary information to TRXAS by looking into the emitted photons after a core hole has been created and gives information on occupied states, in contrast to TRXAS which tells about unoccupied states [25]. In TRPES, the ejected photoelectron is measured after creating a core hole, which gives direct information on binding energies of core electrons that are sensitive to changes in local chemical structure [26].

All of the methods mentioned above provide important and complementary information to describe the ultrafast dynamics of atoms and molecules. This thesis, however, focuses on the use of TRXAS due to its capability in investigating both electronic and structural dynamics on femtosecond and attosecond timescales. This has been shown in recent experiments using HHG [23, 24, 27–29] or XFEL facilities [30–35] and also through theoretical simulations [36–44]. The experiments were mostly done in the gas phase, but recent extensions to the liquid phase have been done to study intermolecular interactions using TRXAS [28, 35, 45]. Given this progress, TRXAS

is an ideal technique for the purposes of this thesis, which aims to follow the ultrafast dynamics of a simple, yet biologically relevant molecule, namely urea, following valence ionization in both gas and aqueous solution. This thesis will further verify the capability of TRXAS to follow both nuclear and electronic dynamics.

Interpreting the results of these time-resolved experiments can, however, be quite challenging from an experimental point of view. Theoretical simulations help by shedding light on the ultrafast processes occurring in these experiments. Excitation or ionization from a pump pulse initiates the system in a non-equilibrium state from where the dynamics start and could involve multiple electronic states which are coupled to each other. In this case, the typically used Born-Oppenheimer adiabatic approximation breaks down which only takes into account a single potential energy surface (PES) and assumes electrons adjust instantaneously to nuclear motion. To go beyond, one needs to perform nonadiabatic dynamics involving multiple coupled PES. This sort of treatment is quite common in photoinduced reactions found in nature such as in the primary steps of vision [46] and photosynthesis [47, 48]. However, the computational costs for these simulations lay out a different challenge for theory, that is to go for large systems and long timescales to address experimental observations.

Full quantum dynamics methods such as multi-configuration time-dependent Hartree (MCTDH) [49, 50] provide exact solutions, making them a gold standard. However since they treat both nuclei and electrons quantum mechanically, they scale exponentially with the number of nuclear degrees of freedom (DOF). Additionally, they require the PES to be calculated and possibly fitted beforehand, which is a formidable task on its own for systems with lots of DOF. Hence, full quantum dynamics methods are computationally unfeasible to go to large systems and can only serve as benchmark results for smaller systems. MCTDH, for instance, can reach up to few tens of DOF [51], with multilayer MCTDH [52, 53] pushing it further in some cases. Going beyond would need additional approximations. Mixed quantum-classical (MQC) dynamics methods approximate the nuclear propagation with classical dynamics. One class of MQC methods does this by replacing the nuclear wave packet with a linear combination of classically propagating Gaussian basis functions [54, 55]. These methods can be derived from first principles and the evolution of the coefficients for each Gaussian function are coupled to each other. Based on the original method of Heller [54], many methods have been devised with this strategy such as multiple spawning [56–58], variational multiconfigurational Gaussian [59, 60] and multiconfigurational Ehrenfest [61]. These methods can handle more DOF than full quantum methods due to the use of classically driven Gaussians but are still limited due to coupling between them (see Ref. [62] for some applications of methods of this class).

Another class of MQC methods goes even further to make use of independent classical trajectories that are propagated based on forces from electronic coefficients attached to each trajectory, which makes these methods quite efficient for nonadiabatic dynamics [63]. Despite this drastic approximation, this class of methods which include Ehrenfest dynamics [64, 65] and trajectory surface hopping approaches [66–69] are

widely used due to their successes (see applications of these methods in Refs. [70, 71]). As opposed to full quantum dynamics where the PES needs to be precalculated, these methods work on-the-fly with PES only computed where the classical trajectory is at the moment. Ehrenfest dynamics is a mean-field method with trajectories evolving on a single effective potential obtained by a weighted average over the different PES. Although this method is quite efficient and simple to implement, it lacks correlation between classical nuclear and quantum electronic motion [63] and due to its mean-field nature, it does not properly describe long timescale dynamics where the PES are no longer coupled to each other [70].

In surface hopping approaches, on the other hand, trajectories are propagated on one state and can stochastically hop between different PES based on probabilities obtained from the evolution of the electronic coefficients. The different surface hopping methods differ in the way they compute this hopping probability. Tully's fewest switches surface hopping (FSSH) [66] algorithm is one of the most popular method of this class, which has been quite successful in describing a wide range of problems including proton transfer reaction [67, 72], photodissociation [73, 74], photoisomerization [75, 76] and energy transfer [77] (see Ref. [78] for a list of applications of FSSH). Hence, due to its computational efficiency and accuracy in describing nonadiabatic dynamics, FSSH is the method of choice for this thesis to simulate TRXAS over the dynamics. Although apart from not being rigorously derivable [79], FSSH also has drawbacks such as dependence on the choice of electronic basis, overcoherence problem, and lack of nuclear quantum effects [80]. These limitations have triggered numerous efforts to tackle these different issues, which are too many to list in this thesis (see Refs. [80, 81] for a list of problems in FSSH and possible methods to solve them). Adding to the literature on methods to solve the overcoherence problem [82–87], this thesis shows a unique way to solve this problem by combining FSSH with ring polymer molecular dynamics (RPMD) [88], which is an approximate method to add nuclear quantum effects into the dynamics and stems from Feynman's path integral approach [89]. Although such previous attempts have been made [90], they were focused more on nuclear quantum effects, whereas this thesis focuses on solving the overcoherence problem by combining them in a particular way.

Apart from the ones mentioned above, a plethora of other mixed quantum-classical nonadiabatic dynamics methods in the literature, each with its advantages and drawbacks. Without going into too much detail, some of them are quantum-classical Liouville equation [91, 92], mapping approach [93–95], nonadiabatic Bohmian dynamics [96] and exact-factorization based methods [97].

One final note, even though MQC dynamics methods are quite efficient compared to full quantum dynamics, they are still limited in system size by the evaluation of PES, hence, cannot go to systems with thousands of atoms. To do so, one can perform classical molecular dynamics (MD) using force fields that are able to simulate even large biological systems such as proteins and enzymes [98]. However, these are limited to the ground state and in general, cannot describe chemical reactions. A solution to

simulate large systems with the capability to go to excited states is using the quantum mechanics/molecular mechanics (QM/MM) [99] method where only a small part is treated quantum mechanically, for instance using MQC dynamics, which can undergo photoexcited chemical reactions and the rest using classical MD. This approach is also taken in this thesis to simulate TRXAS for molecules in an aqueous environment as this also involves a lot of atoms to create the solvated species.

1.1 About this thesis

This thesis involves, as the title suggests, both the application and method development of a quantum-classical dynamics method, namely FSSH. Following a general introduction in this chapter, I briefly outline the underlying theoretical background in Chapter 2 which includes the theory of nonadiabatic dynamics, light-matter interaction, QM/MM approach, and path integral techniques. In Chapter 3, I discuss my results on simulated TRXAS of ionized urea in vacuum using FSSH and how machine learning techniques can be used to perform statistical analysis to understand the dynamical features in the spectra. Chapter 4 builds up on the results of the vacuum calculations to extend the simulations to ionized urea in aqueous solution using the QM/MM scheme and compares the obtained TRXAS to experimental ones. In Chapter 5, I present a new method developed in this thesis that improves upon FSSH by combining it with RPMD. This method is implemented on our newly written code, named XPACDT, which is used to obtain results on a model system. Conclusions and outlook are drawn in Chapter 6.

Chapter 2

Theoretical background

In this chapter, I review the theoretical background that this thesis builds upon. The central theme of this thesis, which is coupled nuclear-electronic dynamics with multiple electronic states, also called nonadiabatic dynamics, is first introduced in Sec. 2.1, followed by a focus on a specific quantum-classical dynamics method, namely Tully's fewest switches surface hopping (FSSH). The theory behind how light-matter interaction is then discussed in Sec. 2.2 which results in a formulation for absorption spectroscopy. Then quantum mechanics/molecular mechanics (QM/MM) simulation is presented in Sec. 2.3 followed by path integral techniques in quantum statics and dynamics in Sec. 2.4.

Atomic units are used throughout this chapter, hence $\hbar = e = m_e = 1/(4\pi\epsilon_0) = 1$ where \hbar is the reduced Planck's constant, e is the elementary charge, m_e is the rest mass of an electron, and $K = 1/(4\pi\epsilon_0)$ is the Coulomb's constant. Speed of light $c = 1/\alpha$ in this unit system where α is the fine structure constant.

2.1 Nonadiabatic dynamics

For a molecular system with N nuclei and N_{el} electrons, the time-evolution of its wave function Ψ is governed by the time-dependent Schrödinger equation

$$i\frac{\partial\Psi(\mathbf{r}, \mathbf{R}, t)}{\partial t} = \hat{H}_{\text{mol}}(\mathbf{r}, \mathbf{R})\Psi(\mathbf{r}, \mathbf{R}, t), \quad (2.1)$$

where $\mathbf{r} = \{\mathbf{r}_a\}$ and $\mathbf{R} = \{\mathbf{R}_A\}$ are sets of all electronic and nuclear positions respectively, t is the time, and the molecular Hamiltonian \hat{H}_{mol} is given by

$$\begin{aligned} \hat{H}_{\text{mol}} &= -\sum_A \frac{\nabla_{\mathbf{R}_A}^2}{2M_A} + \frac{1}{2} \sum_{A \neq B} \frac{Z_A Z_B}{|\mathbf{R}_A - \mathbf{R}_B|} - \sum_a \frac{1}{2} \nabla_{\mathbf{r}_a}^2 + \frac{1}{2} \sum_{a \neq b} \frac{1}{|\mathbf{r}_a - \mathbf{r}_b|} - \sum_{a,A} \frac{Z_A}{|\mathbf{r}_a - \mathbf{R}_A|} \\ &= \hat{T}_{\text{N}} + \hat{V}_{\text{NN}} + \hat{T}_{\text{e}} + \hat{V}_{\text{ee}} + \hat{V}_{\text{eN}} \\ &= \hat{T}_{\text{N}} + \hat{H}_{\text{el}}, \end{aligned} \quad (2.2)$$

where $\nabla_{\mathbf{r}_a}$ is the gradient operator for the a^{th} electron, and M_A , Z_A and $\nabla_{\mathbf{R}_A}$ are the mass, charge and gradient for the A^{th} nuclei respectively. The different terms in Eq. (2.2) refer to the nuclear kinetic energy \hat{T}_{N} , nuclear-nuclear potential energy \hat{V}_{NN} , electronic kinetic energy \hat{T}_{e} , electronic-electronic potential energy \hat{V}_{ee} , and the

electronic-nuclear potential energy \hat{V}_{eN} operators. All the terms but \hat{T}_{N} can be combined into an electronic Hamiltonian $\hat{H}_{\text{el}}(\mathbf{r}, \mathbf{R})$ which has eigenenergies $E_j(\mathbf{R})$ and eigenstates $\phi_j(\mathbf{r}; \mathbf{R})$ such that they fulfill the time-independent electronic Schrödinger equation

$$\hat{H}_{\text{el}}(\mathbf{r}, \mathbf{R})\phi_j(\mathbf{r}; \mathbf{R}) = E_j(\mathbf{R})\phi_j(\mathbf{r}; \mathbf{R}). \quad (2.3)$$

Note that E_j and ϕ_j are also called adiabatic energy and adiabatic state respectively, and ϕ_j parametrically depend upon \mathbf{R} as nuclei are assumed to be fixed while solving Eq. (2.3). Obtaining E_j and ϕ_j is the main challenge in quantum chemistry and will partly be discussed in Sec. 2.2. Calculating E_j for a range of \mathbf{R} gives the adiabatic potential energy surfaces (PES) for the electronic states j .

The full molecular wave function Ψ can be expanded in terms of a complete set of these orthonormal adiabatic electronic states $\phi_j(\mathbf{r}; \mathbf{R})$ giving

$$\Psi(\mathbf{r}, \mathbf{R}, t) = \sum_j \chi_j(\mathbf{R}, t)\phi_j(\mathbf{r}; \mathbf{R}), \quad (2.4)$$

where $\chi_j(\mathbf{R}, t)$ is the time-dependent nuclear wave function for state j . This is known as Born-Huang expansion [100] and is exact in the case of a complete set of states. If only a single electronic state is considered, then this leads to the Born-Oppenheimer approximation [101]. Inserting Eq. (2.4) into Eq. (2.1), multiplying by $\phi_k^*(\mathbf{r}; \mathbf{R})$ from the left and integrating out the electronic part results in

$$i \frac{\partial \chi_k(\mathbf{R}, t)}{\partial t} = \left(\hat{T}_{\text{N}} + E_k(\mathbf{R}) \right) \chi_k(\mathbf{R}, t) - \sum_j \sum_A \left(\frac{1}{M_A} \mathbf{d}_{kj}(\mathbf{R}_A) \cdot \nabla_{\mathbf{R}_A} + \frac{1}{2M_A} \cdot D_{kj}(\mathbf{R}_A) \right) \chi_j(\mathbf{R}, t) \quad (2.5)$$

where the first- and second-order nonadiabatic couplings (NAC) are $\mathbf{d}_{kj}(\mathbf{R}_A) = \langle \phi_k | \nabla_{\mathbf{R}_A} | \phi_j \rangle$ and $D_{kj}(\mathbf{R}_A) = \langle \phi_k | \nabla_{\mathbf{R}_A}^2 | \phi_j \rangle$ respectively. Note that \mathbf{d}_{kj} is anti-Hermitian giving $\mathbf{d}_{kk} = 0$ and $\mathbf{d}_{kj} = -\mathbf{d}_{jk}^*$, and since D_{kj} involves second order derivatives, its magnitude is small, thus often neglected. For adiabatic states, \mathbf{d}_{kj} can also be calculated using the Hellmann-Feynman theorem [102, 103]

$$\mathbf{d}_{kj}(\mathbf{R}) = \frac{\langle \phi_k | \nabla_{\mathbf{R}} \hat{H}_{\text{el}} | \phi_j \rangle}{E_j - E_k}. \quad (2.6)$$

Equation (2.5) is a coupled differential equation between the different electronic states and solving this to propagate χ_k is the main aim of quantum dynamics. The off-diagonal NAC terms are responsible for the coupling between different electronic states and lead to the population being transferred between the states. As there are multiple states involved in the dynamics, this is known as nonadiabatic dynamics. If the NAC terms are ignored, then this results in Born-Oppenheimer adiabatic dynamics where the nuclear wave functions in the different states evolve independently of each other. However, it is important to note that this is an approximation and is only valid

if the NACs are negligible, for instance when the adiabatic energies are well separated as seen from Eq. (2.6).

Apart from the fact that the adiabatic basis changes with nuclear coordinates \mathbf{R} , using this basis has additional problems. Namely, the fact that if two states are equal in energy, this leads to infinite \mathbf{d}_{kj} as seen from Eq. (2.6), which causes numerical problems while solving Eq. (2.5). This issue can be overcome by using a different basis expansion for Eq. (2.4) instead of the adiabatic basis. A more stable basis would be to use a diabatic basis where the electronic states $\tilde{\phi}_j(\mathbf{r}; \mathbf{R}_o)$ are chosen with respect to a fixed reference nuclear geometry \mathbf{R}_o , giving the following exact expansion

$$\Psi(\mathbf{r}, \mathbf{R}, t) = \sum_j \tilde{\chi}_j(\mathbf{R}, t) \tilde{\phi}_j(\mathbf{r}; \mathbf{R}_o), \quad (2.7)$$

where $\tilde{\chi}_j(\mathbf{R}, t)$ is the nuclear wave function associated with the j^{th} diabatic basis. This results in $\tilde{\phi}_j$ not depending upon \mathbf{R} , so the first and second order NACs are 0. In this basis, \hat{H}_{el} is not a diagonal matrix in the electronic basis anymore since $\tilde{\phi}_j$ is not, in general, an eigenstate of \hat{H}_{el} . The off-diagonal potential terms here are responsible for coupling the different states instead of the NACs. Important to note that this basis is not unique as \mathbf{R}_o can be chosen arbitrarily.

Now to briefly discuss some of the practical ways to solve the nonadiabatic dynamics problem. For a small number of nuclear degrees of freedom (DOF), one can directly solve Eq. (2.5) by expanding χ_k in some time-independent basis. However, this scales exponentially with DOF and is only feasible for systems containing few atoms. The multi-configuration time-dependent Hartree (MCTDH) method [49, 50] circumvents part of this problem by using some intermediate time-dependent basis functions which in general would be smaller in number than the basis sets used in the standard approach. This makes MCTDH more efficient and is considered a gold standard for solving full quantum dynamics problems exactly, reaching up to a few tens of DOF (see Ref. [51] for a review and some applications of MCTDH). However, to go beyond this, additional approximations have to be made such as approximating the nuclear wave packet with a set of trajectories following classical dynamics. This results in mixed quantum-classical (MQC) dynamics methods where the nuclei are treated classically and electrons quantum mechanically. One such popular approach is the multiple spawning method [56–58] where classical Gaussian basis functions are propagated along with their amplitude coefficients on each state evolving quantum mechanically with coupled sets of differential equations. This classical approximation here also means that the potential energy surfaces can be calculated on-the-fly during the dynamics and do not have to be precomputed as for full quantum dynamics. This has made multiple spawning applicable to larger systems with more DOF (see Ref. [62] for a review and some applications of this method).

Going even further, one can invoke a severe approximation of independent classical trajectories which makes this class of MQC methods computationally highly efficient. The most popular methods of this class are Tully’s fewest switches surface hopping

(FSSH) [66] and Ehrenfest dynamics [64]. These methods propagate expansion coefficients in the different PES independently along with classical trajectory which determines the forces for the trajectory. In Ehrenfest dynamics, a weighted average force of the multiple states is used to propagate the trajectory. However, this might not be a good choice for long timescale dynamics when the trajectory is well beyond the regions of non-negligible NAC [70]. On the other hand, the trajectories in FSSH move only on a single PES with a possibility to hop between the states. Details of FSSH will be discussed in more detail in the next section as it is the method of choice for this thesis, owing to its numerous successes (see Ref. [78] for a list of applications of FSSH).

2.1.1 Fewest switches surface hopping

A brief overview of the FSSH method for quantum-classical dynamics is given in this section following mostly Tully's original work [66]. First, probability distributions in the nuclear and electronic state spaces are sampled by mutually independent trajectories with nuclear positions $\mathbf{R}(t)$ and momenta $\mathbf{P}(t)$. Then for each trajectory, the nuclei are propagated classically based on Newton's equations of motion on a single PES. The propagation can be done numerically using methods such as the velocity Verlet algorithm [104]. An electronic wave function $\psi(\mathbf{r}, \mathbf{R}, t)$ is associated with each trajectory that can be expanded in terms of any set of electronic basis states $\phi_j(\mathbf{r}; \mathbf{R})$

$$\psi(\mathbf{r}, \mathbf{R}, t) = \sum_j c_j(t) \phi_j(\mathbf{r}; \mathbf{R}), \quad (2.8)$$

where the $c_j(t)$ are time-dependent expansion coefficients. By plugging this expansion into the time-dependent electronic Schrödinger equation, the following equation is obtained for the evolution of these coefficients

$$\dot{c}_k = -i \sum_j c_j V_{kj}(\mathbf{R}) - \sum_j \dot{\mathbf{R}} \cdot \mathbf{d}_{kj}(\mathbf{R}) c_j, \quad (2.9)$$

where $V_{kj}(\mathbf{R})$ is the matrix element of the electronic Hamiltonian \hat{H}_{el} . In the adiabatic basis, where the potential energy matrix is diagonal, $V_{kj} = E_k \delta_{kj}$, Eq. (2.9) simplifies to

$$\dot{c}_k = -i c_k E_k(\mathbf{R}) - \sum_j \dot{\mathbf{R}} \cdot \mathbf{d}_{kj}(\mathbf{R}) c_j. \quad (2.10)$$

The actual PES on which the nuclear trajectory is propagated can change during the propagation. Based on the evolution of the electronic state coefficients, the individual trajectories can hop between the different PESs. From Eq. (2.9) electronic state populations $a_{kk} = c_k c_k^*$ for a given electronic state k evolve through

$$\dot{a}_{kk} = \sum_{l \neq k} b_{kl}, \quad (2.11)$$

where

$$b_{kl} = 2 \operatorname{Im} (c_l c_k^* V_{kl}(\mathbf{R})) - 2 \operatorname{Re} \left(c_l c_k^* \dot{\mathbf{R}} \cdot \mathbf{d}_{kl}(\mathbf{R}) \right). \quad (2.12)$$

As per the name of the method, we aim for the fewest switches between the surfaces. To achieve this, Tully prescribes the following hopping probability from state k to j for each time step $t \rightarrow t + \Delta$ [67]

$$P_{kj} = \frac{\int_t^{t+\Delta} b_{jk}(t') dt'}{a_{kk}(t)}. \quad (2.13)$$

Note that this expression from Ref. [67] is slightly different than Tully's original work [66] which involves an approximation of the above expression. The probability to hop to the same state is 0 and any negative probabilities obtained are set to 0. Now to decide whether or not to hop, first a uniformly sampled random number ζ is generated from 0 to 1. Since there can be multiple states involved, a hop from state k to j takes place if ζ satisfies this condition

$$\sum_{l=1}^{j-1} P_{kl} < \zeta \leq \sum_{l=1}^j P_{kl}. \quad (2.14)$$

After the hop, the nuclei are propagated on state j . If none of these conditions are fulfilled for the different states, the trajectory continues in the same state k .

When such a hop occurs, the nuclear momenta are rescaled in the direction of the NAC to conserve the total energy with a rescaling parameter γ_{kj}

$$\mathbf{P}_f = \mathbf{P}_{\text{in}} - \gamma_{kj} \mathbf{d}_{kj}(\mathbf{R}), \quad (2.15)$$

where \mathbf{P}_{in} and \mathbf{P}_f are the momenta before and after the hop, respectively. Requiring conservation of energy, the following equation is obtained for γ_{kj}

$$\gamma_{kj} = \frac{B_{kj} \pm \sqrt{B_{kj}^2 + 4A_{kj} \cdot C_{kj}}}{2A_{kj}}, \quad (2.16)$$

where

$$\begin{aligned} A_{kj} &= \sum_A \frac{1}{2M_A} (\mathbf{d}_{kj}(\mathbf{R}_A))^2, \\ B_{kj} &= \sum_A \frac{1}{M_A} \mathbf{P}_{A,\text{in}} \cdot \mathbf{d}_{kj}(\mathbf{R}_A), \\ C_{kj} &= V_{kk}(\mathbf{R}) - V_{jj}(\mathbf{R}), \end{aligned}$$

where the sign in Eq. (2.16) is chosen to obtain the smallest change in momenta. In case

$$B_{kj}^2 + 4A_{kj} \cdot C_{kj} < 0, \quad (2.17)$$

the hop is forbidden since this implies that the system does not have sufficient kinetic energy for the transition, so it continues to propagate on state k .

This propagation and hopping can be repeated for each time step until a desired finishing condition is reached. Due to the stochastic nature of the hops, many trajectories need to be propagated till the observable of interest such as state population or nuclear distribution converges.

2.1.2 Two-level system

Two-level systems are ubiquitous in quantum mechanics such as in spin 1/2 systems or ground-excited state systems. In the current context of nonadiabatic dynamics, this can be achieved by limiting the Born-Huang expansion in Eq. (2.4) to just two electronic states. Two-level model potentials such as Tully's model systems [66] offer a simple test system for nonadiabatic dynamics methods. Since this thesis involves developing such a method and testing it on a two-level system, let us briefly go over it. A general two-level potential energy which is a matrix in electronic basis (denoted by underlining) and depends upon \mathbf{R} can be written as

$$\underline{V}(\mathbf{R}) = \begin{pmatrix} V_{11}(\mathbf{R}) & V_{12}(\mathbf{R}) \\ V_{21}(\mathbf{R}) & V_{22}(\mathbf{R}) \end{pmatrix}. \quad (2.18)$$

This potential is Hermitian such that $V_{21} = V_{12}^*$ and could be in any general electronic basis. Since the adiabatic basis is more commonly used in FSSH, adiabatic energies and states can be obtained by diagonalizing \underline{V} to get eigenvalues and eigenvectors, respectively. The adiabatic energies are thus

$$E_{1,2}(\mathbf{R}) = \frac{V_{11} + V_{22}}{2} \mp \frac{\sqrt{(V_{11} - V_{22})^2 + 4|V_{12}|^2}}{2}, \quad (2.19)$$

where E_1 and E_2 are given by the negative ($-$) and positive ($+$) solutions, respectively. The unitary transformation matrix used to diagonalize \underline{V} can be written in terms of a rotation matrix for a real-valued potential given by

$$U(\mathbf{R}) = \begin{pmatrix} \cos \theta & -\sin \theta \\ \sin \theta & \cos \theta \end{pmatrix}, \quad (2.20)$$

where the rotation angle is

$$\theta(\mathbf{R}) = \frac{1}{2} \arctan\left(\frac{2V_{12}}{V_{11} - V_{22}}\right). \quad (2.21)$$

The two columns in Eq. (2.20) give the adiabatic states $|\phi_1\rangle$ and $|\phi_2\rangle$. Note that there is an additional phase difference factor between the two states that can be arbitrarily

chosen. Here, the first-order NAC between the two states is given as

$$\begin{aligned} \mathbf{d}_{12}(\mathbf{R}) &= -\nabla_{\mathbf{R}}\theta \\ &= \frac{\nabla_{\mathbf{R}}V_{12} \cdot (V_{22} - V_{11}) - V_{12} \cdot (\nabla_{\mathbf{R}}V_{22} - \nabla_{\mathbf{R}}V_{11})}{(V_{22} - V_{11})^2 + 4|V_{12}|^2}. \end{aligned} \quad (2.22)$$

2.2 Light matter interaction

A proper theoretical framework that consistently describes light and matter will help us to understand how they interact with each other, allowing us to describe phenomena such as absorption, emission, and scattering. In this section, I will present such a framework based on Ref. [105] and will focus on how that leads to an expression for cross sections in absorption spectroscopy. The total Hamiltonian for an interacting light and matter system can be written as

$$\hat{H} = \hat{H}_{\text{rad}} + \hat{H}_{\text{el}} + \hat{H}_{\text{int}}, \quad (2.23)$$

where \hat{H}_{rad} is the light or radiation field Hamiltonian, \hat{H}_{el} is the electronic Hamiltonian from Eq. (2.2), and \hat{H}_{int} is the interaction Hamiltonian between them. In the following sections, the different parts of the total Hamiltonian from Eq. (2.23) will be discussed separately in the second quantization formalism (see Ref. [106] for more details on this formalism). Note that in this section, nuclear motion is neglected and the focus is only on the response of electrons to the external radiation field.

2.2.1 Radiation field Hamiltonian

An electromagnetic field, described by Maxwell's equations, with electric \mathbf{E} and magnetic \mathbf{B} fields can be expressed in terms of vector \mathbf{A} and scalar Φ potentials

$$\begin{aligned} \mathbf{E} &= -\nabla\Phi - \alpha \frac{\partial \mathbf{A}}{\partial t} \\ \mathbf{B} &= \nabla \times \mathbf{A}. \end{aligned} \quad (2.24)$$

Note that $\nabla \cdot \mathbf{B} = 0$, i.e. \mathbf{B} has only transverse components. In Eq. (2.24), there is still gauge freedom such that a gauge transformation of \mathbf{A} and Φ leaves \mathbf{E} and \mathbf{B} invariant. Choosing the Coulomb gauge, i.e. $\nabla \cdot \mathbf{A} = 0$, for a free electromagnetic field, \mathbf{E} also becomes purely transverse. Now quantizing the fields, the second quantized Hamiltonian for a free radiation field is given as

$$\begin{aligned} \hat{H}_{\text{rad}} &= \frac{1}{8\pi} \int d^3x \left(\hat{\mathbf{E}}^2 + \hat{\mathbf{B}}^2 \right) \\ &= \frac{1}{8\pi} \int d^3x \left\{ \alpha^2 \left(\frac{\partial \hat{\mathbf{A}}}{\partial t} \right)^2 + \left(\nabla \times \hat{\mathbf{A}} \right)^2 \right\}. \end{aligned} \quad (2.25)$$

$\hat{\mathbf{A}}$ can be expanded in terms of plane waves in a box with volume V

$$\hat{\mathbf{A}}(\mathbf{x}) = \sum_{\mathbf{k}, \lambda} \sqrt{\frac{2\pi}{V\omega_{\mathbf{k}}\alpha^2}} \left(\hat{a}_{\mathbf{k}, \lambda} \epsilon_{\mathbf{k}, \lambda} e^{i\mathbf{k} \cdot \mathbf{x}} + \hat{a}_{\mathbf{k}, \lambda}^\dagger \epsilon_{\mathbf{k}, \lambda}^* e^{-i\mathbf{k} \cdot \mathbf{x}} \right), \quad (2.26)$$

where $\hat{a}_{\mathbf{k}, \lambda}$ and $\hat{a}_{\mathbf{k}, \lambda}^\dagger$ are annihilation and creation operators, respectively, for a photon in mode described by wave vector \mathbf{k} and polarization $\epsilon_{\mathbf{k}, \lambda}$ ($\lambda = 1$ or 2) with mode frequency $\omega_{\mathbf{k}} = |\mathbf{k}|/\alpha$. \mathbf{k} and the two polarization vectors $\epsilon_{\mathbf{k}, \lambda}$ are all orthogonal to each other. Since photons are bosons, $\hat{a}_{\mathbf{k}, \lambda}$ and $\hat{a}_{\mathbf{k}, \lambda}^\dagger$ follow the bosonic commutation relations

$$\begin{aligned} [\hat{a}_{\mathbf{k}, \lambda}, \hat{a}_{\mathbf{k}', \lambda'}] &= [\hat{a}_{\mathbf{k}, \lambda}^\dagger, \hat{a}_{\mathbf{k}', \lambda'}^\dagger] = 0, \\ [\hat{a}_{\mathbf{k}, \lambda}, \hat{a}_{\mathbf{k}', \lambda'}^\dagger] &= \delta_{\mathbf{k}, \mathbf{k}'} \delta_{\lambda, \lambda'}. \end{aligned} \quad (2.27)$$

Using the mode expansion from Eq. (2.26), the radiation Hamiltonian can be written as a sum of independent harmonic oscillator Hamiltonians for each mode

$$\hat{H}_{\text{rad}} = \sum_{\mathbf{k}, \lambda} \omega_{\mathbf{k}} \left(\hat{a}_{\mathbf{k}, \lambda}^\dagger \hat{a}_{\mathbf{k}, \lambda} + \frac{1}{2} \right). \quad (2.28)$$

The number operator $\hat{n}_{\mathbf{k}, \lambda} = \hat{a}_{\mathbf{k}, \lambda}^\dagger \hat{a}_{\mathbf{k}, \lambda}$ counts the number of photons $n_{\mathbf{k}, \lambda}$ in the mode (\mathbf{k}, λ)

$$\hat{n}_{\mathbf{k}, \lambda} |n_{\mathbf{k}, \lambda}\rangle = n_{\mathbf{k}, \lambda} |n_{\mathbf{k}, \lambda}\rangle, \quad (2.29)$$

where a complete set of orthonormal states are formed by $|n_{\mathbf{k}, \lambda}\rangle$.

2.2.2 Electronic Hamiltonian

To be consistent with the formulation of the electromagnetic field, we now go to the second quantized formulation also for the electronic Hamiltonian \hat{H}_{el} given in first quantization in Eq. (2.2). Again, note that we are only interested in the interaction of electrons with the radiation field, hence, nuclear dynamics is neglected here. For second quantization, we first define an electron field operator

$$\hat{\psi}(\mathbf{x}) = \begin{pmatrix} \hat{\psi}_{1/2}(\mathbf{x}) \\ \hat{\psi}_{-1/2}(\mathbf{x}) \end{pmatrix}, \quad (2.30)$$

which is a two-component spinor where the operators $\hat{\psi}_\sigma(\mathbf{x})$ and $\hat{\psi}_\sigma^\dagger(\mathbf{x})$ annihilate and create an electron, respectively, at position \mathbf{x} with spin quantum number σ . Since electrons are fermions, these field operators fulfill the fermionic anti-commutator relations

$$\begin{aligned} \left\{ \hat{\psi}_\sigma(\mathbf{x}), \hat{\psi}_\sigma(\mathbf{x}') \right\} &= \left\{ \hat{\psi}_\sigma^\dagger(\mathbf{x}), \hat{\psi}_{\sigma'}^\dagger(\mathbf{x}') \right\} = 0, \\ \left\{ \hat{\psi}_\sigma(\mathbf{x}), \hat{\psi}_{\sigma'}^\dagger(\mathbf{x}') \right\} &= \delta_{\sigma, \sigma'} \delta(\mathbf{x} - \mathbf{x}'). \end{aligned} \quad (2.31)$$

The second quantized electronic Hamiltonian in the Schrödinger picture can then be written in terms of $\hat{\psi}(\mathbf{x})$ as

$$\begin{aligned} \hat{H}_{\text{el}} = & \int d^3x \hat{\psi}^\dagger(\mathbf{x}) \left[-\frac{1}{2} \nabla^2 - \sum_A \frac{Z_A}{|\mathbf{x} - \mathbf{R}_A|} \right] \hat{\psi}(\mathbf{x}) \\ & + \frac{1}{2} \int d^3x \int d^3x' \hat{\psi}^\dagger(\mathbf{x}) \hat{\psi}^\dagger(\mathbf{x}') \frac{1}{|\mathbf{x} - \mathbf{x}'|} \hat{\psi}(\mathbf{x}') \hat{\psi}(\mathbf{x}) + V_{\text{NN}}. \end{aligned} \quad (2.32)$$

Here, in the case of static nuclei, V_{NN} is a constant energy shift.

Similar to the mode expansion of the radiation field, the electron field can also be expanded in terms of a complete set of orthonormal spin orbitals $\varphi_p(\mathbf{x})$, which are the eigenstates of an effective one-electron Hamiltonian \hat{H}

$$\begin{aligned} \hat{H} \varphi_p(\mathbf{x}) &= \left(-\frac{1}{2} \nabla^2 - \sum_A \frac{Z_A}{|\mathbf{x} - \mathbf{R}_A|} + \bar{V}(\mathbf{x}) \right) \varphi_p(\mathbf{x}) \\ &= \epsilon_p \varphi_p(\mathbf{x}), \end{aligned} \quad (2.33)$$

where ϵ_p is the eigenvalue, also called orbital energy, of $\varphi_p(\mathbf{x})$ and $\bar{V}(\mathbf{x})$ is a mean-field potential that takes into account the electron-electron interaction in an approximate way. More details on the choice of $\bar{V}(\mathbf{x})$ and obtaining $\varphi_p(\mathbf{x})$ will be discussed later when discussing the Hartree-Fock approximation. The field operators $\hat{\psi}(\mathbf{x})$ and $\hat{\psi}^\dagger(\mathbf{x})$ in this expansion are given as

$$\begin{aligned} \hat{\psi}(\mathbf{x}) &= \sum_p \hat{c}_p \varphi_p(\mathbf{x}), \\ \hat{\psi}^\dagger(\mathbf{x}) &= \sum_p \hat{c}_p^\dagger \varphi_p^\dagger(\mathbf{x}), \end{aligned} \quad (2.34)$$

where the expansion coefficients \hat{c}_p and \hat{c}_p^\dagger are the annihilation and creation operators, respectively, for an electron in spin orbital $\varphi_p(\mathbf{x})$, and obey anti-commutator relations

$$\begin{aligned} \{\hat{c}_p, \hat{c}_q\} &= \{\hat{c}_p^\dagger, \hat{c}_q^\dagger\} = 0, \\ \{\hat{c}_p, \hat{c}_q^\dagger\} &= \delta_{p,q}. \end{aligned} \quad (2.35)$$

The Fock states $|\{n_p\}\rangle = |n_1, n_2, \dots\rangle$ form a complete orthonormal basis in the electron states and the number operator $\hat{n}_p = \hat{c}_p^\dagger \hat{c}_p$ counts the number of electrons in state p

$$\hat{n}_p |\{n_q\}\rangle = n_p |\{n_q\}\rangle. \quad (2.36)$$

Due to the fermionic character of the electrons, n_p can only be 0 or 1. A small note on notation, states or spin orbitals that are occupied by an electron are labelled by i, j, k and so on, and unoccupied ones by a, b and so on. p, q and so on refer to general spin orbitals, both occupied and unoccupied.

Before proceeding any further, it is useful to define one-body and two-body operators in this formalism. One-body operators act only on a single particle; an example of this is \hat{H} . These are represented by

$$\begin{aligned}\hat{t} &= \int d^3x \hat{\psi}^\dagger(\mathbf{x})t(\mathbf{x})\hat{\psi}(\mathbf{x}) \\ &= \sum_{p,q} t_{pq}\hat{c}_p^\dagger\hat{c}_q,\end{aligned}\quad (2.37)$$

where the one-body operator matrix elements are defined as

$$t_{pq} = \langle \varphi_p | t(\mathbf{x}) | \varphi_q \rangle = \int d^3x \varphi_p^*(\mathbf{x})t(\mathbf{x})\varphi_q(\mathbf{x}). \quad (2.38)$$

Two-body operators, on the other hand, describe the interaction between two particles, such as electron-electron repulsion potential, and are represented by

$$\begin{aligned}\hat{v} &= \frac{1}{2} \int d^3x \int d^3x' \hat{\psi}^\dagger(\mathbf{x})\hat{\psi}^\dagger(\mathbf{x}')v(\mathbf{x},\mathbf{x}')\hat{\psi}(\mathbf{x}')\hat{\psi}(\mathbf{x}) \\ &= \frac{1}{2} \sum_{p,q,r,s} v_{p,q,r,s}\hat{c}_p^\dagger\hat{c}_q^\dagger\hat{c}_s\hat{c}_r,\end{aligned}\quad (2.39)$$

where

$$v_{p,q,r,s} = \int d^3x \int d^3x' \varphi_p^\dagger(\mathbf{x})\varphi_q^\dagger(\mathbf{x}')v(\mathbf{x},\mathbf{x}')\varphi_r(\mathbf{x})\varphi_s(\mathbf{x}'). \quad (2.40)$$

Now, the electronic Hamiltonian \hat{H}_{el} can be repartitioned as

$$\hat{H}_{\text{el}} = \hat{H} + \hat{V}_{\text{res}} + V_{\text{NN}}, \quad (2.41)$$

where the mean-field Hamiltonian \hat{H} can be written as

$$\begin{aligned}\hat{H} &= \sum_{p,q} \langle \varphi_p | \left[-\frac{1}{2}\nabla^2 - \sum_A \frac{Z_A}{|\mathbf{x} - \mathbf{R}_A|} + \bar{V} \right] | \varphi_q \rangle \hat{c}_p^\dagger\hat{c}_q \\ &= \sum_p \epsilon_p \hat{c}_p^\dagger\hat{c}_p,\end{aligned}\quad (2.42)$$

and the residual electron-electron interaction potential \hat{V}_{res} , which is simply the mean-field potential \bar{V} subtracted from the electron-electron interaction term, is given as

$$\hat{V}_{\text{res}} = \frac{1}{2} \sum_{p,q,r,s} v_{p,q,r,s}\hat{c}_p^\dagger\hat{c}_q^\dagger\hat{c}_s\hat{c}_r - \sum_{p,q} \langle \varphi_p | \bar{V} | \varphi_q \rangle \hat{c}_p^\dagger\hat{c}_q. \quad (2.43)$$

Here, and from now on, $v_{p,q,r,s}$ is defined as the Coulomb matrix element of orbitals p, q, r, s :

$$v_{p,q,r,s} = \int d^3x \int d^3x' \varphi_p^\dagger(\mathbf{x})\varphi_q^\dagger(\mathbf{x}')\frac{1}{|\mathbf{x} - \mathbf{x}'|}\varphi_r(\mathbf{x})\varphi_s(\mathbf{x}'). \quad (2.44)$$

This repartitioning now shifts the problem to finding $\varphi_p(\mathbf{x})$ which serves as a basis for eigenstates of \hat{H}_{el} and to find the optimal form of \bar{V} that reduces the effect of \hat{V}_{res} .

One of the simplest strategies is using the Hartree-Fock method which will be briefly discussed below.

Hartree-Fock

In this section, I briefly introduce the closed shell restricted Hartree-Fock mean-field method for describing the non-degenerate ground state of a N_{el} -electron system through a certain solution for ϵ_p and $\varphi_p(\mathbf{x})$ that leads to an expression for \bar{V} ; see Ref. [106] for more detailed discussion and derivation. This ground state is approximated by a single antisymmetric Fock state $|\Phi_0^{N_{\text{el}}}\rangle = |\{n_p\}\rangle$ which aims at minimizing the energy $\langle \Phi_0^{N_{\text{el}}} | \hat{H}_{\text{el}} | \Phi_0^{N_{\text{el}}} \rangle$, thus providing the best possible approximation to the exact ground state energy. Through variational principle, one obtains the following Hartree-Fock equations for occupied spin orbitals $\varphi_i(\mathbf{x})$

$$\begin{aligned} \epsilon_i \varphi_i(\mathbf{x}) &= f \varphi_i(\mathbf{x}) \\ &= \left(-\frac{1}{2} \nabla^2 - \sum_A \frac{Z_A}{|\mathbf{x} - \mathbf{R}_A|} \right) \varphi_i(\mathbf{x}) + \sum_j \int d^3x' \frac{\varphi_j^*(\mathbf{x}') \varphi_j(\mathbf{x}')}{|\mathbf{x} - \mathbf{x}'|} \varphi_i(\mathbf{x}) \\ &\quad - \sum_j \int d^3x' \frac{\varphi_j^*(\mathbf{x}') \varphi_i(\mathbf{x}')}{|\mathbf{x} - \mathbf{x}'|} \varphi_j(\mathbf{x}), \end{aligned} \quad (2.45)$$

where f is called the Fock operator. The third term on the right-hand side of Eq. (2.45) is called the direct interaction which describes the Coulomb interaction between electron i and the density cloud from the rest of the electrons, and the last term is the non-local exchange interaction. Note that ϵ_i is spin-independent in restricted Hartree-Fock. Since building the Fock operator already requires all the occupied spin orbitals, Eq. (2.45) needs to be solved self-consistently, starting with an initial guess of the spin orbitals and then solving them till the orbital energies converge. After obtaining results for occupied spin orbitals, a similar equation can then be solved for unoccupied spin orbitals $\varphi_a(\mathbf{x})$.

In the Hartree-Fock approximation, one obtains the following mean-field potential

$$\bar{V}_{pq} = \sum_i (v_{pqi} - v_{piiq}), \quad (2.46)$$

which results in the Hartree-Fock energy for state $|\Phi_0^{N_{\text{el}}}\rangle$ is given by

$$\langle \Phi_0^{N_{\text{el}}} | \hat{H}_{\text{el}} | \Phi_0^{N_{\text{el}}} \rangle = \sum_i \epsilon_i - \frac{1}{2} \sum_{i,j} (v_{ijij} - v_{ijji}) + V_{\text{NN}}. \quad (2.47)$$

The Hartree-Fock method provides a basis from which excited states can be constructed using higher-order methods such as configuration interaction (CI) or coupled cluster (CC). These methods build upon Hartree-Fock and go beyond it by including electronic correlation effects missing in Hartree-Fock due to the use of mean-field potential. This is included by adding terms with holes (lack of electrons) in occupied

orbitals and particles (electrons) in unoccupied ones from the ground state $|\Phi_0^{N_{\text{el}}}\rangle$. Configuration interaction singles (CIS) for instance includes terms with $1p-1h$ (one-particle and one-hole).

Koopmans' theorem

Now, to describe an ionized system starting from a Hartree-Fock ground state, the following $1h$ (one-hole) configuration with a hole in state i is considered

$$|\Phi_i^{N_{\text{el}}-1}\rangle = \hat{c}_i |\Phi_0^{N_{\text{el}}}\rangle. \quad (2.48)$$

Here, one gets

$$\langle \Phi_i^{N_{\text{el}}-1} | \hat{H}_{\text{el}} | \Phi_i^{N_{\text{el}}-1} \rangle - \langle \Phi_0^{N_{\text{el}}} | \hat{H}_{\text{el}} | \Phi_0^{N_{\text{el}}} \rangle = -\epsilon_i, \quad (2.49)$$

which is known as Koopmans' theorem. Here, in the Hartree-Fock approximation, the electron binding energy or ionization potential, which is the difference between the energy of $(N_{\text{el}}-1)$ -electron system to the N_{el} -electron system, is given by the negative of the orbital energy ϵ_i .

2.2.3 Interaction Hamiltonian

Now, let us look into the term that couples light and matter, namely the interaction Hamiltonian \hat{H}_{int} , which from the principle of minimal coupling is given by

$$\hat{H}_{\text{int}} = \alpha \sum_a \hat{\mathbf{p}}_a \cdot \hat{\mathbf{A}}(\mathbf{r}_a) + \frac{1}{2} \alpha^2 \sum_a \hat{\mathbf{A}}^2(\mathbf{r}_a), \quad (2.50)$$

where $\hat{\mathbf{p}}_a$ is the momentum operator for the a^{th} electron. In the second quantized formulation, this can be written as

$$\hat{H}_{\text{int}} = \alpha \sum_{p,q} \langle \varphi_p | \mathbf{p} \cdot \hat{\mathbf{A}}(\mathbf{x}) | \varphi_q \rangle \hat{c}_p^\dagger \hat{c}_q + \frac{1}{2} \alpha^2 \sum_{p,q} \langle \varphi_p | \hat{\mathbf{A}}^2(\mathbf{x}) | \varphi_q \rangle \hat{c}_p^\dagger \hat{c}_q. \quad (2.51)$$

The first term is referred to as the ' $\mathbf{p} \cdot \mathbf{A}$ ' term and the second as the ' A^2 ' term. In this formalism, it is easy to see that both the operators change the state of one electron from q to p . By plugging in the mode expansion of $\hat{\mathbf{A}}$ from Eq. (2.26), we see that the ' $\mathbf{p} \cdot \mathbf{A}$ ' term leads to one-photon absorption (annihilation) or emission (creation), and the ' A^2 ' term causes two-photon absorption or emission, or scattering of one photon.

Depending upon whether \hat{H}_{int} vanishes at some later time or not, there are two distinct cases to be considered. If \hat{H}_{int} is permanently present, then this causes energy shifts of the total coupled systems such as in Lamb shift or AC Stark shift. If it vanishes at later times, then this causes transitions between eigenstates of the light and matter fields, which is the case for photon absorption, emission, and scattering. The latter is the focus of this thesis, in particular one-photon absorption, so this

type of interaction will be discussed. To that end, first, we need to talk about time-dependent perturbation theory which describes an interaction with a time-dependent potential.

Time-dependent perturbation theory

Here, treating the interaction Hamiltonian \hat{H}_{int} as a small perturbation, the full Hamiltonian can be separated as

$$\hat{H} = \hat{H}_0 + \hat{H}_{\text{int}} e^{-\epsilon|t|}, \quad (2.52)$$

where the unperturbed Hamiltonian $\hat{H}_0 = \hat{H}_{\text{rad}} + \hat{H}_{\text{el}}$ and the infinitesimal parameter $\epsilon > 0$ is introduced to ensure that the interaction term vanishes at $t \rightarrow \pm\infty$, in accordance with the adiabatic switching procedure.

In the limit before the interaction begins, assuming that the radiation field is in a single-mode $(\mathbf{k}_{\text{in}}, \lambda_{\text{in}})$ Fock state $|N_{\text{ph}}\rangle$ with N_{ph} photons (for simplicity) and the electronic system is in a general ground state given by $|\Psi_0^{N_{\text{el}}}\rangle$ with energy $E_0^{N_{\text{el}}}$, the initial state can be written as

$$|I\rangle = |N_{\text{ph}}\rangle |\Psi_0^{N_{\text{el}}}\rangle. \quad (2.53)$$

Since this is an eigenstate of \hat{H}_0 , the initial energy is

$$E_I = \omega_{\text{in}}(N_{\text{ph}} + \frac{1}{2}) + E_0^{N_{\text{el}}}. \quad (2.54)$$

By going to the interaction picture and applying time-dependent perturbation theory (see Refs. [105, 107] for more details and derivation), one obtains the following transition rate Γ_{FI} to go from initial state $|I\rangle$ to final state $|F\rangle$

$$\Gamma_{FI} = 2\pi\delta(E_F - E_I) \left| \langle F | \hat{H}_{\text{int}} | I \rangle + \sum_M \frac{\langle F | \hat{H}_{\text{int}} | M \rangle \langle M | \hat{H}_{\text{int}} | I \rangle}{E_I - E_M + i\epsilon} + \dots \right|^2. \quad (2.55)$$

Here $|F\rangle \neq |I\rangle$ is an eigenstate of \hat{H}_0 with eigenenergy E_F and $|M\rangle$ is an intermediate state which is also an eigenstate of \hat{H}_0 but with eigenenergy E_M . The delta function $\delta(E_F - E_I)$ ensures energy conservation is fulfilled. Only first- and second-order terms are shown in Eq. (2.55), but higher-order terms can also be computed. But, for one-photon absorption, only the first-order is relevant as discussed below.

One-photon absorption

The final state of the system after absorbing one photon can be written as

$$|F\rangle = |N_{\text{ph}} - 1\rangle |\Psi_F^{N_{\text{el}}}\rangle, \quad (2.56)$$

where the $|N_{\text{ph}} - 1\rangle$ is the final state of the radiation field which has one less photon than the initial state and $|\Psi_F^{N_{\text{el}}}\rangle$ is the final electronic state which has energy of $E_F^{N_{\text{el}}}$.

Since only one photon is annihilated, only first-order in perturbation theory from Eq. (2.55) is needed and in particular, only the ‘ $\mathbf{p} \cdot \mathbf{A}$ ’ term can cause this transition as it has the term containing a single photon annihilation operator $\hat{a}_{\mathbf{k},\lambda}$. Hence, the transition rate to absorb a photon in first-order is

$$\begin{aligned} \Gamma_{FI} &= 2\pi\delta(E_F^{N_{\text{el}}} - E_0^{N_{\text{el}}} - \omega_{\text{in}}) \left| \langle N_{\text{ph}} - 1 | \langle \Psi_F^{N_{\text{el}}} | \sum_{p,q} \sum_{\mathbf{k},\lambda} \sqrt{\frac{2\pi}{V\omega_{\mathbf{k}}}} \hat{c}_p^\dagger \hat{c}_q \right. \\ &\quad \left. \times \langle \varphi_p | e^{i\mathbf{k}\cdot\mathbf{x}} \mathbf{p} \cdot \boldsymbol{\epsilon}_{\mathbf{k},\lambda} | \varphi_q \rangle \hat{a}_{\mathbf{k},\lambda} | N_{\text{ph}} \rangle | \Psi_0^{N_{\text{el}}} \rangle \right|^2 \\ &= \frac{4\pi^2}{V\omega_{\text{in}}} N_{\text{ph}} \delta(E_F^{N_{\text{el}}} - E_0^{N_{\text{el}}} - \omega_{\text{in}}) \times \left| \sum_{p,q} \langle \varphi_p | e^{i\mathbf{k}_{\text{in}}\cdot\mathbf{x}} \mathbf{p} \cdot \boldsymbol{\epsilon}_{\mathbf{k}_{\text{in}},\lambda_{\text{in}}} | \varphi_q \rangle \langle \Psi_F^{N_{\text{el}}} | \hat{c}_p^\dagger \hat{c}_q | \Psi_0^{N_{\text{el}}} \rangle \right|^2 \end{aligned} \quad (2.57)$$

Defining the photon flux, which is the number of incident photons per unit time and unit area

$$J_{\text{ph}} = \frac{1}{\alpha} \frac{N_{\text{ph}}}{V}, \quad (2.58)$$

the photoabsorption cross section is given as

$$\begin{aligned} \sigma_F(\mathbf{k}_{\text{in}}, \lambda_{\text{in}}) &= \frac{\Gamma_{FI}}{J_{\text{ph}}} \\ &= \frac{\alpha 4\pi^2}{\omega_{\text{in}}} \delta(E_F^{N_{\text{el}}} - E_0^{N_{\text{el}}} - \omega_{\text{in}}) \left| \sum_{p,q} \langle \varphi_p | e^{i\mathbf{k}_{\text{in}}\cdot\mathbf{x}} \mathbf{p} \cdot \boldsymbol{\epsilon}_{\mathbf{k}_{\text{in}},\lambda_{\text{in}}} | \varphi_q \rangle \langle \Psi_F^{N_{\text{el}}} | \hat{c}_p^\dagger \hat{c}_q | \Psi_0^{N_{\text{el}}} \rangle \right|^2, \end{aligned} \quad (2.59)$$

which depends upon the photon energy, polarization and propagation direction \mathbf{k}_{in} .

In the independent-electron model, \hat{H}_{el} is approximated by the mean-field Hamiltonian \hat{H} , such that the initial state $|\Psi_0^{N_{\text{el}}}\rangle = |\Phi_0^{N_{\text{el}}}\rangle$ is the N_{el} ground state of \hat{H} . To obtain non-zero matrix elements in Eq. (2.59) after applying $\hat{c}_p^\dagger \hat{c}_q$ to $|\Phi_0^{N_{\text{el}}}\rangle$, the final state needs to be a particle-hole state with q being an occupied state (now labelled by i) and p being an unoccupied state (labelled by a). Hence, the final state is of the form $|\Phi_i^a\rangle = \hat{c}_a^\dagger \hat{c}_i |\Phi_0^{N_{\text{el}}}\rangle$. Thus, the photoabsorption cross section for an electron initially in orbital i transitioning to orbital a is

$$\sigma_i^a(\mathbf{k}_{\text{in}}, \lambda_{\text{in}}) = \frac{4\pi^2}{\omega_{\text{in}}} \alpha \delta(\epsilon_a - \epsilon_i - \omega_{\text{in}}) \left| \langle \varphi_a | e^{i\mathbf{k}_{\text{in}}\cdot\mathbf{x}} \mathbf{p} \cdot \boldsymbol{\epsilon}_{\mathbf{k}_{\text{in}},\lambda_{\text{in}}} | \varphi_i \rangle \right|^2. \quad (2.60)$$

Note that this equation is an approximation and the energies here are evaluated using \hat{H} instead of \hat{H}_{el} .

In the electric dipole approximation, $e^{i\mathbf{k}_{\text{in}}\cdot\mathbf{x}} \approx 1$, i.e. the dependence on the photon propagation direction vanishes. Furthermore, the transition matrix element in the so-called *velocity* form can be transformed as

$$\langle \varphi_p | \mathbf{p} \cdot \boldsymbol{\epsilon} | \varphi_q \rangle = -i(\epsilon_q - \epsilon_p) \langle \varphi_p | \mathbf{x} \cdot \boldsymbol{\epsilon} | \varphi_q \rangle, \quad (2.61)$$

where $\langle \varphi_p | \mathbf{x} \cdot \boldsymbol{\epsilon} | \varphi_q \rangle$ is the dipole transition matrix element in the *length* form. Using this and the electric dipole approximation, the photoabsorption cross section becomes

$$\sigma_i^a(\mathbf{k}_{\text{in}}, \lambda_{\text{in}}) = 4\pi^2 \omega_{\text{in}} \alpha \delta(\epsilon_a - \epsilon_i - \omega_{\text{in}}) |\langle \varphi_a | \mathbf{x} \cdot \boldsymbol{\epsilon}_{\mathbf{k}_{\text{in}}, \lambda_{\text{in}}} | \varphi_i \rangle|^2. \quad (2.62)$$

2.3 Quantum mechanics/molecular mechanics simulations

Performing quantum dynamics of large systems in the condensed phase is computationally unfeasible, since solving the time-independent Schrödinger equation to get the gradients for the dynamics grows exponentially with the number of atoms. An alternative is to use the quantum mechanics/molecular mechanics (QM/MM) method [99, 108], where only a small section is calculated using quantum mechanics (QM) and the rest is treated with classical force field molecular mechanics (MM). Figure 2.1 shows a QM/MM scheme to illustrate the separation between QM and MM regions. This is a useful technique to simulate chemical reactions where the effect of the environment can be important, such as in liquid phase reactions or photoexcitations in proteins (see Ref. [109] for more applications). In this section, first molecular mechanics is introduced and then different approaches to QM/MM are discussed.

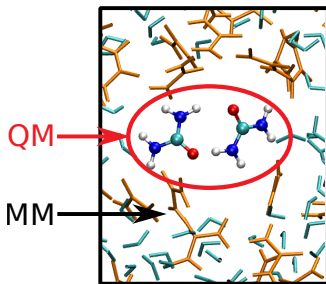


FIGURE 2.1: QM/MM scheme for a system in aqueous solution. Only a small portion of atoms are considered in the QM region and the rest are in the MM part.

2.3.1 Molecular mechanics

Classical ground state molecular dynamics (MD) using MM treats the atoms in a system with a "ball and spring" model, where the "balls" represent the atoms and the "springs" are the bonds between them. The nuclei are propagated using Newton's equation of motion

$$M_A \frac{d^2 \mathbf{R}_A(t)}{dt^2} = -\nabla_{\mathbf{R}_A} V_{\text{MM}}(\mathbf{R}(t)), \quad (2.63)$$

where the MM potential $V_{\text{MM}}(\mathbf{R}(t))$ is parameterized by [98]

$$V_{\text{MM}}(\mathbf{R}(t)) = V_b(\mathbf{R}(t)) + V_{\text{nb}}(\mathbf{R}(t)), \quad (2.64)$$

where $V_b(\mathbf{R}(t))$ and $V_{nb}(\mathbf{R}(t))$ are the bonding and non-bonding potentials, respectively. $V_b(\mathbf{R}(t))$ is given by

$$V_b(\mathbf{R}(t)) = \sum_{\text{bonds}} \frac{k_d}{2}(d - d_o)^2 + \sum_{\text{angles}} \frac{k_\theta}{2}(\theta - \theta_o)^2 + \sum_{\text{dihedrals}} \frac{k_\varphi}{2}(1 + \cos(n\varphi - \delta)), \quad (2.65)$$

where d , θ , and φ are the bond length, the angle between two bonds, and the dihedral angle for three adjacent bonds within a molecule, respectively. In Eq. (2.65), bonds and angles are modelled by harmonic potentials with k_d and k_θ as their respective force constants, and d_o and θ_o as their respective equilibrium values. Dihedral angles, on the other hand, are represented by periodic functions with k_φ and δ as its force constant and phase shift, respectively. The non-bonding potential $V_{nb}(\mathbf{R}(t))$ is described as a sum of Coulomb and Lennard-Jones potential for each pair of atoms, which describes electrostatic and van der Waals interaction, respectively,

$$V_{nb}(\mathbf{R}(t)) = \sum_{A < B} \left(\frac{q_A q_B}{d_{AB}} + 4\varepsilon_{AB} \left[\left(\frac{\sigma_{AB}}{d_{AB}} \right)^{12} - \left(\frac{\sigma_{AB}}{d_{AB}} \right)^6 \right] \right), \quad (2.66)$$

where q_A and q_B are the charges of atoms A and B , d_{AB} is the distance between them, σ_{AB} and ε_{AB} are the Lennard-Jones parameters. These required parameters, such as the force constants, charges, and Lennard-Jones parameters, are obtained through quantum chemistry calculations or experimental fitting and are summarized in force field files containing these parameters for each specific case. Some common force fields used are AMBER [110], CHARMM [111], OPLS [112].

This analytical form of force fields makes MM calculations extremely computationally efficient as opposed to *ab initio* MD. Hence, it has proven to be a powerful tool to model biological systems for understanding phenomena such as protein folding, DNA unzipping, and substrate transport through membrane [113]. However, since electrons are not treated explicitly in this approach, a general treatment of chemical reactions with bond dissociation and formation is not possible, even with more sophisticated force fields such as reactive force fields [114]. Furthermore, since it only describes the ground state of the system near equilibrium, excitation or ionization cannot be described.

2.3.2 Different QM/MM approaches

To resolve the issues with pure classical MM simulations and circumvent the computational cost of QM calculation, a hybrid method, namely QM/MM, can be used. This is especially useful in condensed phase systems where only a small portion needs to be described using QM where a reaction takes place, and the rest can be through MM which can act as a bath that still influences the QM dynamics. However, modelling the interaction between QM and MM regions can be a challenging task. Two distinct approaches to describe this interaction in QM/MM simulations are the subtractive and additive coupling schemes.

In the subtractive approach, the total potential is given by

$$V_{\text{tot}}(\mathbf{R}) = V_{\text{MM}}(\mathbf{R}) + V_{\text{QM}}(\mathbf{R}_{\text{QM}}) - V_{\text{MM}}(\mathbf{R}_{\text{QM}}), \quad (2.67)$$

where the nuclear positions \mathbf{R} are divided into \mathbf{R}_{QM} and \mathbf{R}_{MM} for the QM and MM regions, respectively, and V_{QM} and V_{MM} are the potentials calculated at QM and MM level, respectively. In Eq. (2.67), essentially the whole system is first evaluated at the MM level and then the MM potential for the QM atoms is replaced by the QM potential for these atoms. Hence, the interaction between the two regions is only at the force field level, making this approach quite simple. It lacks effects from the environment to the QM region such as polarization effects though. The ONIOM method [115, 116] is one of the most popular subtractive scheme methods.

Alternatively, one can use an additive scheme that explicitly takes into account the coupling between two regions with an interaction potential term $V_{\text{QM/MM}}(\mathbf{R})$, such that

$$V_{\text{tot}}(\mathbf{R}) = V_{\text{QM}}(\mathbf{R}_{\text{QM}}) + V_{\text{MM}}(\mathbf{R}_{\text{MM}}) + V_{\text{QM/MM}}(\mathbf{R}). \quad (2.68)$$

This coupling term can be described by mechanical [117] or electrostatic embedding [118] scheme. The interaction between the two regions is modelled by force fields in the mechanical scheme, hence also does not include polarization effects. On the other hand, in the electrostatic embedding scheme, the charges from the MM atoms are included explicitly in the QM calculations, allowing it to include polarization from the environment. Going even further, the polarization of the MM region due to the effect of the QM region can also be included [119]. See Ref. [120] for a more detailed overview of these different approaches.

2.4 Path integral methods

So far we focused on the use of classical nuclei due to computational efficiency reasons. However, this lacks nuclear quantum effects such as zero-point energy (ZPE) and tunneling which can be important in some cases, for instance in proton transfer reactions as these involve light atoms. One approximate way of adding these is by semi-classical dynamics involving Feynman's imaginary time path integral approach [89]. In this section, path integral molecular dynamics (PIMD) is first introduced which is used to evaluate static properties with quantum effects of a system in thermal equilibrium. Then, ring polymer molecular dynamics (RPMD) is discussed which builds upon PIMD to get approximated real-time quantum dynamics.

2.4.1 Path Integral Molecular Dynamics

The Hamiltonian for one nuclear DOF and a single electronic state is

$$\hat{H} = T_N(\hat{P}) + V(\hat{R}), \quad (2.69)$$

where \hat{P} and \hat{R} are the nuclear momentum and position operators, respectively, and the nuclear kinetic and potential energies are T_N and V (same as \hat{H}_{el} from before but just written differently for ease of notation), respectively. In this section, only one nuclear DOF is considered for simplicity; however, generalization to a system of distinguishable particles with multiple DOFs can easily be done.

Static properties of a system in thermal equilibrium can be obtained through the partition function

$$Z = \text{Tr} \left[e^{-\beta \hat{H}} \right], \quad (2.70)$$

where β is the inverse equilibrium temperature. By evaluating the trace in Eq. (2.70) in the position basis, employing the symmetric Trotter product (since \hat{T}_N and \hat{V} do not commute), and inserting identity operators in position and momentum basis $\hat{1} = \int dR |R\rangle \langle R| = \int dP |P\rangle \langle P|$, one obtains

$$\begin{aligned} Z &= \lim_{n \rightarrow \infty} Z_n \\ &= \lim_{n \rightarrow \infty} \left(\frac{1}{2\pi} \right)^n \int d\{P^{(\alpha)}\} \int d\{R^{(\alpha)}\} e^{-\beta_n H_n(\{R^{(\alpha)}\}, \{P^{(\alpha)}\})}, \end{aligned} \quad (2.71)$$

where $R^{(\alpha)}$ and $P^{(\alpha)}$ are the position and momentum, respectively, of a so-called ring polymer bead labelled by α with n being the number of beads or replicas of the system, $\int d\{R^{(\alpha)}\}$ means $\int dR^{(1)} \dots \int dR^{(n)}$, and $\beta_n = \frac{\beta}{n}$. This formulation of the partition function is still exact in the limit $n \rightarrow \infty$ and thus casts the quantum Z into a classical object through this classical isomorphism [121]. Note that the bead momenta are reinserted in Eq. (2.71) to perform molecular dynamics for sampling the phase space, resulting in the PIMD formulation [122]. If the momenta are left out, sampling the integrals can still be done using Monte Carlo methods which gives the path integral Monte Carlo (PIMC) method [123]. Both methods enable one to obtain exact static quantum properties from classical quantities. In PIMD, the sampling is done through the so-called ring polymer Hamiltonian which is also a classical object and is given as

$$H_n(\{R^{(\alpha)}\}, \{P^{(\alpha)}\}) = \sum_{\alpha=1}^n \left(\frac{(P^{(\alpha)})^2}{2M} + \frac{1}{2} M \omega_n^2 (R^{(\alpha)} - R^{(\alpha+1)})^2 + V(R^{(\alpha)}) \right) \quad (2.72)$$

where M is the nuclear mass, $\omega_n = \frac{1}{\beta_n}$ and index $\alpha = n + 1$ is interpreted as index $\alpha = 1$. The centroid position \bar{R} and momentum \bar{P} are given by the average of those quantities over all n beads. To sample the phase space in Eq. (2.71), the bead positions and momenta are propagated using classical Hamilton's equations of motion for each bead

$$\begin{aligned} \dot{R}^{(\alpha)} &= \frac{\partial H_n}{\partial P^{(\alpha)}} = \frac{P^{(\alpha)}}{M}, \\ \dot{P}^{(\alpha)} &= -\frac{\partial H_n}{\partial R^{(\alpha)}} = M \omega_n^2 (R^{(\alpha+1)} + R^{(\alpha-1)} - 2R^{(\alpha)}) - \frac{\partial V(R^{(\alpha)})}{\partial R^{(\alpha)}}. \end{aligned} \quad (2.73)$$

Any observable that is a function of position $\hat{A}(R)$ can be calculated in PIMD through

$$\begin{aligned}\langle \hat{A}(R) \rangle &= \frac{1}{Z} \text{Tr} [\hat{A}(R) e^{-\beta \hat{H}}] \\ &\simeq \frac{1}{(2\pi)^n Z_n} \int d\{P^{(\alpha)}\} \int d\{R^{(\alpha)}\} A_n(\{R^{(\alpha)}\}) e^{-\beta_n H_n}\end{aligned}\quad (2.74)$$

where $A_n(\{R^{(\alpha)}\}) = \frac{1}{n} \sum_{\alpha=1}^n A(R^{(\alpha)})$ is known as the estimator. Note that the observables obtained are also exact in the limit $n \rightarrow \infty$, but in practice, n is chosen till results converge. For observables that are a function of momenta, the estimator can be a bit more complicated and are possible by either taking derivatives of position operators or from a statistical property using the partition function such as one for energy (see Ref. [124] for more details on estimators for various quantities). PIMD and PIMC have been widely used to study condensed phase systems from aqueous and biological systems to material science (see Refs. [125, 126] for different applications).

2.4.2 Ring polymer molecular dynamics

RPMD [88] extends PIMD to get approximated real-time quantum correlation functions, which in standard form for two operators \hat{A} and \hat{B} is given as

$$\begin{aligned}C_{AB}(t) &= \langle \hat{A}(0) \hat{B}(t) \rangle \\ &= \frac{1}{Z} \text{Tr} [\hat{A}(0) \hat{B}(t) e^{-\beta \hat{H}}]\end{aligned}\quad (2.75)$$

where $\hat{B}(t) = e^{i\hat{H}t} \hat{B}(0) e^{-i\hat{H}t}$. This can be used to calculate quantities such as diffusion and reaction rate constants, and infrared absorption spectra. An alternative form of correlation functions is the more symmetric Kubo-transformed form [127]

$$\tilde{C}_{AB}(t) = \frac{1}{\beta Z} \int_0^\beta d\lambda \text{Tr} [e^{-(\beta-\lambda)\hat{H}} \hat{A}(0) e^{-\lambda\hat{H}} \hat{B}(t)].\quad (2.76)$$

These two correlation functions are related to each other by the following relation

$$G_{AB}(\omega) = \frac{\beta\omega}{1 - e^{-\beta\omega}} \tilde{G}_{AB}(\omega)\quad (2.77)$$

where $G_{AB}(\omega)$ and $\tilde{G}_{AB}(\omega)$ are Fourier transforms of $C_{AB}(t)$ and $\tilde{C}_{AB}(t)$, respectively. By evolving the bead positions and momenta using the same Hamiltonian from Eq. (2.72), one gets the following approximated correlation function for RPMD [88]

$$\langle \hat{A}(0) \hat{B}(t) \rangle \simeq \frac{1}{(2\pi)^n Z_n} \int d\{P^{(\alpha)}\} \int d\{R^{(\alpha)}\} A_n(0) B_n(t) e^{-\beta_n H_n},\quad (2.78)$$

which is argued to be comparable to the Kubo transformed one from Eq. (2.76) due to the similar symmetries in both.

Although the dynamics are approximate and only exact in certain limits such as short time, harmonic, and high-temperature limits, RPMD has been shown to accurately incorporate nuclear quantum effects in computing reaction rate constants and diffusion rates [128–131]. Furthermore, RPMD, which performs classical dynamics with quantum statistics, still preserves the quantum Boltzmann distribution over the dynamics, hence there is no ZPE leakage problem [132]. Recently, RPMD was shown to stem from Matsubara dynamics [133, 134] which is a more rigorously derived and accurate method but is rather computationally expensive. However, retrieving RPMD requires approximations whose physical reasonings are not clear yet. RPMD has also been extended to non-equilibrium cases involving vertical excitation and momentum kick [135], with recent applications to calculating state-to-state reaction cross sections [136–138]. Non-equilibrium dynamics involve initial equilibrium sampling using one Hamiltonian and propagation using a different one. A further important extension in the scope of this thesis is nonadiabatic dynamics using RPMD. The aim is to capture nuclear quantum effects in quantum-classical dynamics for the multistate case. This has been attempted by combining RPMD with FSSH [90, 139] and the Meyer-Miller-Stock-Thoss (MMST) mapping approach [140–142]. Each of these methods have their drawbacks though.

Chapter 3

Ultrafast time-resolved x-ray absorption spectroscopy of ionized urea and its dimer in vacuum

This chapter is based on the following published manuscript with minor changes to fit the thesis structure:

- Yashoj Shakya, Ludger Inhester, Caroline Arnold, Ralph Welsch, and Robin Santra, "Ultrafast time-resolved x-ray absorption spectroscopy of ionized urea and its dimer through ab initio nonadiabatic dynamics", *Structural Dynamics* **8**, 034102 (2021). <https://doi.org/10.1063/4.0000076>

I performed the simulations, did the data analysis, and wrote the manuscript under the supervision of Ludger Inhester and Robin Santra. In particular, I performed ionized state simulations and the XAS spectra calculations using the in-house developed codes CDTK and XMOLECULE, where I extended CDTK to generate TRXAS spectra for any general molecule using absorption cross sections from XMOLECULE. I also conducted the analysis of the data including analysing proton transfer reaction and statistical analysis using a machine learning technique, namely PLSR.

3.1 Introduction

The response of biological matter to ionizing radiation is of fundamental interest to many fields, ranging from radiation oncology [143], x-ray diffraction imaging [144], and human space flight [145]. The dynamics in a molecule that are triggered by the formation of deep valence holes, i.e., by ionization beyond the highest occupied molecular orbital (HOMO), are of particular relevance for highly energetic ionizing radiation. Deep valence holes can be caused either by the direct interaction with extreme ultraviolet light or by secondary ionizations, e.g., by photo- or Auger electrons following core level ionization [146–149]. Upon ionization, the molecule undergoes chemical dynamics that involve conversion of the electronic excitation energy to vibrational energy through nonadiabatic couplings of electronic potential energy surfaces (PES).

With the advent of x-ray free-electron lasers (XFEL) and the recent progress in high harmonic generation (HHG) technology offer new routes to investigate the

ultrafast dynamics triggered by such ionization events in molecules. In particular, a promising tool to investigate ultrafast structural dynamics on a femtosecond timescale is time-resolved x-ray absorption spectroscopy (TRXAS), where the ultrafast dynamical changes initiated by an ionizing or exciting light pulse are probed with a delayed, ultra-short x-ray pulse. Complementary to the wide range of experimental methods that have been used to study the femtosecond dynamics of molecules[3, 26], TRXAS has the advantage that the probe acts locally on a specific atomic site in the molecule since the dominant interactions occur with the core orbitals in the molecule. Different atoms with distinct inner-shell binding energies thus provide separate time-resolved absorption signals that cover different local aspects of the dynamics of the molecule.

The capabilities of TRXAS in probing structural and electronic dynamics on a femtosecond timescale have been demonstrated in several experiments at large XFEL facilities [30–35] and in laboratory setups employing HHG [23, 24, 28]. Interpreting the TRXAS signals is, however, usually not trivial and often relies crucially on theoretical modelling. In this context, a number of theoretical works have provided valuable insight into the dynamics following ionization or excitation of a sample molecule and how they can be revealed from TRXAS [36–41].

Depending on the initial excitation level, the triggered dynamics can involve a large number of different PES [36]. Hence, with increasing system size, simulating the dynamics and calculating the resulting TRXAS can become rather computationally involved, thus posing a strong challenge for theoretical modelling. A relatively affordable, yet reasonably accurate, approach is to employ the fewest switches surface hopping method [66] in combination with PES provided by Koopmans’ theorem [35, 36, 40, 150, 151].

In this chapter, I present a computational study on the TRXAS of urea and its dimer. Due to its use as a fertilizer, urea is a highly relevant molecule for industry and agriculture. Its first synthesis by Wöhler [152] is often considered a foundational milestone in organic chemistry [153]. As an amide with a planar structure, it has similarities with proteins and thus can be seen as a simplified building block of a biological molecule. Moreover, the urea dimer is linked via hydrogen bonds whose specific role in TRXAS has not yet been studied. I performed on-the-fly *ab initio* nonadiabatic dynamics simulations following instantaneous HOMO and deeper valence ionization of urea and its dimer, and calculated the TRXAS at the carbon (C), nitrogen (N), and oxygen (O) *K*-edges. Using these results, I demonstrate how statistical analysis can provide a clear interpretation of features in the TRXAS with respect to structural dynamics in the molecule. Furthermore, I reveal pronounced fingerprints of nonadiabatic relaxation and proton transfer reaction in the TRXAS.

This chapter is structured as follows: first, I briefly explain the computational methodology in Sec. 3.2. In Sec. 3.3, I present and discuss the results for the urea monomer and dimer. Then I summarize the main findings in Sec. 3.4.

3.2 Computational method

I performed on-the-fly *ab initio* molecular dynamics on multiple coupled electronic PES employing the methodology used in Refs. [35, 40]. Electronic structure calculations at a particular molecular geometry have been performed using the XMOLECULE package (rev. 3700) [154, 155] at the Hartree-Fock (HF) level of theory with the 6-31+G* basis set [156–159]. I also performed calculations with the smaller 6-31G basis set which gives qualitatively similar results. The ionized system was described by Koopmans’ theorem, which gives the energy of a state with a hole in the i -th orbital as $E_i = E_{\text{HF}} - \epsilon_i$, where ϵ_i is the energy of the i -th orbital and E_{HF} is the HF ground-state energy of the neutral molecule. This approach provides a computationally efficient, yet reasonable, description of the valence shell ionized system and was previously used to study the dynamics of other ionized systems [35, 36, 40, 150, 151]. Although the accuracy is certainly limited, the employed scheme has the potential to be applied also to larger molecules, since it essentially only involves HF calculations. Due to its simplicity, it can also straightforwardly be applied to the ionization of deeply bound valence orbitals where the ensuing relaxation dynamics involve a large number of different PES. [36]

In the calculations, the gradients of the PES and the nonadiabatic coupling vectors between the different ionized states were obtained by solving the coupled perturbed Hartree-Fock equations in XMOLECULE [40, 160–162].

The molecular dynamics simulations on the ionized states were performed using Tully’s fewest switches surface hopping method [66]. In this quantum-classical approach, the nuclei are treated classically on a single PES. At each time step, there is a probability to hop to another surface based on the coherent evolution of an electronic wavefunction. The propagation of the quantum electronic wave packet is done by solving the time-dependent Schrödinger equation simultaneously along with the classical propagation of the nuclear geometry.

Initial positions and momenta were obtained by sampling the Wigner distribution of the ground vibrational state of the neutral molecule, employing the harmonic approximation. An ensemble of 100 samples was created and then propagated starting in a selected valence-ionized electronic state for a total time of 300 fs using a simulation time step of 0.5 fs.

Along each trajectory, I calculated the time-dependent x-ray absorption spectra. Given the element specificity of core orbitals, one can probe the dynamics of the molecule through different inner-shell edges in the x-ray absorption spectra, reflecting different local environments in the molecule. Here, I consider the C, N, and O K -edges, whose binding energies are around 289 eV, 399 eV, and 535 eV, respectively [163]. More specifically, I addressed the energetically lowest absorption resonance that can be found below the ionization threshold and can be associated with the refilling of the previously created valence hole from the respective core orbital. Such an absorption

resonance is thus only present in the ionized molecule, which in a prospective pump-probe experiment has the advantage that the signal from pumped molecules can be distinguished from the background signal of non-pumped, neutral molecules.

For an electron in the core orbital ϕ_i with orbital energy ϵ_i being excited to the valence orbital vacancy ϕ_f with orbital energy ϵ_f , the cross section was calculated using [105]

$$\sigma(\omega) = \frac{4}{3}\pi^2\omega\alpha \delta(\epsilon_f - \epsilon_i - \omega) |\langle \phi_f | \hat{\mathbf{d}} | \phi_i \rangle|^2, \quad (3.1)$$

where ω is the photon energy of the x-ray probe pulse, α is the fine structure constant, and $\hat{\mathbf{d}}$ is the dipole vector, which in Eq. (3.1) is averaged over the three spatial dimensions. The quantities in Eq. (3.1) are given in atomic units (a.u.) and is the same as Eq. (2.62), apart from the averaging over three dimensions. For the function $\delta(E - \omega)$, I employed a finite-width line profile given by a Lorentzian function with a width of 100 meV to account for the natural line width of the core-ionized state.

Note that the energetic positions of the absorption resonances, here calculated by $\epsilon_f - \epsilon_i$, are several eVs off from realistic values. This is mostly due to orbital relaxation effects accompanying core shell ionization that are not taken into account in the Koopmanns' approach. To correct for this effect, I down-shifted the calculated absorption spectra by 21 eV, 25 eV, and 24 eV for the C, N, and O *K*-edges, respectively. These shifts have been estimated from the difference between the calculated orbital binding energies and the experimental *K*-edge ionization potentials [163].

3.3 Results

3.3.1 Urea

For the urea molecule (schematic shown in Fig. 3.1(a)), I have considered initial ionization in the HOMO, HOMO-1, and HOMO-2. The orbitals are depicted in Figs. 3.1(c)-3.1(e). Figure 3.1(b) shows the corresponding binding energy histogram for the molecular geometries in the considered ground-state Wigner distribution. As can be seen, HOMO, HOMO-1, and HOMO-2 lie relatively close to each other in binding energy within the range between 11 eV and 13 eV. The computed binding energies are somewhat higher than the values from experimental data reporting 10.28 eV and 10.78 eV for the first two ionization potentials [164]. As the binding energies overlap, one can expect that ionization of HOMO-1 or HOMO-2 leads to a rapid internal conversion via nonadiabatic dynamics towards the electronic ground state with a hole in HOMO. Additionally, these hole states are below the double ionization potential (~ 30 eV as estimated from a Δ SCF calculation at the equilibrium geometry) and therefore do not undergo autoionization processes.

TRXAS

Figure 3.2 shows the evolution of the three calculated x-ray absorption spectra after removing an electron from HOMO, HOMO-1, and HOMO-2, respectively. Compared

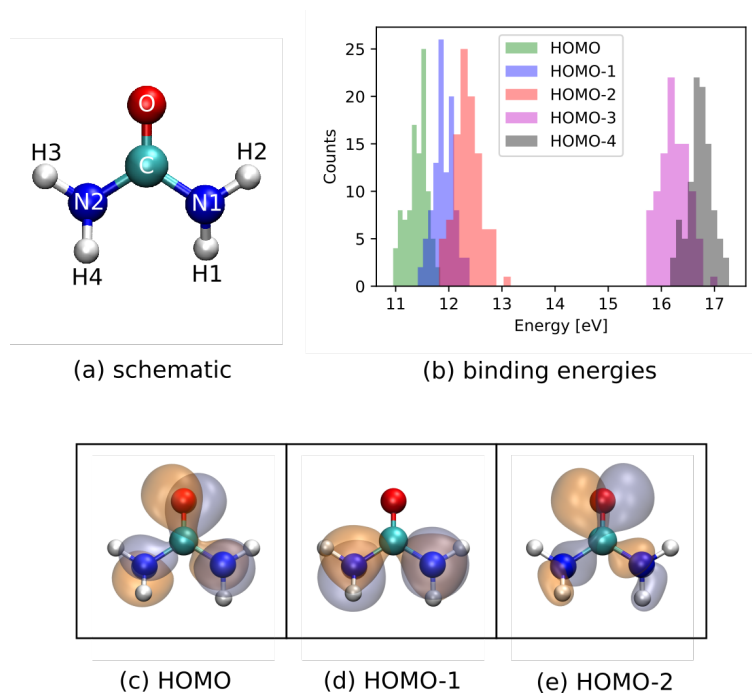


FIGURE 3.1: (a) Schematic of urea. (b) Histogram of the calculated molecular orbital binding energies for HOMO to HOMO-4 for the ground-state Wigner distribution of neutral urea. (c)-(e) HOMO, HOMO-1, and HOMO-2 at equilibrium geometry, visualized using VMD [165]. Figure taken from Ref. [44].

to the N and O K -edges, the absorption at the C K -edge is considerably weaker, since the three considered valence orbitals only have a small amplitude on the C atom (see Fig. 3.1).

The three element-selective absorption spectra for an initial hole in HOMO [Figs. 3.2(a)-3.2(c)] exhibit oscillations in energy, in particular for the C and N K -edge absorption resonances during the first 50 fs. I attribute these oscillations to vibrations initiated by ionization. Such oscillations are not visibly observed for deeper hole states [Figs. 3.2(d)-3.2(i)], where nonadiabatic relaxation effects and higher vibrational energy lead to a rapid decay of vibrational coherence. Along the same line, one can understand that the absorption resonances are considerably broader after initial ionization in HOMO-1 or HOMO-2 as compared to initial ionization in HOMO. Moreover, the spectra for the deeper hole states exhibit a blueshift of 1–2 eV at times ~ 20 fs that is not present in the spectrum following HOMO ionization.

To investigate the intensity variation in more detail, Fig. 3.3 shows the absorption signal integrated over the energy range shown in Fig. 3.2. As seen for the initial HOMO and HOMO-1 holes [Figs. 3.3(a) and 3.3(b)], the energy-integrated spectra oscillate for the first 100 fs with a similar period as the oscillations seen in the energetic peak positions at the C and N K -edges for an initial HOMO hole state [Figs. 3.2(a) and 3.2(b)]. Apart from these oscillations, the energy-integrated spectra stay rather constant. In contrast, the absorption intensity at the N K -edge following ionization of HOMO-2 shows an overall increment in the first 100 fs, mirrored by a corresponding

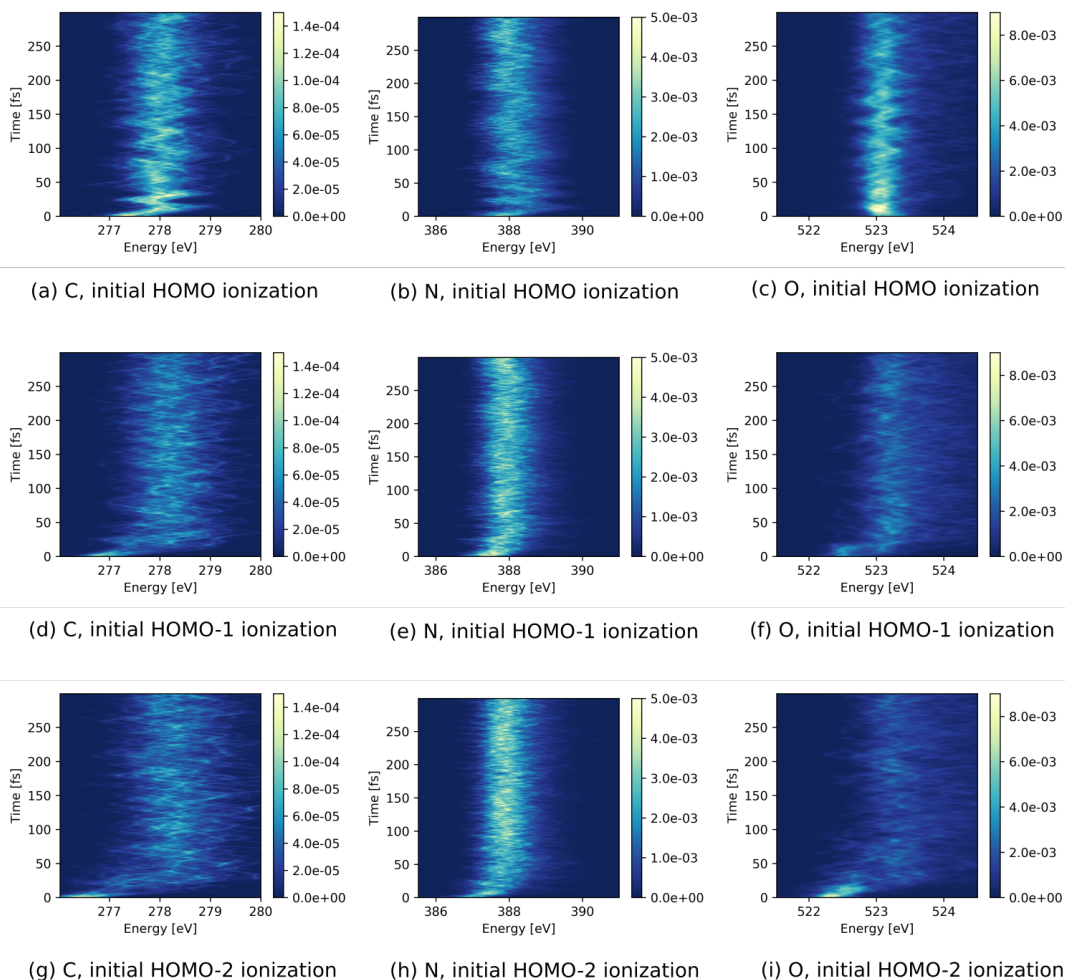


FIGURE 3.2: TRXAS (given by cross sections in a.u.) of urea after initial ionization of (a)-(c) HOMO, (d)-(f) HOMO-1, and (g)-(i) HOMO-2 at the lowest (left) C, (middle) N, and (right) O K -edge absorption resonances. Figure taken from Ref. [44].

decrement in the absorption intensity at the O K -edge [Fig. 3.3(c)]. For all three cases, Fig. 3.3 indicates a strict anti-correlation between the temporal variations in the absorption intensities at the N and O K -edges.

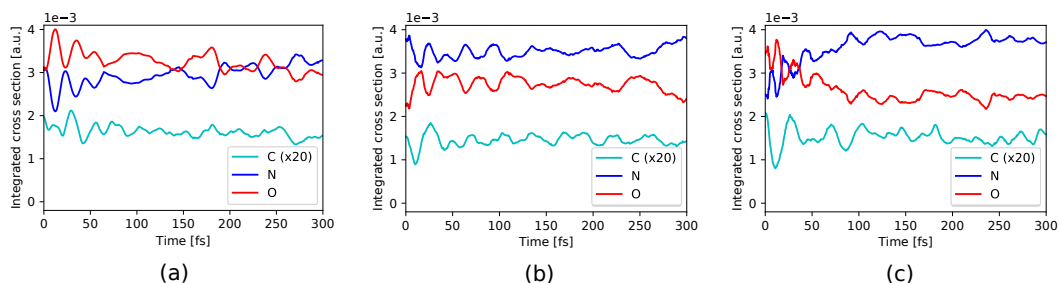


FIGURE 3.3: Energy-integrated spectra of urea from Fig. 3.2 for the C (scaled by 20), N, and O $1s$ pre-edge resonances following initial ionization of (a) HOMO, (b) HOMO-1, and (c) HOMO-2. Figure taken from Ref. [44].

The observed temporal changes in the TRXAS for initial holes in HOMO-1 and

HOMO-2 can be partially attributed to the electronic relaxation dynamics due to nonadiabatic effects. Figure 3.4 shows the population of the relevant electronic states as a function of time. As can be seen in Fig. 3.4(a), the HOMO-1 valence hole decays electronically on a timescale of ~ 20 fs. The HOMO-2 hole state [Fig. 3.4(b)] decays rapidly towards the HOMO-1 hole state, losing half of its population within ~ 5 fs, followed by a further decay leading to an almost complete relaxation to the HOMO-hole state by ~ 100 fs. Since the HOMO-2 has dominant contributions on the O atom whereas the HOMO-1 is rather concentrated on the two N atoms (see Figs. 3.1(d) and 3.1(e)), the electronic relaxation step from the hole in HOMO-2 to the hole in HOMO-1 is reflected by the rapid decay of the O absorption signal and the corresponding increase in the N absorption signal [Fig. 3.3(c)]. Along with the reported electronic relaxations, the binding energy of the valence hole decreases, and therefore the energetic gap to the core shells increases. The observed increase in the energetic position of the absorption resonances [Figs. 3.2(d)-3.2(i)] can thus be directly linked to these electronic relaxations.

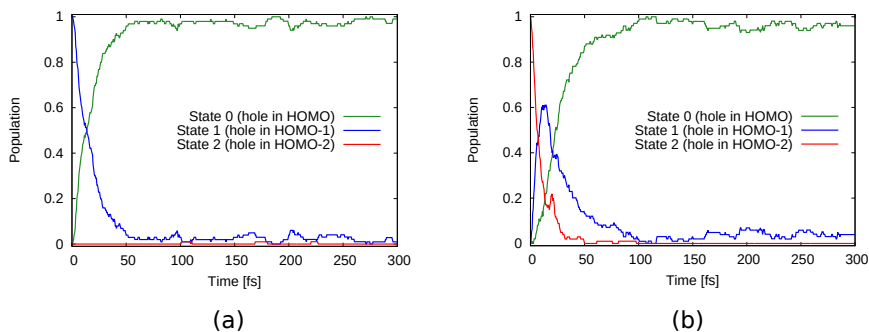


FIGURE 3.4: Electronic state population over time for urea with an initial hole in (a) HOMO-1 and (b) HOMO-2. Figure taken from Ref. [44].

Identifying collective coordinates

Beyond interpreting the TRXAS via electronic relaxation processes, further insight can be obtained by understanding the spectral variations also in terms of structural changes. To that end, I inspected the correlation of a complete set of internal coordinates with the three corresponding absorption intensities (note that the intensities from the two N atoms are summed up). I restrict this analysis to the trajectories with the initial hole in HOMO. However, the results can also be transferred to ionization of deeper valence orbitals, since the electronic states decay rapidly into the ground state of the cation. A similar analysis using the energetic positions of the absorption resonances instead of their intensities was employed before in Ref. [41], demonstrating how specific molecular vibrations can be linked to variations in the line positions. Figure 3.5(a) shows the Pearson correlation coefficients for the absorption intensities with the 10 internal coordinates showing the largest (anti-)correlation. It can clearly be seen that the interatomic distances C-O, N1-C, and N2-C, and the angle N1-C1-N2 are

the internal coordinates that show the strongest correlation or anti-correlation with the absorption intensities at the N and O *K*-edges. As already mentioned before (see Fig. 3.3(a)), there is a strong anti-correlation between the N and O signal intensities, which is reflected in the opposite sign of the correlation coefficients in Fig. 3.5(a). The absorption intensity at the C *K*-edge is rather correlated with the hydrogen angles C-N1-H1, C-N2-H4, and H1-N1-H2 as well as the interatomic distance C-O and the angle N1-C-N2.

To obtain a consistent picture of the correlations between absorption intensities and molecular vibrations, I conducted a statistical analysis using a machine learning technique, namely partial least square regression (PLSR) [166], to find collective internal coordinates that maximize the covariance between the geometrical parameters and the absorption intensities. This way the two collective internal coordinates were identified that are shown in Fig. 3.5(b) and 3.5(c), one linked to the absorption intensity at the N and O *K*-edges, and the other at the C *K*-edge. Accordingly, the variation in the N and O absorption signals can be connected to a collective coordinate predominantly consisting of C-O bond stretching and N1-C-N2 angle opening that explains 77% of the variance in the absorption intensities (which is the R^2 score). Note that this motion represents only 10% of the total variation in the geometry, which is mostly dominated by hydrogen vibrations that do not significantly affect the intensities at the N and O *K*-edges. The impact of the obtained collective vibration on the absorption can be rationalized by the mechanism that stretching of the C-O bond causes the valence hole to be localized on the O atom. Hence, this leads to an increase in the absorption signal at the O *K*-edge and a decrease at the N *K*-edge (see Fig. 3.5(b)). Similarly, the variation in the C absorption signal can be attributed to the collective motion illustrated in Fig. 3.5(c), which is mostly a correlated bending in the NH₂ groups and to a lower extent an elongation of the C-O bond. This coordinate explains 30% of the variance in the absorption intensity and contributes 7% to the total variation in the geometry. As can be seen in Fig. 3.5(c), this bending motion deforms the HOMO, slightly shifting its contribution towards the C atom. The strong correlation of the respective time-dependent intensities with the two collective coordinates are illustrated in Figs. 3.5(d) and 3.5(e), which compare the evolution of the obtained coordinates with the change in their respective standardized absorption intensities.

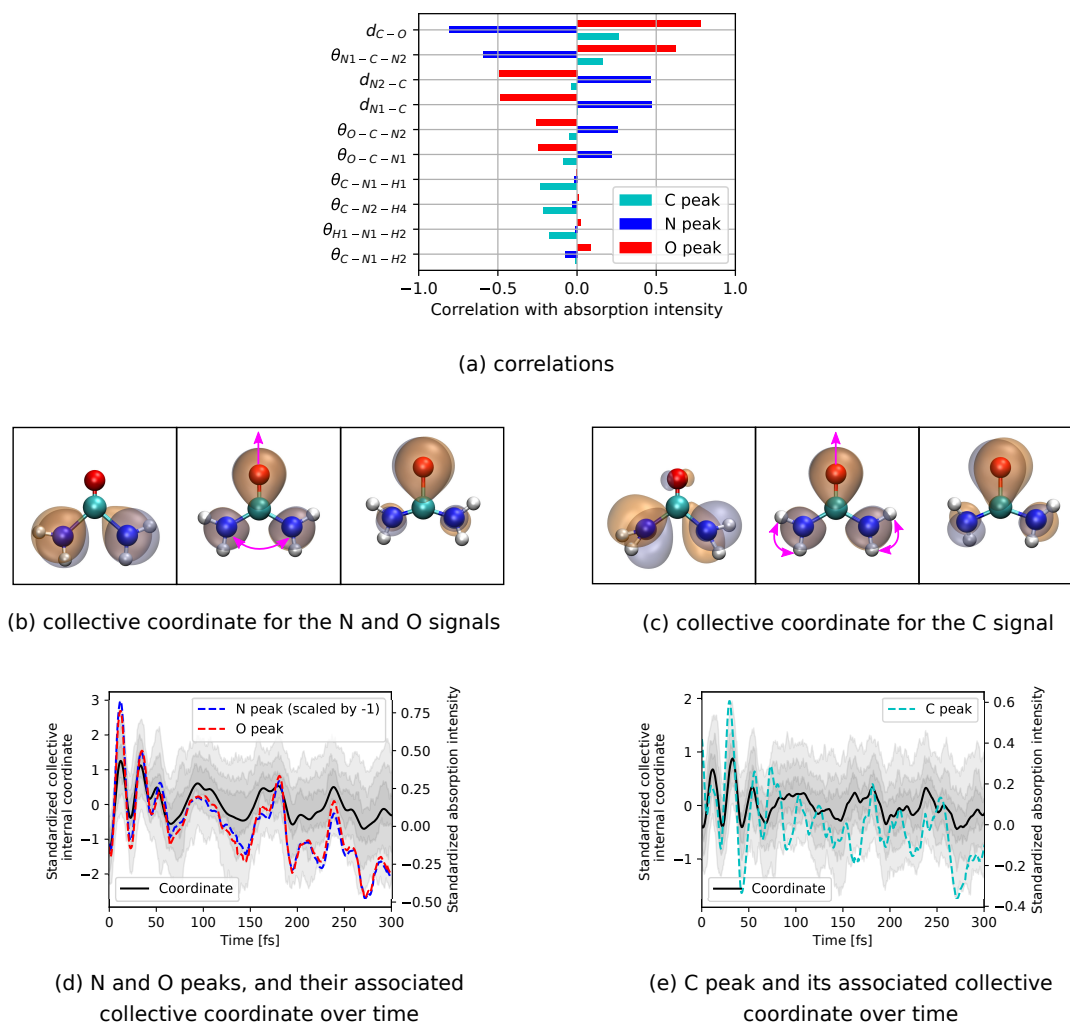


FIGURE 3.5: (a) Pearson correlation coefficients between internal coordinates of urea and absorption intensities at the C, N, and O K -edges for initial HOMO ionization. HOMO along the collective internal coordinate motion attributed to the temporal intensity variations (b) in the N and O peaks, and (c) in the C peak. Temporal evolution of the collective coordinate along with the averaged standardized absorption intensity for (d) the N and O peaks, and (e) the C peak. The shaded areas indicate regions between percentiles (37.5%–67.5%, 25%–75%, and 12.5%–87.5%) of the coordinate distributions. Figure taken from Ref. [44].

3.3.2 Urea dimer

Having understood how TRXAS features link to the ionization-induced dynamics of the urea monomer, I now turn to its dimer. Specifically, I address here a cyclic urea dimer conformer, where the monomers exhibit two hydrogen bonds with each other leading to a more stable structure than the alternative linear conformers [167]. Analogous to the monomer case, the binding energies of the orbitals up to HOMO-5 are relatively close in energy [Fig. 3.6(a)]. The molecular geometry of the considered conformer is depicted in Figs. 3.6(b)-3.6(g) together with the molecular orbitals HOMO to HOMO-5.

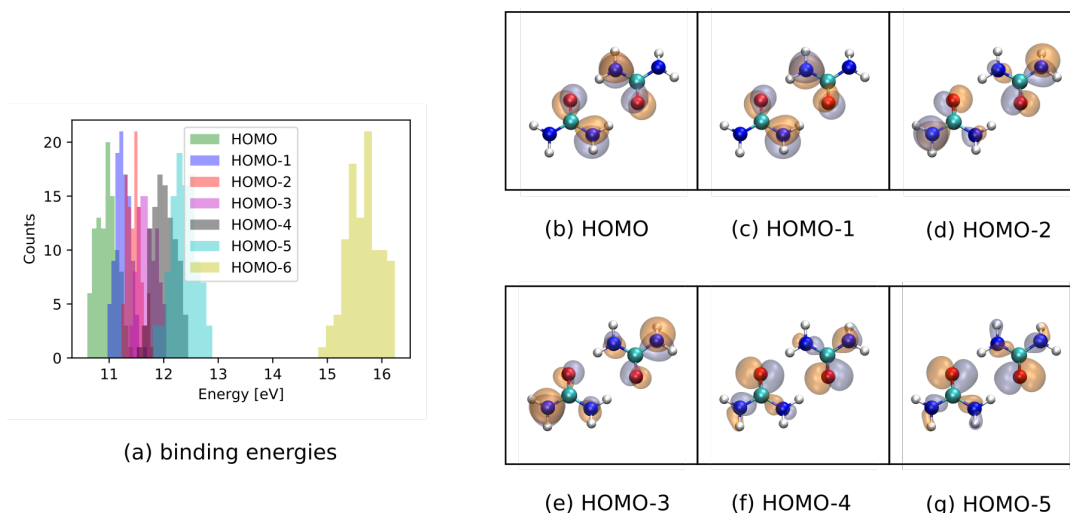


FIGURE 3.6: (a) Histogram of the calculated molecular orbital binding energies for HOMO to HOMO-6 for the ground-state Wigner distribution of neutral urea dimer. (b)-(g) HOMO to HOMO-5 at equilibrium geometry, visualized using VMD [165]. Figure taken from Ref. [44].

TRXAS

Figure 3.7 shows the time evolution of the x-ray absorption spectra for various valence hole states in the ionized dimer. Here, I only show the TRXAS for an initial hole in HOMO, HOMO-3, and HOMO-5 as exemplars. The spectra for HOMO-1, HOMO-2, and HOMO-4 show similar features to the ones shown in Fig. 3.7. For all three initial valence holes, a pronounced change in absorption intensity at the C K -edge (see Figs. 3.7(a), 3.7(d), and 3.7(g)) is seen. In particular, the very weak absorption signal becomes continuously stronger on a timescale of ~ 100 fs. This increment is accompanied by a blueshift in the energetic position of the absorption line. In the absorption intensity at the O K -edge [Fig. 3.7(c)], there is a suppression of intensity occurring for the initial HOMO hole at ~ 50 fs. For an initial hole in HOMO, a transient redshift in energy at ~ 75 fs can be seen in the N absorption resonance position [Fig. 3.7(b)], which is absent for the deeper hole states.

As can be seen from the monomer, the TRXAS for the initial holes in HOMO-3 and HOMO-5 [Figs. 3.7(d)-3.7(i)] show spectral shifts in the absorption energy for all three edges at ~ 20 fs and ~ 40 fs for HOMO-3 and HOMO-5, respectively. For the HOMO-5 hole, the spectral shift is accompanied by a decline in the O absorption intensity [Fig. 3.7(i)].

The electronic state population dynamics for initial HOMO-3 and HOMO-5 holes are shown in Fig. 3.8. As can be seen for the two initial hole states, the electronic state rapidly relaxes to a state with a hole in HOMO-1 at ~ 20 fs and ~ 40 fs, respectively. This is followed by a further decay to the HOMO hole state at ~ 40 fs and ~ 60 fs, respectively. These timescales confirm the assignment of the spectral shifts in Figs. 3.7(d), 3.7(f), 3.7(g), and 3.7(i) to nonadiabatic relaxations. Around 100 fs after ionization almost all of the excited electronic state population has eventually relaxed

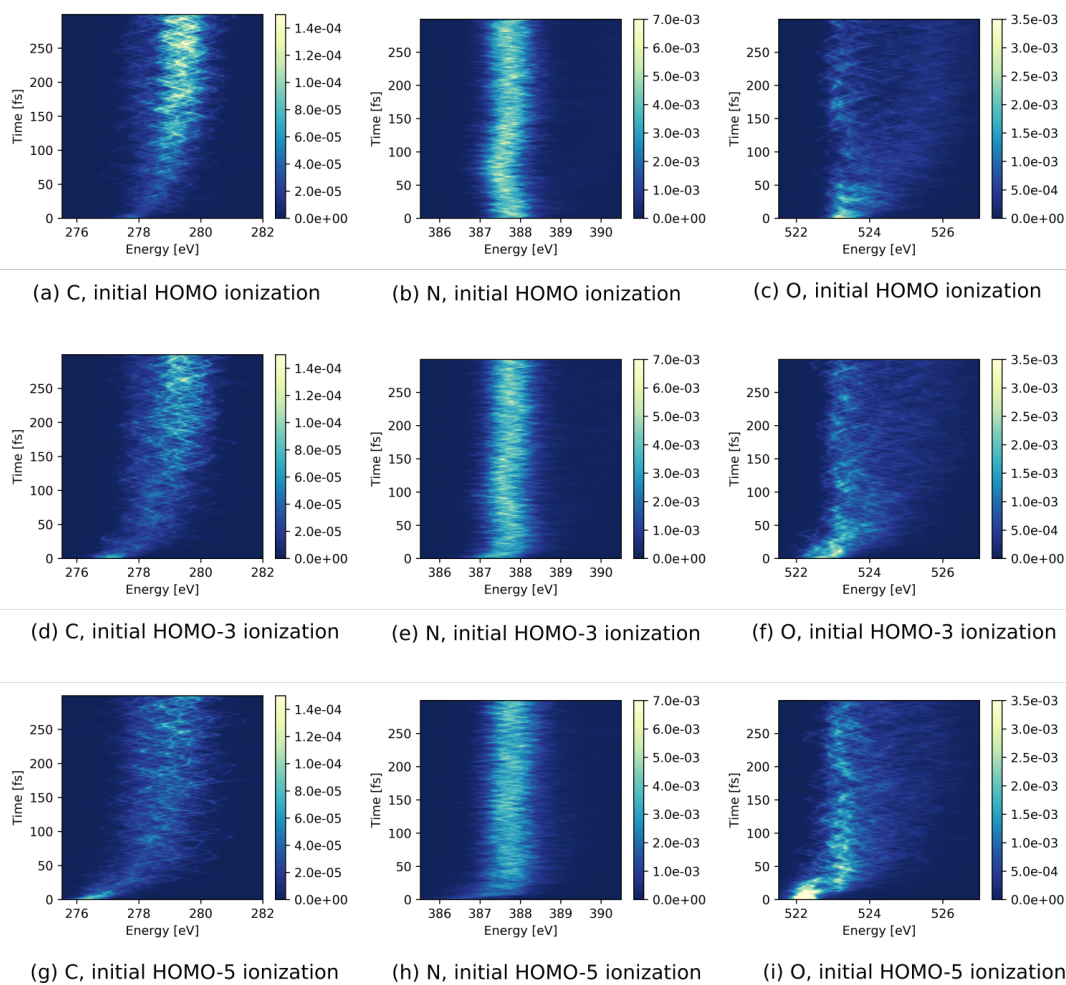


FIGURE 3.7: TRXAS (given by cross sections in a.u.) of urea dimer after initial ionization of (a)-(c) HOMO, (d)-(f) HOMO-3, and (g)-(i) HOMO-5 at the lowest (left) C, (middle) N, and (right) O K -edge absorption resonances. Figure taken from Ref. [44].

to the ground state.

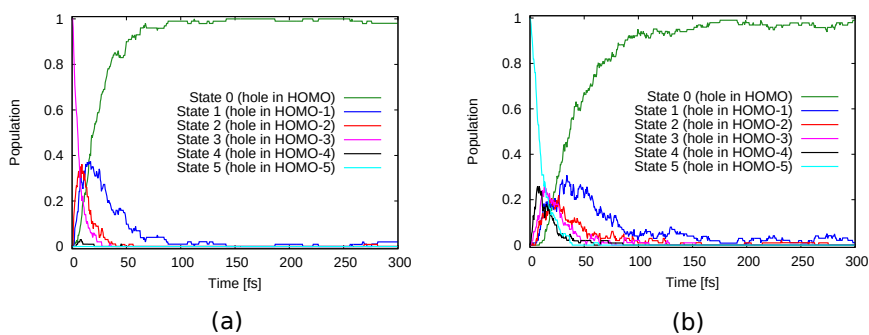


FIGURE 3.8: Electronic state population over time for urea dimer with an initial hole in (a) HOMO-3 and (b) HOMO-5. Figure taken from Ref. [44].

Proton transfer reaction

Upon analyzing the trajectories, I noticed that some of them exhibit a proton transfer reaction, where one of the protons forming a hydrogen bond moves towards the oxygen partner of the other monomer. This reaction has been observed in simulations with all the considered initial ionizations. However, the proton transfer only occurs after relaxation to the HOMO ionized state. To quantify this process, I employed a criterion for proton transfer to be defined by the distance between the oxygen on the acceptor urea and the hydrogen from the donor being less than 1.25\AA . Using this criterion, I found that after ionization of HOMO 70% of the trajectories undergo proton transfer on a timescale of ~ 50 fs (estimated by fitting a sigmoid function to the number of completed proton transfers over time). For initial ionization in HOMO-1, HOMO-2, HOMO-3, HOMO-4, and HOMO-5, timescales of about 65 fs, 80 fs, 80 fs, 90 fs, and 95 fs are observed, and a relative proportion of the trajectories undergoing the transfer of 60%, 53%, 54%, 55%, and 40%, respectively. I attribute this slightly delayed proton transfer to initially deeper bound valence hole states to the additional time that is needed to relax to the ground state where the proton transfer eventually occurs.

To investigate the effect of proton transfer on the spectra, I split the trajectories up into two subsets, one that undergoes proton transfer and another that does not, based on the criterion stated above. The respective spectra for the two subsets are shown in Fig. 3.9. Since the proton transfer occurs in the HOMO hole state, I restricted this analysis to trajectories starting in this hole state. Both subsets show very similar dynamical features for the N K -edge where a transient shift towards lower energies is seen at ~ 75 fs [Figs. 3.9(b) and 3.9(e)]. For absorption resonance at the C and O K -edges, the two subsets exhibit distinct features for delay times larger than 50 fs. The trajectories undergoing proton transfer show a considerable blueshift in energetic position at the C K -edge absorption resonance and a rise in intensity after ~ 100 fs [Fig. 3.9(a)]. In contrast, only a relatively minute rise in intensity [Fig. 3.9(d)] and no energetic shifts can be seen for the subset without proton transfer. Furthermore, for the subset with proton transfer, the absorption intensity at the O K -edge declines at ~ 50 fs [Fig. 3.9(c)], whereas for the subset without proton transfer, no systematic change in intensity can be seen [Fig. 3.9(f)].

The reported changes in absorption intensities can be more clearly seen in the energy-integrated spectra in Fig. 3.10 for the two cases with and without proton transfer. The continuous rise in intensity at the C K -edge well beyond 100 fs and the decrease in signal at the O K -edge up to ~ 50 fs for trajectories with proton transfer are clearly visible in Fig. 3.10(a). Moreover, for the trajectories with proton transfer, one can see that for times less than 50 fs the decrease in the O intensity is mirrored by an increase in the N intensity. For trajectories without proton transfer in Fig. 3.10(b), the intensities exhibit oscillations but no clear increment or decrement. Similar to the monomer case, a strong anti-correlation for the absorption at the O and N K -edges is seen here, suggesting that the time variation can be linked to the same structural dynamics.

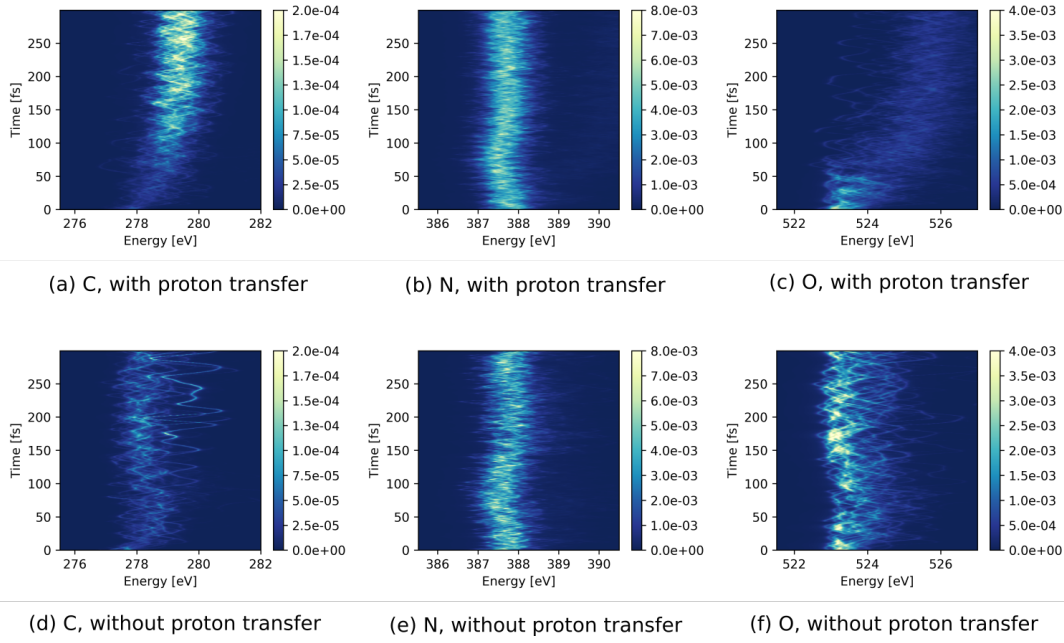


FIGURE 3.9: TRXAS (given by cross sections in a.u.) of urea dimer after initial ionization of HOMO for trajectories (a)-(c) with and (d)-(f) without proton transfer at (left) C, (middle) N, and (right) O K -edge absorption resonances. Figure taken from Ref. [44].

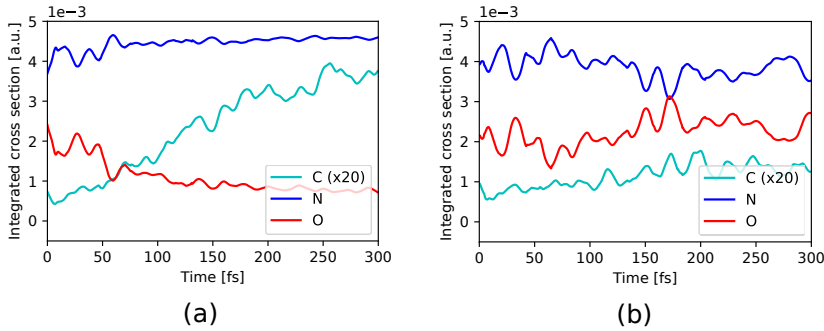


FIGURE 3.10: Energy-integrated spectra of urea dimer from Fig. 3.9 for the C (scaled by 20), N, and O $1s$ pre-edge resonances following initial ionization in HOMO for trajectories (a) with and (b) without proton transfer. Figure taken from Ref. [44].

To understand these intensity variations, Fig. 3.11 shows snapshots at selected times for two representative trajectories, one with proton transfer [Figs. 3.11(a)-3.11(d)] and another without [Figs. 3.11(e)-3.11(h)]. The HOMO orbital containing the electron hole is depicted in each of the snapshots. In both trajectories, the initially delocalized valence hole localizes to one of the two ureas after ~ 30 fs (see Figs. 3.11(a), 3.11(b), 3.11(e), and 3.11(f)). The initial electron hole localization is followed by a cleavage of one hydrogen bond and a contraction of the other hydrogen bond. The upper trajectory exhibits proton transfer leading to a protonated urea cation $(\text{NH}_2)_2\text{COH}^+$ and a deprotonated urea $(\text{NH}_2)(\text{NH})\text{CO}$ [Fig. 3.11(c)]. After the proton transfer, the dimer rearranges and a new hydrogen bond is formed between the

O atoms of $(\text{NH}_2)_2\text{COH}^+$ and $(\text{NH}_2)(\text{NH})\text{CO}$ [Fig. 3.11(d)]. In contrast, in the trajectory without proton transfer, the dimer remains bonded via one remaining hydrogen bond between the N and O atoms [Fig. 3.11(h)]. In the corresponding snapshots in Figs. 3.11(c) and 3.11(d), one can see that the proton transfer comes along with a deformation of the HOMO orbital leading to larger and lower contributions on the N and O atoms, respectively. From the inspection of these example trajectories, I thus hypothesize that the observed decrease in O absorption intensity and the accompanying increase of the N absorption intensity [Fig. 3.10(a)] can be attributed to this reaction.

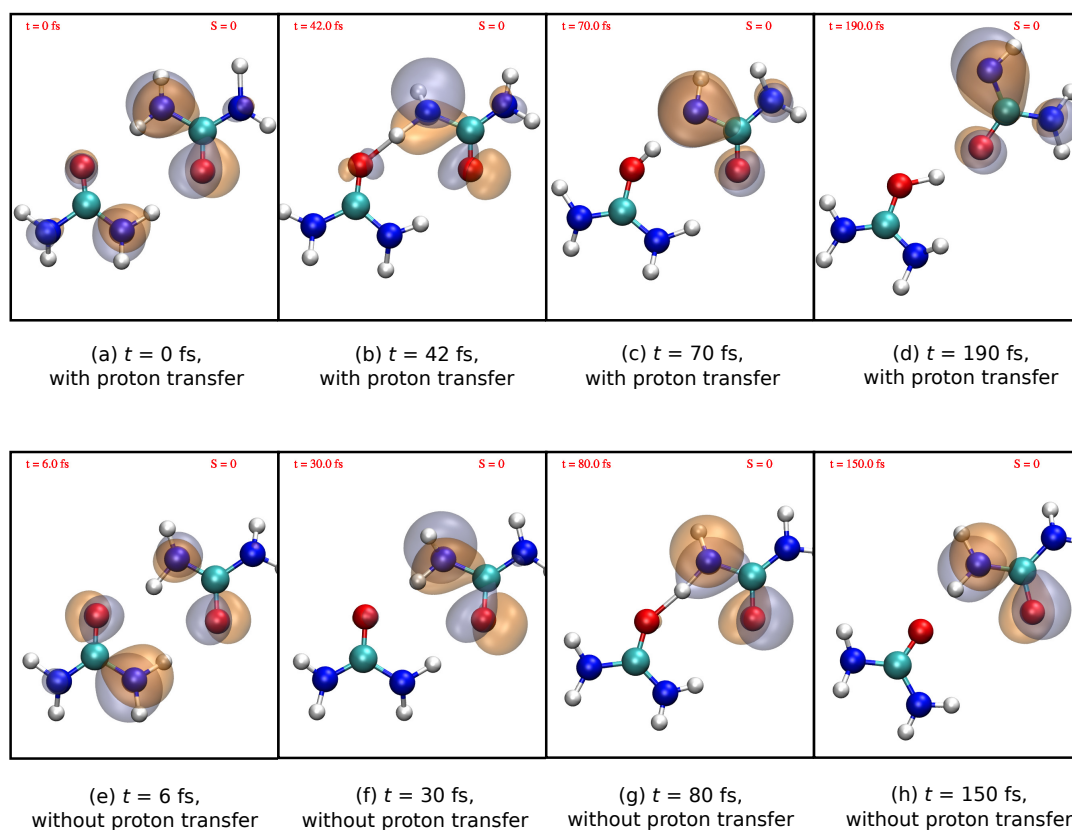


FIGURE 3.11: Hole orbital at selected times for two exemplarily trajectories, (a)-(d) one with and (e)-(h) another without proton transfer following initial HOMO ionization. The hole remains in HOMO (labelled by $S=0$) throughout the simulation. Figure taken from Ref. [44].

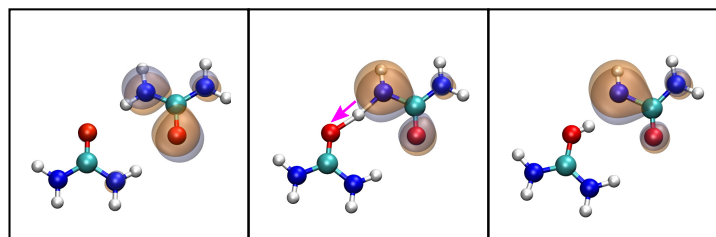
Identifying collective coordinates

To verify the interpretation of the intensity variations with the dynamical motifs of the proton transfer reaction, I performed a PLSR analysis on the geometrical and spectral variations of the dimer, similar to the monomer case. Due to the difficulties in properly selecting a complete set of internal coordinates that also describe intermolecular motion such as the proton transfer, the analysis has been conducted using Cartesian coordinates as opposed to the monomer where internal coordinates have been used. Due to the symmetry, any of the two hydrogen bonds between the two

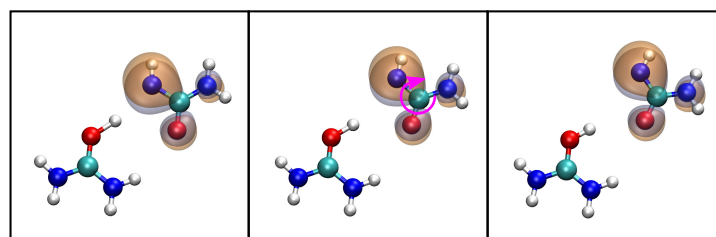
ureas can exhibit proton transfer. To get a clearer picture, I selected trajectories undergoing proton transfer only in one particular direction as input for the PLSR. Because the intensity variation for the N and O signal occurs in the first 100 fs of the simulation, I restricted the corresponding analysis to this time range. The collective coordinate obtained for the N and O signals is shown in Fig. 3.12(a). As one can see, the resulting coordinate describes the proton transfer and comes along with a shift in the HOMO from the O towards the N atoms. This result confirms the interpretation that the decrease in the absorption signal for O and the corresponding increase for N is indeed a signature of the proton transfer. Figure 3.12(c) compares the time evolution of this collective motion with the standardized N and O absorption intensity. As can be seen, considerable variations in the intensity in the first 20 fs cannot be explained with the depicted motion (the coordinate explains 24% of the variation in the N and O peaks combined). This discrepancy indicates that the relation between geometrical changes and absorption intensity cannot fully be explained by a one-dimensional linear model. Nevertheless, on a longer timescale, the depicted coordinate and the absorption intensity follow the same trend.

To also obtain an explanation for the increment in absorption signal at the C *K*-edge seen at ~ 100 fs [Fig. 3.9(a)], I performed a similar PLSR analysis on the absorption intensities (again taking only trajectories with proton transfer in one direction), but now with the full time range up to 300 fs. The collective coordinate found is shown in Fig. 3.12(b) that is able to describe 45% of the variance in the C absorption intensity. The coordinate depicts the rearrangement of the donor urea after the proton transfer, where $(\text{NH}_2)(\text{NH})\text{CO}$ rotates and forms a new hydrogen bond with $(\text{NH}_2)_2\text{COH}^+$ between the two O atoms. As can be seen, the formation of the new hydrogen bond between the two O atoms results in an increase in the population of the HOMO orbital on the C atom (also seen in Figs. 3.11(c) and 3.11(d)) and thus explaining the increase of absorption intensity at the C *K*-edge. The evolution of the identified coordinate together with the averaged variation in the standardized C absorption intensity is shown in Fig. 3.12(d). As can be seen, the evolution of this coordinate follows roughly the intensity rise in the C resonance. However, in the range below 100 fs the rise in intensity does not follow the evolution of the collective coordinate. A further analysis focusing on the time-range up to 100 fs (see Fig. 3.13) reveals that this rise can be associated with a proton transfer motion similar to the one depicted in Fig. 3.12(a).

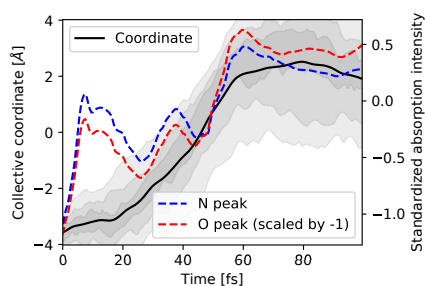
To sum up, I observed that the localization of the electron hole to one of the ureas causes a redistribution of the charge in the dimer and alters the partial charge distribution between the hydrogen bond partners. This leads to a repulsion along one of the hydrogen bonds and to attraction along the other hydrogen bond. After the proton has been transferred to the acceptor molecule, the latter is now positively charged and attracts the partially negative O atom of the now neutral deprotonated urea. This causes the formation of a new hydrogen bond between the O of the donor with the donated proton on the acceptor side. The proton transfer as well as the



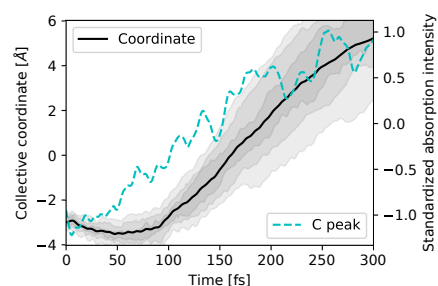
(a) collective coordinate for the N and O signals



(b) collective coordinate for the C signal



(c) N and O peaks, and their associated collective coordinate over time

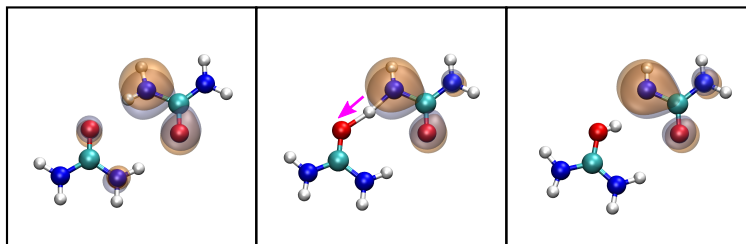


(d) C peak and its associated collective coordinate over time

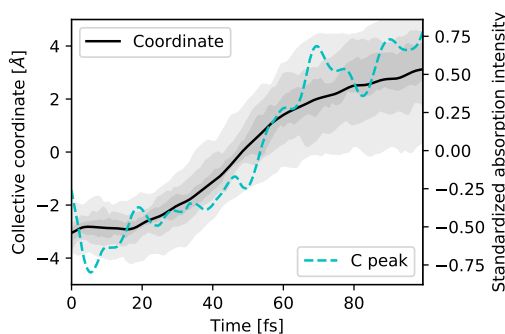
FIGURE 3.12: HOMO along the collective coordinate motion that explains the intensity variations (a) in the N and O peaks, and (b) in the C peak for the dimer. Temporal evolution of the collective coordinate along with the averaged standardized absorption intensity for (c) the N and O peaks, and (d) the C peak. The shaded areas indicate regions between percentiles (37.5% - 67.5%, 25% - 75%, and 12.5% - 87.5%) of the coordinate distribution. Figure taken from Ref. [44].

subsequent rearrangement of the resulting conformer leave distinct fingerprints as intensity variations in the TRXAS.

Regarding the proton transfer, note that an analogous sequence of events was described before in a study of liquid water, where the localization of a valence hole triggered a proton transfer and thus a separation of charge and spin [168]. In this context, an x-ray absorption energy shift for the donor during proton transfer was reported [35], similar to what has been observed here as the transient redshift at ~ 75 fs in the energetic position of the N resonance [Figs. 3.9(b) and 3.9(e)]. To further investigate this transient shift, I performed a similar PLSR analysis as for the N and O absorption intensities, but now for the energetic position of the N absorption resonance using all trajectories, with and without proton transfer, taking the first 100 fs.



(a) collective coordinate for the C signal



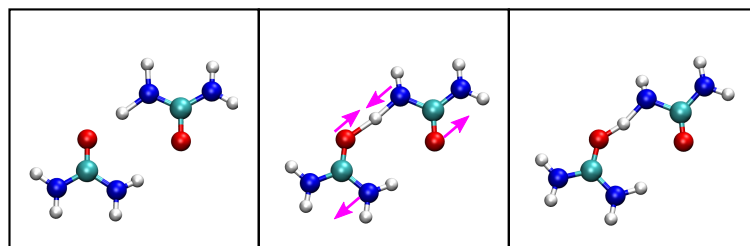
(b) C peak and its associated collective coordinate over time

FIGURE 3.13: (a) HOMO along the collective coordinate motion that explains the intensity variations in the C peak for the first 100 fs of the dimer. (b) Temporal evolution of the collective coordinate along with the averaged standardized absorption intensity for the C peak. The shaded areas indicate regions between percentiles (37.5% - 67.5%, 25% - 75%, and 12.5% - 87.5%) of the coordinate distribution. Figure taken from Ref. [44].

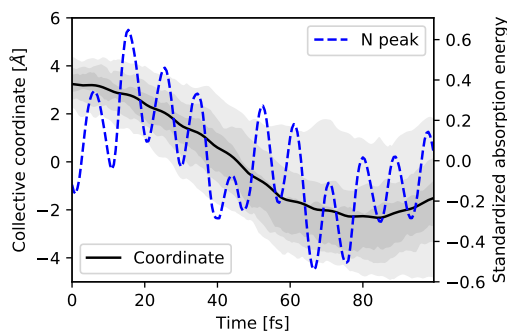
The results confirm that this transient energy shift can be attributed to the motion of attempted proton transfer which all trajectories undergo (see Fig. 3.14). More specifically, this is the breaking of one hydrogen bond and contraction of the other. The analogies to the case with liquid water lead us to speculate that the discussed trends in the TRXAS are transferable to other situations where a proton transfer takes place. Notably, further analysis (not shown) reveals that these attempted proton transfer dynamics can also partially account for the discrepancy in the first 20 fs in Fig. 3.12(c).

3.4 Summary

To summarize, I performed on-the-fly *ab initio* nonadiabatic dynamics upon HOMO and deeper valence ionization of urea and its dimer, and have calculated the TRXAS at the C, N, and O *K*-edges. Nuclear, as well as electronic dynamics, are clearly visible as distinct spectroscopic signatures in the TRXAS. After ionization in deeper valence orbitals, time-dependent blueshifts in the absorption energy are observed, indicating electronic relaxation via nonadiabatic transitions to the electronic ground state of the cation. This occurs on a timescale of a few tens of femtoseconds in both urea and its



(a) collective coordinate for the N absorption energy



(b) N absorption energy and its associated collective coordinate over time

FIGURE 3.14: (a) Collective coordinate motion that explains the absorption energy variations in the N peak. (b) Temporal evolution of the collective coordinate along with the averaged standardized absorption energy for the N peak. The shaded areas indicate regions between percentiles (37.5% - 67.5%, 25% - 75%, and 12.5% - 87.5%) of the coordinate distribution. Figure taken from Ref. [44].

dimer. Creating an initial hole in HOMO for urea leads to some noticeable variations in the intensity of the spectra that I associate with specific molecular vibrations through PLSR analysis. For the urea dimer, a proton transfer reaction occurs between the two ureas following HOMO ionization at around 50 fs for about 70% of the trajectories. This reaction leaves fingerprints in the TRXAS which can be attributed to the proton transfer itself at the N and O K -edges and a subsequent rearrangement of the dimer structure C K -edge, both elucidated through PLSR analysis again.

Chapter 4

Tracing ultrafast proton transfer dynamics in ionized aqueous urea

This chapter is based on the following manuscript with some changes and restructuring to fit the thesis structure:

- Zhong Yin*, Yi-Ping Chang*, Tadas Balčiūnas*, Yashoj Shakya*, Aleksa Djorović, Geoffrey Gaulier, Giuseppe Fazio, Robin Santra, Ludger Inhester, Jean-Pierre Wolf, and Hans Jakob Wörner, "Femtosecond proton transfer in urea solutions probed by X-ray spectroscopy", Nature (2023). <https://doi.org/10.1038/s41586-023-06182-6>

* Equal contribution

In this joint theoretical and experimental work, I performed the theoretical computations (except those shown in Table 4.1) and analysed the simulated data under the supervision of Ludger Inhester and Robin Santra. In particular, I ran neutral MD simulations of aqueous urea solution using the publicly available software GROMACS, and I performed ionized state QM/MM simulations and the XAS spectra calculations using the in-house developed CDTK and XMOLECULE codes, where I extended CDTK to generate TRXAS spectra for any general molecule with MM point charges using absorption cross sections from XMOLECULE. I also conducted the analysis of the data including analysing proton transfer reaction and the geometric structures of urea dimers. Our experimental collaborators Zhong Yin, Yi-Ping Chang, and Tadas Balčiūnas performed the experiments and analysed the experimental data. I contributed to writing the manuscript together with all the other co-authors. Note that this work extends the urea in vacuum simulations from Chapter 3 to deal with ionized aqueous urea solution.

4.1 Introduction

Urea and its photoinduced reactions are a cornerstone in current theories on the origin of life. Its serendipitous synthesis from inorganic compounds by Wöhler in 1828 [152] shattered the long-held dogma that organic molecules could only originate from living matter and initiated the search for the molecular history of life. In their seminal 1959

spark-discharge experiments mimicking the prebiotic conditions on earth, Miller and Urey showed that urea was indeed formed in large quantities from gases present in the primordial atmosphere [169]. Oró and Kimball later demonstrated how urea and the related molecule guanidine can be efficiently synthesized under plausible prebiotic conditions [170]. Combined with its outstanding stability against radiation damage and radiation-induced chemistry [171], it is therefore very likely that urea was available in large quantities at the origin of life on earth.

Moreover, urea has been demonstrated to be a possible nucleoside precursor [172]. When exposed to ionizing radiation, urea forms malonic acid [171], which has been shown to further react with urea to yield several nucleobases [172]. This reactive pathway is favored under high concentrations of urea, which are likely to have existed under prebiotic conditions. Urea forms dimers, held together by hydrogen bonds that are equivalent to those found in Wobble base pairs, responsible for the secondary structure of ribonucleic acid (RNA) and the proper translation of the genetic code. Poly-urea RNA, also referred to as "Wöhler-RNA" [173], is, therefore, itself a promising candidate for understanding the molecular evolution that has led to the commonly accepted RNA world [174]. Extensive experimental evidence underscores the central role that urea may have played in the early molecular evolution [175].

The urea dimer thus offers itself as an intriguing system for understanding the ultrafast chemistry at the origin of life. The absence of a dense atmosphere in prebiotic Earth indicates the presence of intense ionizing radiation, which implies the significance of ionization-induced chemistry [176, 177]. Additionally, the urea dimer is also an excellent model system for studying proton transfer across hydrogen bonds, which is an important source of mutations, in both RNA and DNA [178].

In addition to its potential relevance for the origin of life, urea plays an important role as an osmolyte in living cells [179, 180]. At high concentrations, urea mediates protein denaturation [181–183]. Whether this denaturation effect bases on a urea-mediated change of the water hydrogen-bond structure or on a direct interaction of urea molecules with the protein has been debated for decades (see Refs. [184–186] and references therein). Previous works characterizing aqueous urea solutions indicate that at high concentrations urea molecules partially self-associate and form transient hydrogen-bonded oligomers [187–191].

Given the wide significance of urea, its dimer and photoinduced proton transfer dynamics, this system offers an ideal test bed for the application of femtosecond soft-X-ray-absorption spectroscopy of liquids [28]. The recent development of table-top soft-X-ray spectroscopy [23, 24, 192] has indeed opened new avenues for investigating electronic and structural dynamics in molecular systems with site specificity [27] and ultimate time resolution [29]. This method has so far mainly been applied to gas-phase studies, thus excluding the relaxation pathways arising from coupling to an environment. In the liquid phase intermolecular interactions can be studied as well, including solute-solvent interactions as well as bimolecular interactions [28, 45]. Here, we investigate femtosecond proton transfer in ionized urea dimers. We employ

element-specific soft-X-ray transient-absorption spectroscopy to investigate dynamics in ionized, highly-concentrated urea solutions, relevant to prebiotic conditions on earth.

In addition to following the proton transfer in real-time, we show through direct comparison with quantum mechanics/molecular mechanics (QM/MM) calculations, that the underlying electronic and nuclear dynamics can be distinguished. Specifically, the X-ray absorption strength at the carbon K-edge traces the gradual appearance of a valence hole at the carbon atom with atomic resolution. The transfer of the charged proton, in contrast, is visualized by an energy shift of the X-ray absorption resonance, which occurs on a different time scale. This separation of electronic and structural dynamics is a unique feature of transient XAS that sets it apart from other techniques, such as elastic X-ray or electron diffraction. Our work thereby establishes XAS as a promising method for elucidating the broad class of nonadiabatic ultrafast dynamics in solution-phase chemistry.

4.2 Experimental setup and static spectra

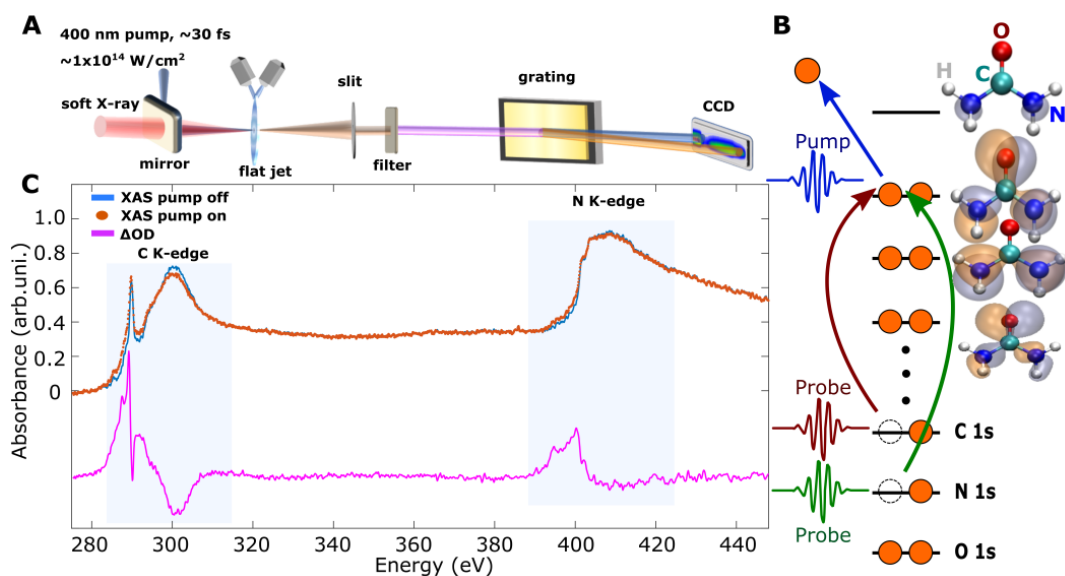


FIGURE 4.1: Overview of the experimental setup and the pumped and unpumped spectra: (A) Schematic depiction of the experimental setup. (B) Schematic molecular-orbital diagram illustrating ionization by a pump pulse, followed by probing the system with an SXR pulse. (C) XAS spectrum of 10M urea solution covering the carbon and nitrogen K-edges with and without pump, and the accumulated Δ OD signal.

Figure taken from Ref. [193].

First, starting with a description of the experimental setup from our collaborators to perform transient X-ray absorption spectroscopy (XAS) measurements on 5 M and 10 M aqueous urea solution, Figure 4.1 illustrates the experimental scheme, where a broadband soft X-ray (SXR) probe pulse covering the carbon and nitrogen K-edges is focused on a sub-micron-thin liquid flat-sheet sample [194]. The SXR pulse is obtained

by high-harmonic generation of a (sub)-two-cycle mid-infrared laser pulse, obtained by filamentation pulse compression [195]. The transmitted light is recorded with a soft-X-ray spectrometer utilizing a variable-line-spacing grating and a charge-coupled-device (CCD) X-ray camera (see Appendix A and Ref. [28] for more details). A 400-nm pulse, with a duration of ~ 30 fs serves as the pump pulse, inducing multi-photon ionization in the liquid sample.

Figure 4.1C shows the measured static X-ray absorption spectrum of a 10 M aqueous urea solution at the carbon and nitrogen K-edge (blue) as well as the time-averaged transient absorption of the ionized sample (orange). The difference spectrum (ΔOD) is shown in magenta. The shaded areas highlight the near-edge X-ray-absorption fine-structure (NEXAFS) region of the spectra around the carbon and nitrogen edges. The carbon K-edge absorption exhibits a strong and narrow pre-edge feature around 290 eV followed by a shoulder and a broader peak around 300 eV corresponding to the $C1s \rightarrow \pi^*$ and $C1s \rightarrow \sigma^*$ transitions of urea, respectively, in agreement with previous studies [45, 196, 197]. At the nitrogen edge, a shoulder is visible at around 400 eV followed by a broad peak of increased absorption. At the carbon edge, the signal of the photoionized sample follows the same trend as the unpumped sample, with intensity differences below and above the edge. At the nitrogen edge, the ΔOD spectrum exhibits an increased absorption below the pre-edge. All pre-edge absorption features originate from allowed transitions into valence vacancies created by the pump pulse. The experimental spectra have been calibrated by aligning the experimental nitrogen pre-edge peak to previous synchrotron data [197].

4.3 Theoretical Computation Details

Now, this section provides details on the simulations performed to match the experimental setup.

4.3.1 Initial MD setup

The dynamics of ionized urea molecules in an aqueous solution were investigated based on molecular dynamics (MD) simulations using the hybrid quantum-mechanics/molecular-mechanics (QM/MM) approach. To sample the possible configuration structures in the liquid phase, I first performed force-field MD calculations for a 10 M and a 5 M aqueous urea solution using Gromacs (version 2018.8) [198] employing the GROMOS 54A7 force field [199]. The urea force field is based on Ref. [200] and the SPC/E water model [201] was employed. The setup is similar to the calculations in Ref. [202]. For the 10 M urea aqueous solution, a cubic box with volume $(3 \text{ nm})^3$ was filled with 146 urea molecules using the insert-molecules routine from Gromacs. The remaining space was then solvated with 439 water molecules. For the 5 M urea aqueous solution, the same box size was used, but 81 urea molecules and 622 water molecules. The MD simulations were performed at a temperature of 300 K and a pressure of 1 bar

using periodic boundary conditions. In particular, I employed the Particle-Mesh-Ewald method ($r_{\text{cutoff}} = 1$ nm, Fourier spacing = 0.12 nm), Parinello-Rahman pressure coupling ($\tau_p = 1$ ps), velocity-rescale temperature coupling ($\tau = 0.1$ ps) [203], and a time-step of 0.5 fs. After 50 ps of NVT-ensemble equilibration, followed by 50 ps of NpT-ensemble equilibration, a 1000 ps production run (NpT-ensemble) was performed. The actual final concentrations were 10.2 M and 5.5 M. For simplicity, the two simulation setups are simply referred to as 10 M and 5 M in the text. If not stated otherwise, all the data is shown for the 10 M calculation.

From different snapshots of the 10 M simulation, I selected 149 clusters containing a hydrogen-bonded urea dimer and 150 clusters containing a urea molecule with a hydrogen-bonded water molecule. These clusters were considered as the QM region in the following simulations, while the rest of the molecules in the simulation box were part of MM and hence treated using classical force fields. For the selection of these clusters, I employed a geometric hydrogen bond criterion (donor-acceptor distance ≤ 3 Å and hydrogen-donor-acceptor angle $\leq 20^\circ$). For each of these QM regions, the QM/MM setup was further equilibrated by a 2 ps QM/MM simulation performed with Gromacs (version 4.5.5) [204] with the same MD parameters as for the initial setup using the ONIOM embedding scheme [116]. In these calculations, the respective QM region was described using restricted Hartree-Fock (HF) employing the 6-31+G(d) [157–159] basis set. The QM calculations were performed using the XMOLECULE package (rev. 3847) [154, 155] with a modification of the gromacs QM-interface code; for the evaluation of electron integrals the libcint library [205] was employed.

4.3.2 Ionized State Simulation

Based on these samples obtained from MD, I performed simulations with an ionized QM region. In particular, an electron was removed either from the highest occupied molecular orbital (HOMO) or the deeper valence HOMO-3 orbital. These simulations were also performed using the ONIOM embedding scheme and the same force fields for water and urea as used for the MM simulations discussed above. The QM/MM simulations were propagated in an NVE-ensemble setup for 1 ps with a time-step of 0.5 fs and no periodic boundary conditions (the QM region was shifted to the center of the simulation box). The calculations were performed using a similar methodology as earlier work from Chapter 3 on urea monomer and dimer in vacuum [44] using Tully’s fewest switching surface-hopping scheme [66] to handle nonadiabatic dynamics. The electronic structure calculations were again performed at the HF level with the 6-31+G(d) basis set using XMOLECULE. Koopmans’ theorem was used to describe the ionized QM region, which has shown to be reasonably accurate and computationally efficient at describing valence ionized states [35, 40, 44].

Molecule	Basis Set	C1s Ionization Potential from		
		Orbital Energy (eV)	Δ SCF (eV)	Difference (eV)
urea	6-31+G(d)	309.90	298.15	11.75
	6-311++G(d,p)	310.04	296.63	13.31
urea + 3 water	6-31+G(d)	310.20	298.27	11.94
	6-311++G(d,p)	310.06	296.60	13.47

TABLE 4.1: Calculated C1s ionization potentials for exemplary conformation from the MD simulations (urea and urea with 3 neighboring water molecules). In the calculation, the remaining environment was embedded via point charges.

4.3.3 Theoretical TRXAS calculation

To compute the time-resolved X-ray absorption spectra (TRXAS), I calculated the absorption cross section for the core to valence hole transition at each time-step and for each ionized state trajectory using Eq. (3.1) as described before in Chapter 3 and Refs. [35, 40, 44]. The quantities in Eq. (3.1) are given in atomic units (at.u.). To take into account the effect of the MM environment in the cross section calculations, the transition dipoles and orbital energies employed in Eq. (3.1) were calculated by incorporating the MM environment via point charges defined in the force field. For the function $\delta(\epsilon_f - \epsilon_i - \omega)$ I used a finite-width line profile given by a Lorentzian function with a width of 0.5 eV to take into account the natural line width of the core-ionized state and the finite detector resolution in the experiment. The calculated absorption spectra were averaged over all ionized state trajectories for each time-step. In addition, I performed a convolution in time with a Gaussian function with a full width at half maximum (FWHM) of 10 fs to account for the finite time resolution in the experiment.

The absorption resonance energetic positions here were calculated by the orbital energy difference $\epsilon_f - \epsilon_i$. Notably, the resulting energies differed by several eVs when compared to realistic values which were mostly because of orbital relaxation effects following core shell ionization not being taken into consideration in the orbital energy differences. Thus, I down-shifted the calculated absorption spectra by 15.7 eV to correct this effect. This shift was estimated from the difference between the calculated orbital binding energies (310.21 eV) and the corrected experimental carbon K-edge ionization potentials (294.51 eV) [206]. The experimental C1s ionization of urea in an aqueous solution was determined before by Ottosson et al. as 294.0 eV. In their measurement they used the $1b_1$ binding energy in liquid water as reference [207] employing a value of 11.16 eV. Recent measurements revealed, however, a somewhat higher value of 11.67 eV for this binding energy [208]. Therefore, the C1s ionization potential was corrected to 294.51 eV.

The shift of 15.7 eV is qualitatively confirmed by Δ SCF calculations that take into account the relaxation effect upon core ionization. For an exemplary structural configuration taken from the MD simulation (urea and urea with 3 neighboring water molecules) Table 4.1 compares computed C1s ionization potentials. As can be seen,

the Δ SCF method yields ionization potentials that are 12–13eV lower. Furthermore, there is a clear trend that a larger basis set (6-311++G(d,p) vs. 6-31+G(d)) and the incorporation of environmental water molecules yields considerably lower ionization potentials.

4.4 Results and Discussion

4.4.1 Urea aggregation

Urea in high concentration aqueous solutions forms clusters linked by hydrogen bonds to other urea. To quantify this, Fig. 4.2 illustrates the aggregation pattern of urea molecules in these solutions. From snapshots of the MD simulation, I calculated the concentration of different urea aggregates linked via hydrogen bonds. The concentration of monomers, dimers, and larger oligomers is shown in Fig. 4.2A for the two considered concentrations, namely 10 M and 5 M. As can be seen, for both urea concentrations the contributions of oligomers decrease with size. This finding is similar to the results obtained in Ref. [191]. Comparing the two urea concentrations, one can see that oligomers larger than dimers are almost negligible at 5 M. Moreover, the dimer concentration is almost twice for 10 M compared to 5 M solution.

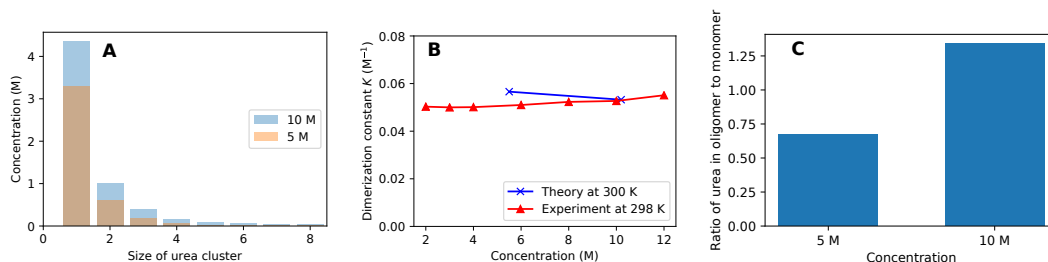


FIGURE 4.2: (A) Concentration of urea monomers/ hydrogen-bonded oligomers as a function of size for 10 M and 5 M aqueous urea solutions. The results are obtained from MD simulations. (B) Dimerization constant K at different concentrations from the calculations (at 300 K) and from Ref. [209] (at 298 K). (C) The ratio of urea oligomers to monomers for 5 M and 10 M aqueous urea solutions. Figure taken from Ref. [193].

To confirm the validity of our MD simulations, I calculated the equilibrium dimerization constant $K = c_d/c_m^2$ where c_d and c_m are the concentration for dimer and monomer, respectively. The calculated values ($K = 0.056 \text{ M}^{-1}$ and $K = 0.053 \text{ M}^{-1}$ for 5 M and 10 M respectively) are compared in Fig. 4.2B with experimental data from Ref. [209] at $T = 298 \text{ K}$. As can be seen, there is a good agreement with these values. The ratio of urea oligomers vs. monomers is shown in Fig. 4.2C. As can be seen, this ratio is roughly twice as large for 10 M compared to 5 M, indicating a drastic difference between the two urea concentrations. Note that the contrast between 10 M

and 5 M is much more pronounced in Fig. 4.2C than in Fig. 4.2A (oligomer concentrations) because an oligomer of size n contains n hydrogen-bonded molecules and thus contributes n times to the oligomer vs. monomer ratio.

4.4.2 Molecular-orbital binding energies and deeper-valence hole state dynamics

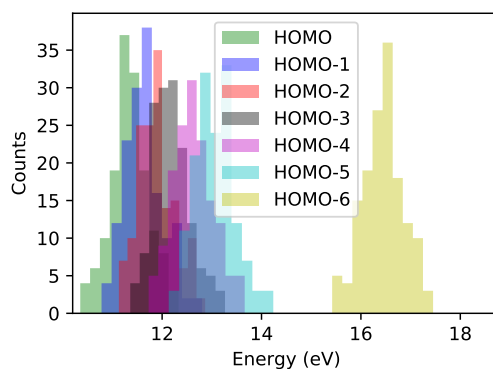


FIGURE 4.3: Histogram of the calculated molecular-orbital binding energies from HOMO to HOMO-6 for the initial QM/MM ensemble of the neutral QM urea dimer in 10 M aqueous solution. Figure taken from Ref. [193].

Now looking in particular at the neutral urea dimer samples in the 10 M aqueous solution, Fig. 4.3 shows the binding-energy distribution for molecular orbitals from HOMO to HOMO-6. This result is similar to the binding-energy distribution for a cyclic dimer in vacuum from Chapter 3 [44] with HOMO to HOMO-5 lying close to each other in energy within about 3 eV. Thanks to the computational efficiency of Koopmans' theorem approach, our computational model can also address valence holes in orbitals that are more strongly bound than HOMO. Due to the proximity in binding energies, ionizing deeper-valence orbitals down to HOMO-5 would lead to rapid decay within the first tens of femtoseconds to the ground state of the ionized system, i.e., into the state with a valence hole in HOMO, which is again similar to the gas phase case from the previous chapter. As a representative example, I show here the hole population dynamics for an initial valence hole in HOMO-3. The corresponding evolution of populations in the different ionized states (valence hole in HOMO-3, HOMO-2, HOMO-1, and HOMO) are shown in Fig. 4.4. As can be seen, the population of the HOMO-3 hole state decays to almost zero in less than 50 fs. The population of the HOMO hole state reaches almost one at about 100 fs.

4.4.3 Transient XAS

Figure 4.5 shows the time-resolved ΔOD spectra of aqueous urea solutions with 10 M and 5 M concentrations, respectively, recorded over a 2 ps time window. At both concentrations, the dominant features are a sharp depletion at 290 eV, corresponding

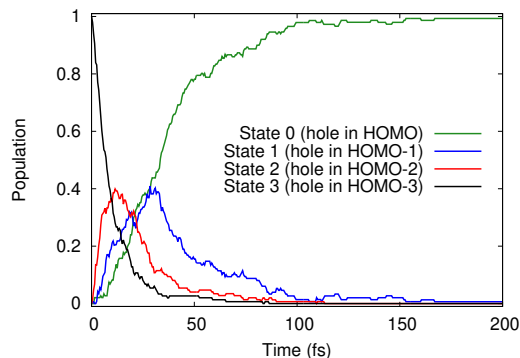


FIGURE 4.4: Population of urea dimer cation states after initial ionization in HOMO-3. The half decay time obtained by an exponential fit to state 3 (hole in HOMO-3) is (6.68 ± 0.02) fs and the half rise time obtained by a sigmoidal fit to state 0 population (hole in HOMO) is (34.19 ± 0.10) fs. Figure taken from Ref. [193].

to the $C\ 1s \rightarrow \pi^*$ transition of the neutral urea molecule, a peak at 289 eV, assigned to the corresponding transition of the urea cation, and a broader, gradually increasing absorption feature extending from 285 eV to 289 eV. This region is assigned to vacancies created by outer-valence ionization of urea molecules.

The main difference between the results obtained with 5M and 10M solutions is the appearance of an additional absorption band on top of the broad absorption feature in the latter data, that appears in the range 286.5-287 eV, gradually shifts to 287.5 eV, and simultaneously increases in intensity. This band is highlighted with an arrow in Fig. 4.5B. A similar feature is not observed at 5M (or lower) concentrations, as seen in panel D. The exclusive observation of this feature at high concentrations suggests that it is a feature associated with urea molecules linked via hydrogen bonds to other urea molecules. The abundance of urea-urea hydrogen bonds was already discussed in Sec. 4.4.1 based on MD simulations (see Fig. 4.2C).

This feature can be identified by comparison with detailed QM/MM calculations in 10M aqueous urea solution. After ionization, we observe that a fraction of the trajectories that employ a urea dimer as the QM region undergo a proton transfer (PT) reaction (about 7% after ionization out of the HOMO, and about 17% after HOMO-3 ionization; see Sec. 4.4.5 below for how this is quantified). This proton transfer reaction resembles the one that was previously studied for a urea dimer in vacuum [44]. We note that the simulations most likely underestimate the amount of proton transfer reactions for reasons discussed below. For the dimer trajectories that undergo proton transfer following HOMO ionization, the resulting time-resolved XAS spectra in the region 286–290 eV (i.e., the region highlighted in panel A–D by dashed lines) are shown in Figs. 4.5E and 4.5F. The calculated spectra clearly display the distinctive time-dependent feature observed in panel B, i.e., both the increase of intensity and the energy shift of the absorption resonance are well reproduced.

We note, however, that the calculated resonance $C1s \rightarrow$ HOMO peak is 3.2 eV lower than the resonance position in the experimental absorption spectra. This offset

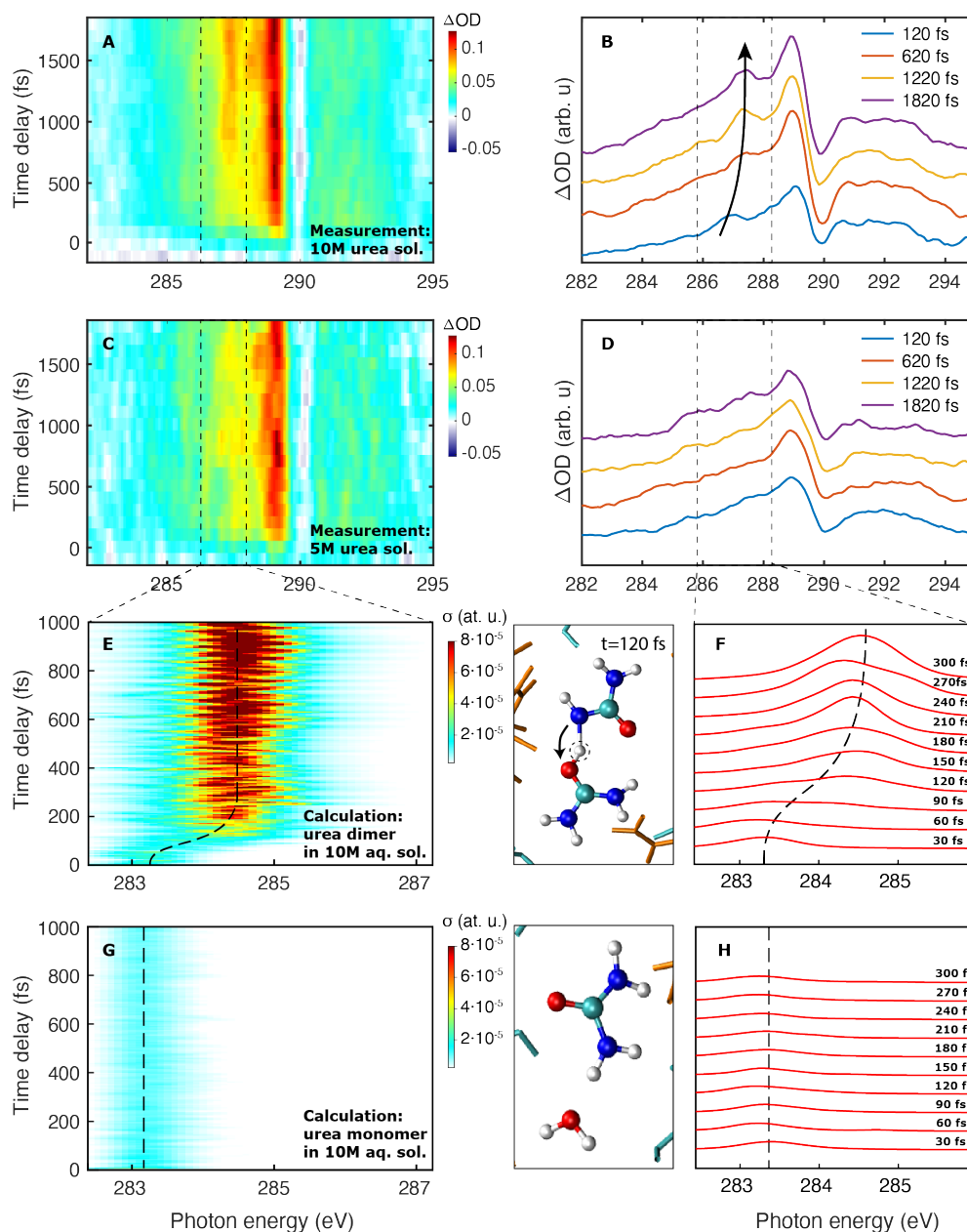


FIGURE 4.5: Overview of experimental and theoretical results. Panels (A-D) represent the transient carbon K-edge XAS results of 10M or 5M urea solutions, whereas panels (E-H) provide a direct comparison with the QM/MM calculations after HOMO ionization (showing cross sections in at.u.). The 10M concentrated urea solution (A, B) reveals the signature of proton transfer in the urea dimer, which is comparable with the QM/MM calculations with urea dimer as QM region following HOMO ionization shown in (E, F). At the lower 5M concentration (C, D) proton transfer is not observed, which is supported by the lack of proton transfer in QM/MM calculations of ionized urea monomers embedded in water (G, H). Figure taken from Ref. [193].

is explained by the large effect of the aqueous environment on the valence ionization potential. By subtracting the known C1s ionization potential of aqueous urea [206] (about 294.51 eV, see correction in Sec. 4.3.3) from the here measured C 1s \rightarrow valence resonance energy of 287.6 eV, we estimate a valence ionization energy of about 6.9 eV, which is about 3.4 eV lower than the ionization energy of urea in the gas phase of about 10.28 eV [164]. This large effect of the aqueous environment is not captured in the calculations and is thus responsible for the too low absorption resonance energy.

The transient XAS from trajectories that consider a monomer with a hydrogen-bonded water molecule in the QM region is shown in Figs. 4.5G and 4.5H. In contrast to the dimer simulations, the XAS from monomer with water simulations only displays a weak and nearly time-independent absorption feature, showing that ionized urea in water remains stable and only undergoes small-amplitude vibrational motion on the simulated time scales. Similarly, the transient XAS of ionized urea dimers that do not undergo proton transfer (shown in Fig. 4.6C) show only minor time-dependent changes. These comparisons therefore clearly establish proton transfer in the ionized urea dimer as the origin of the time-dependent spectral feature highlighted with an arrow in Fig. 4.5B.

For completeness, Fig. 4.6 shows the calculated TRXAS spectra at both carbon and nitrogen K-edges for QM urea dimer with and without PT, and for QM urea monomer with a hydrogen-bonded water molecule in 10 M aqueous urea solutions. Figures 4.6A and 4.6E show the same data as shown in Figs. 4.5E and 4.5G, respectively. For the TRXAS at the nitrogen 1s \rightarrow valence resonance transition (Figs. 4.6B, 4.6D, and 4.6F), no strong temporal changes are observed as opposed to the carbon K-edge. Only for the trajectories with PT (Fig. 4.6B), a small transient redshift at \simeq 100 fs in the resonance position around 398 eV can be seen. Hence, we focus on analysing carbon K-edge spectra in the following sections.

4.4.4 Analysing spectral features

Additional insight into the carbon K-edge spectral feature from Fig. 4.5A can be obtained through a detailed analysis of the experimental and theoretical results. Figure 4.7A shows a magnified version of the experimental XAS spectra in the region of the proton-transfer band from Fig. 4.5A. This data is well represented by three Gaussian bands with time-dependent intensities shown in panel B. The band centered at 286.7 eV decays first, followed by the band centered at 287.3 eV, after which the band centered at 287.6 eV rises.

These observations are well explained by the calculations, which provide additional insights through the contributions from deeper-valence orbital ionization. Whereas such effects have previously been observed in gas-phase attosecond transient-absorption spectroscopy [29], corresponding evidence in the liquid phase has so far remained elusive. Figure 4.7C shows QM/MM calculations of the proton-transfer band of urea dimers following HOMO ionization. This gives rise to the transient spectra previously discussed in the context of Fig. 4.5. The detailed comparison reveals a good

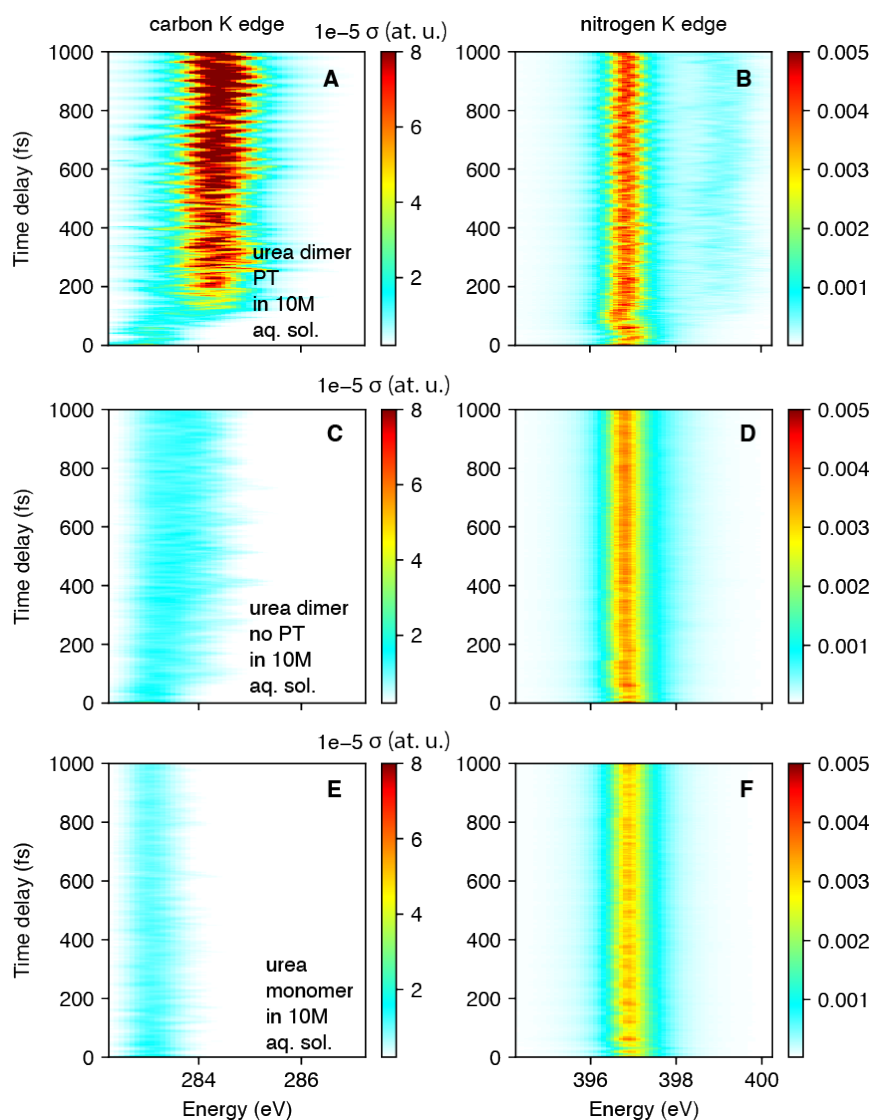


FIGURE 4.6: Calculated TRXAS (given by cross sections in at.u.) for 10M aqueous urea from QM/MM trajectories following HOMO ionization for the $1s \rightarrow$ valence resonance absorption transition from the carbon (A, C, E) and nitrogen (B, D, F) core levels. The panels show the calculated TRXAS from trajectories with PT (A and B) and without PT (C and D). Panel E and F show the TRXAS from calculations that involve a urea molecule and an adjacent water molecule in the QM region. Figure taken from Ref. [193].

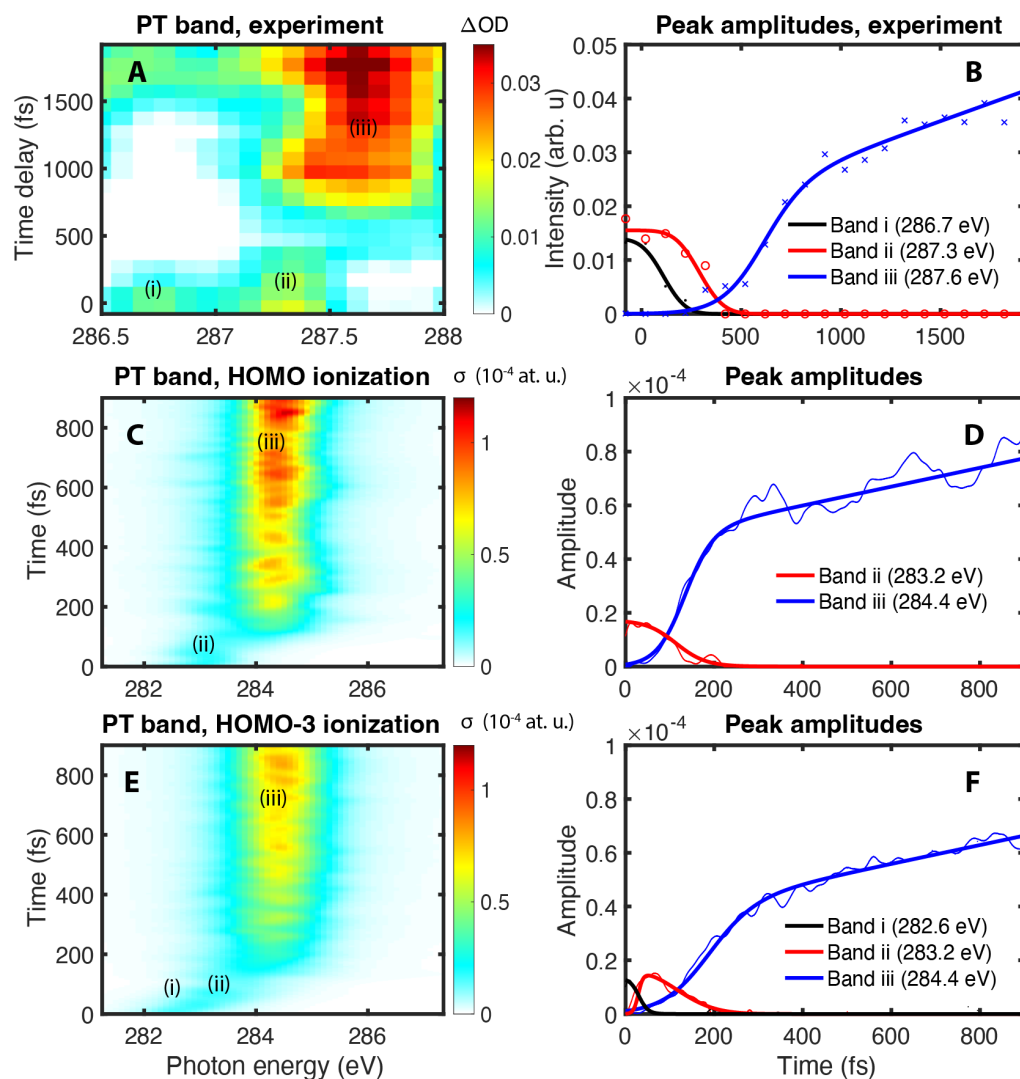


FIGURE 4.7: Detailed analysis of the proton-transfer band in the transient XAS of 10M aqueous urea solution for (A, B) experimental data and (C-F) QM/MM calculations. The proton-transfer bands from (A) the experiment and calculations for ionization of (C) HOMO and (E) HOMO-3 are analyzed by fitting three Gaussians corresponding to the two pre- and one post-proton-transfer band positions as shown inside the figures. Their corresponding amplitude coefficients are shown in (B, D, F). Figure taken from Ref. [193].

agreement with the experimental data overall, but the calculated spectrum consists of a single absorption band at early times, rather than two bands as in the experimental data. This prompted us to study the dynamics following ionization from lower-lying orbitals.

As already seen in Sec. 4.4.2, urea dimer possesses a total of six closely spaced molecular orbitals, all lying within a range of ~ 2 eV (see Fig. 4.3). Ionization from any of these 6 orbitals is followed by nonadiabatic internal conversion to the electronic ground state of the solvated ionized urea dimer (i.e., with a hole in the HOMO) on time scales of $\lesssim 50$ fs (see Fig. 4.4 for an example with HOMO-3 ionization). As a representative case, we show the TRXAS following ionization from HOMO-3 in

Fig. 4.7E for the QM dimer trajectories that undergo proton transfer. Band i in Fig. 4.7F represents the absorption of the electronically excited state of the urea-dimer cation, which decays with a characteristic time of (30 ± 1) fs. These results show that ionization from the lower-lying orbital HOMO-3 gives rise to the appearance of a lower-lying pre-edge absorption feature, which decays more rapidly compared to the case of HOMO ionization, but leads to otherwise very similar signatures of the proton-transfer dynamics. The band i in the measured data in Fig. 4.7B rapidly decays within (110 ± 15) fs, which is consistent with the calculations.

The experimentally measured band ii (panel B) with a decay time of (290 ± 22) fs is thus assigned to the calculated bands ii with decay times of (114 ± 2) fs and (143 ± 1) fs for the HOMO and HOMO-3 ionized dimers, respectively (panels D and F). The (591 ± 128) fs rise time of band iii observed in the experiment is slower than in the calculations: 141 and (180 ± 2) fs, respectively. We attribute this longer rise time in the experimental data to the variation of conformations in the urea solution and to the contribution of diffusion-controlled proton transfers at later times that are not entirely covered by the simulations.

We indeed find that whether a urea dimer undergoes proton transfer within the 1 ps simulation time strongly depends on its initial structure, as discussed below in Sec. 4.4.7. Specifically, we observe a strong propensity for proton transfer if the two urea molecules are linked via the hydrogen atom that lies closest to the oxygen atom (H_{proximal}). This type of hydrogen bond enables the formation of a double-bonded dimer structure that is also the energetically most favorable conformer in vacuum, the so-called cyclic dimer [167]. In contrast, for urea dimers linked via the hydrogen bonds opposite to the oxygen atom (H_{distal}), proton transfer is almost absent. Our results, therefore, suggest that proton transfer occurs after the ionized urea molecule has found a matching proton transfer partner in the proper orientation (again see discussion later in Sec. 4.4.7). Such a diffusion-controlled process is only partially covered in our simulation, since, in order to describe the proton transfer, we have to pick the corresponding partner at the beginning of the simulation and include it in the QM region. By offering only a single urea molecule as a potential proton-transfer partner, namely one that is initially hydrogen-bonded to the ionized molecule in the QM dimer case, we artificially suppress the number of proton transfers, particularly at later times. We, therefore, think that these effects are also largely responsible for the faster rise time in the simulated XAS compared to the experiment.

4.4.5 Quantifying proton transfer

Here, I analyzed the temporal progress of PT by calculating the fraction of simulated trajectories in which PT has occurred as a function of time. For this analysis, I consider a PT to have occurred when the distance between the donor-urea hydrogen and the acceptor-urea oxygen is less than 1.25 \AA . The percentage of PT as a function of time is shown in Fig. 4.8 for different cases. Figures 4.8A and 4.8B show the

PT following HOMO and HOMO-3 ionization, respectively. Following HOMO ionization, about 7% of trajectories undergo PT. Most of the PT dynamics are completed before 400 fs. For HOMO-3 ionization, about 17% undergo PT. The PT dynamics continue up to 1 ps, with most of the PT occurring around 200 fs. The observation that HOMO-3 ionization results in more PT can be explained by the fact that after internal conversion, the ionized molecule has a larger vibrational energy that facilitates overcoming the PT barrier. As discussed earlier, our QM/MM simulations most likely underestimate the actual amount of PT, particularly at longer timescales, as there is only one other urea molecule in the QM region that can accept a proton for the QM dimer situation. In addition, we think that the transfer barriers provided by our electronic structure model are likely overestimated [210].

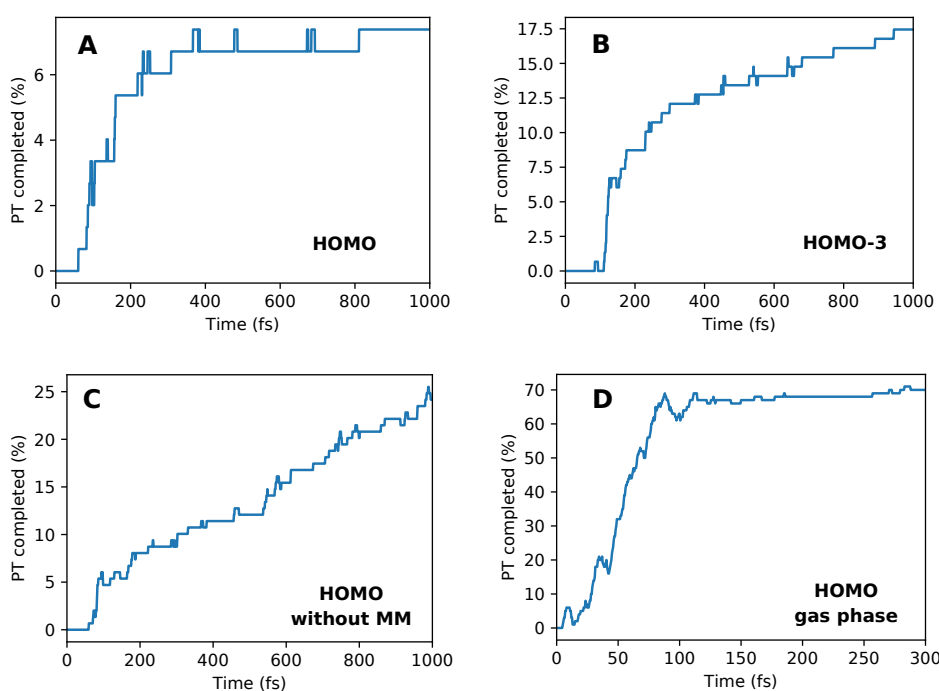


FIGURE 4.8: Percentage of completed PT between urea dimer following ionization of (A) HOMO, (B) HOMO-3 and (C) HOMO without MM environment in a 10 M aqueous urea solution, and (D) HOMO ionization of gas phase cyclic dimer in vacuum from Ref. [44] (please note the different time scale here). Figure taken from Ref. [193].

Figure 4.8C shows an artificial scenario where the MM part has been removed from the ionized dynamics simulation. This setup allows us to highlight the effect of the MM environment. As can be seen from the figure, the ratio of PT trajectories keeps increasing up to 1 ps. About 25% of the trajectories undergo PT within 1 ps. This is clearly different from the results shown in Fig. 4.8A which includes the MM environment. This observation can be explained by the fact that suddenly removing the MM environment leads to a large instantaneous vibrational energy because the QM cluster is suddenly put into a far-from-equilibrium situation. Moreover, without the liquid environment, any vibrational excess energy in the urea molecule after ionization

cannot be dissipated to the surroundings. This excess energy that remains in the ionized system helps to overcome the PT barrier.

For further comparison, in Fig. 4.8D I show gas-phase simulation results from Ref. [44] (so from Chapter 3). These calculations have been performed for a cyclic dimer conformer that results in a much larger amount of PT (about 70%). The PT is also considerably faster due to the ideal initial geometrical arrangements of the two urea molecules, which is also reflected in its spectra as discussed earlier for Figs. 4.10C and 4.10D.

4.4.6 Revealing impact of proton transfer on XAS

Proton transfer is an emblematic case of strongly coupled electronic and nuclear dynamics. It is therefore interesting to explore the specific sensitivities of time-resolved XAS to such dynamics. In the present case, we are particularly interested in understanding whether or how the two types of dynamics can be separated in the experimental observables. For the purpose of illustration, we first discuss the analysis of a selected trajectory and then show that our conclusions also apply to the ensemble average. Figure 4.9 presents snapshots from a QM/MM trajectory of the HOMO-ionized urea dimer undergoing proton transfer. The two urea molecules are initially linked via two hydrogen bonds. Immediately after ionization, the electronic valence hole is localized on one of the urea moieties. After some time, the ionized urea molecule donates one of its protons to the neighboring urea molecule. The characteristic time for the proton transfer is about 150 fs as shown in panel (c). Following the proton transfer, a pronounced rearrangement of the dimer geometry takes place. During this rearrangement, the valence hole, which initially has a vanishing density at the central carbon atom, develops a rapidly increasing amplitude near the carbon atom.

The electronic-structure rearrangement and proton transfer processes are found to manifest themselves in different observables in the corresponding XAS spectra. Figure 4.9E shows the increase of the absorption cross section of the proton-transfer band over time and can directly be assigned to the change in the electronic structure, i.e., the gradual development of electron-hole amplitude on the carbon atom. The proton transfer, in contrast, predominantly leads to a shift of the absorption band to higher photon energies by about 1.2 eV as shown in panel F. An analysis of the time-dependent binding energies of the C1s and singly-occupied molecular orbital (SOMO) of the studied trajectory reveals that the energy shift of the SOMO is the dominant contribution. This shift can directly be assigned to the signature of the charged proton moving away from the donor moiety, leading to a shift of the SOMO towards the vacuum level (i.e., decreasing binding energy).

Interestingly, the increasing absorption cross section (panel E) and the shifting resonance position (panel F) occur on different time scales. A fit of the data with sigmoidal functions yields characteristic half-rise times of (126 ± 3) fs and (80 ± 2) fs, respectively. Whereas the asymptotic absorption strength is only reached after more than 300 fs, the shift of the resonance position is completed in less than 200 fs.

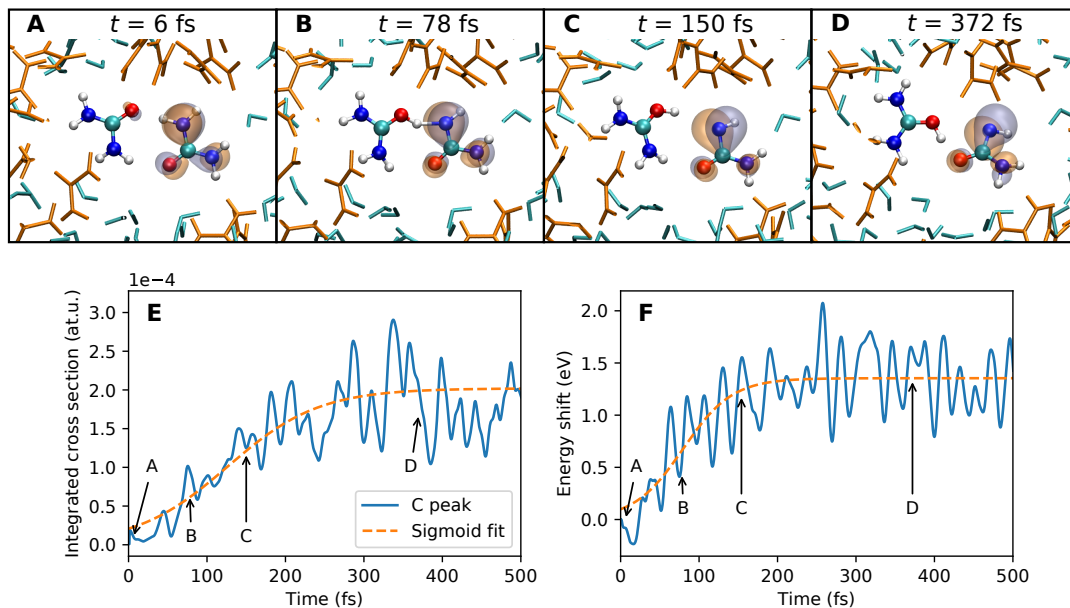


FIGURE 4.9: (A-D) Snapshots from an exemplary QM/MM trajectory displaying proton transfer in the HOMO-ionized urea dimer along with the SOMO (or hole orbital). Time is shown on top. (E) C1s→SOMO absorption cross-section as a function of time; (F) energy shift of the corresponding transition. The blue line shows the calculated position and the dashed orange line is a sigmoidal fit with time constants given in the text. Figure taken from Ref. [193].

Looking at the trajectory snapshots (A-D), these different time scales can be readily explained. The transfer of the (charged) proton is completed in (C), corresponding to a time delay of 150 fs. At this time delay, the SOMO amplitude on the carbon atom has not yet fully developed, which is only the case after more than 300 fs (see panel D).

The conclusions derived from the analysis of a single trajectory in Fig. 4.9 are representative of the ensemble of calculated trajectories that undergo proton transfer. This is illustrated in Figs. 4.10A and 4.10B, which show the corresponding results for the ensemble. The characteristic half-rise times for the increase of the absorption strength and the shift of the resonance position amount to (134 ± 10) fs and (107 ± 7) fs, respectively. Consistent with the example trajectory in Fig. 4.9, these ensemble values indicate that the energetic position of the resonance shifts somewhat earlier than the increase in the absorption cross section. This leads to the conclusion that time-resolved XAS in the water window is, in the present case, capable of separating the dynamical evolution of the electronic structure of solvated molecules from the effects of the moving charge, i.e., the proton transfer. Since the sensitivity of carbon K-edge absorption strength to the time-evolving SOMO amplitude on the carbon atom has previously been observed in Rydberg-valence mixing in dissociating gas-phase CF_4^+ molecules [24], it is likely to be a fairly general feature. Our detailed analysis of the effect of the charged proton being transferred moreover also suggests that the upward shift of the XAS resonance position can also be expected to be a generic feature of

charge-transfer processes in molecular systems. These results, therefore, highlight the considerable potential of water-window time-resolved XAS in disentangling electronic and nuclear dynamics of solvated molecules.

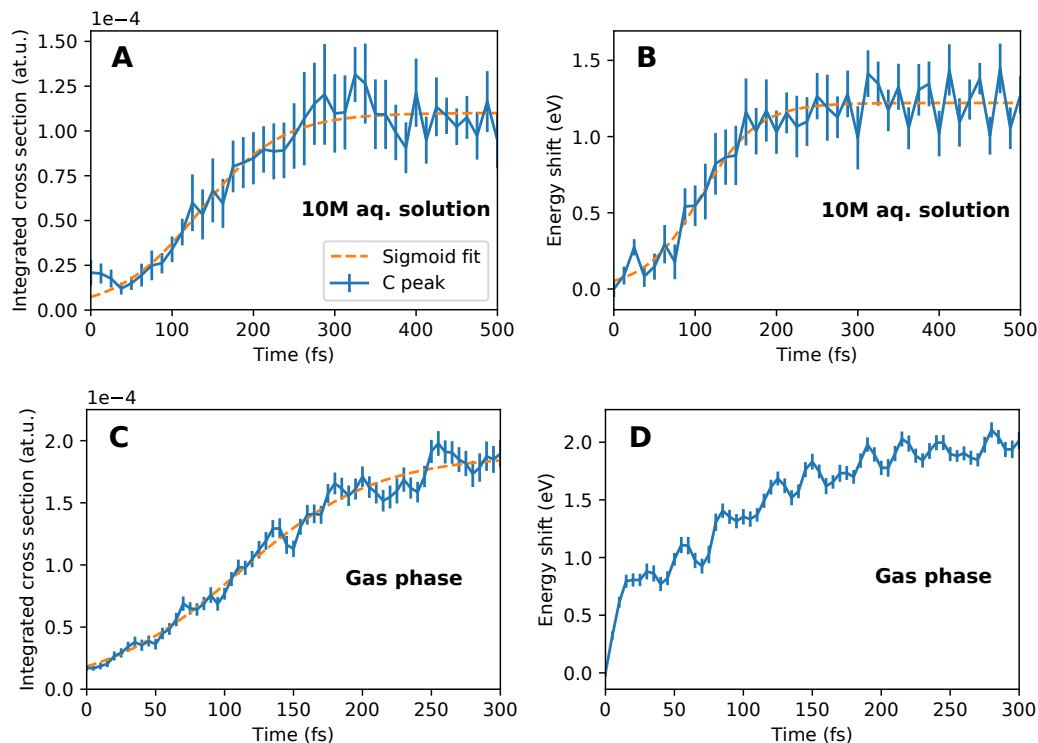


FIGURE 4.10: (A) Ensemble-averaged C1s \rightarrow valence resonance integrated absorption cross-section and (B) energy shift of the corresponding transition as a function of time for the QM dimer trajectories in 10 M solution that undergo PT following HOMO ionization. For comparison, subfigures C and D show the same quantities for a cyclic dimer in vacuum from Ref. [44] (please note the different timescales here). The blue line shows the calculated values and the dashed orange line is a sigmoidal fit with time constants given in the text. Figure taken from Ref. [193].

In Chapter 3, very similar dynamical changes of the TRXAS for urea dimers in vacuum (cyclic conformer) have been observed [44], shown here in Figs. 4.10C and 4.10D for comparison. As can be seen, the changes in the TRXAS in vacuum occur considerably faster. In particular, we obtain half-rise times of (110 ± 3) fs (from sigmoidal fit) and about 60 fs for the cross section and the energy shift, respectively. This comparison indicates that in the aqueous solution at 300 K, the interaction with the environment and the large number of structural conformations considerably slows down the dynamics leading to the slower temporal changes in the TRXAS.

4.4.7 Geometrical-parameter analysis for proton transfer

As briefly mentioned earlier, whether or not PT occurs strongly depends on the initial geometrical structure of the dimer that is selected for the QM region in the simulations. Here, I provide details on this statement. Figure 4.11 shows the fraction of

trajectories where the dimer is initially hydrogen-bonded via the hydrogen atoms next to the oxygen (H_{proximal}) or via the hydrogen atoms opposite to the oxygen (H_{distal}). Figures 4.11B and 4.11C show illustrative examples of the two different dimer structures. As can be seen from the blue bars, both structures occur in similar amounts in aqueous solution. The orange bars indicate the fraction of those trajectories that perform a PT. As can be seen, PT is highly selective for dimer structures that are linked via the H_{proximal} hydrogen atom.

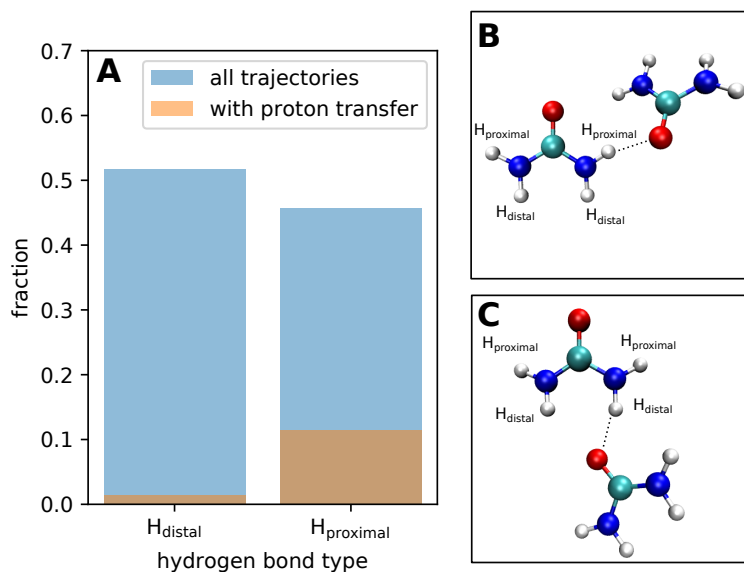


FIGURE 4.11: (A) Fraction of initial QM/MM dimer structures connected via hydrogen bond with a H_{proximal} or a H_{distal} atom (simulations involving HOMO and HOMO-3 ionization combined). The orange bars represent the fraction of trajectories that undergo proton transfer. Exemplary structures for dimers hydrogen bonded through (B) H_{proximal} or (C) H_{distal} are shown on the right-hand side. Figure taken from Ref. [193].

I also investigated some geometrical parameters to further highlight the dependence of PT on the dimer structure. Figure 4.12 shows scatter plots of two geometrical parameters, namely, the oxygen-oxygen distance (d_{O-O}) and the angle between the carbon-oxygen bond vectors (α_{C-O}) of two ureas in the 10 M aqueous urea solution. These geometrical parameters for dimers in the equilibrium solution are shown via blue dots in panels C, D, and E. For ionized QM/MM trajectories that undergo PT, the geometrical parameters at the time of PT following initial ionization of HOMO (panel C) and HOMO-3 (panel D), and HOMO ionization without MM (panel E) are shown on top of this distribution as orange dots. HOMO ionization without MM denotes the artificial setup described earlier: the MM environment is stripped off right before ionization. As can be seen from the distribution of the blue dots (panels C, D, and E), there is a larger variety of initial dimer geometries. The distribution can be roughly clustered into two regions for $d_{O-O} < 4.3 \text{ \AA}$ and $d_{O-O} > 4.3 \text{ \AA}$ as a consequence of the prevalent relative positions and orientations of the two urea molecules [202].

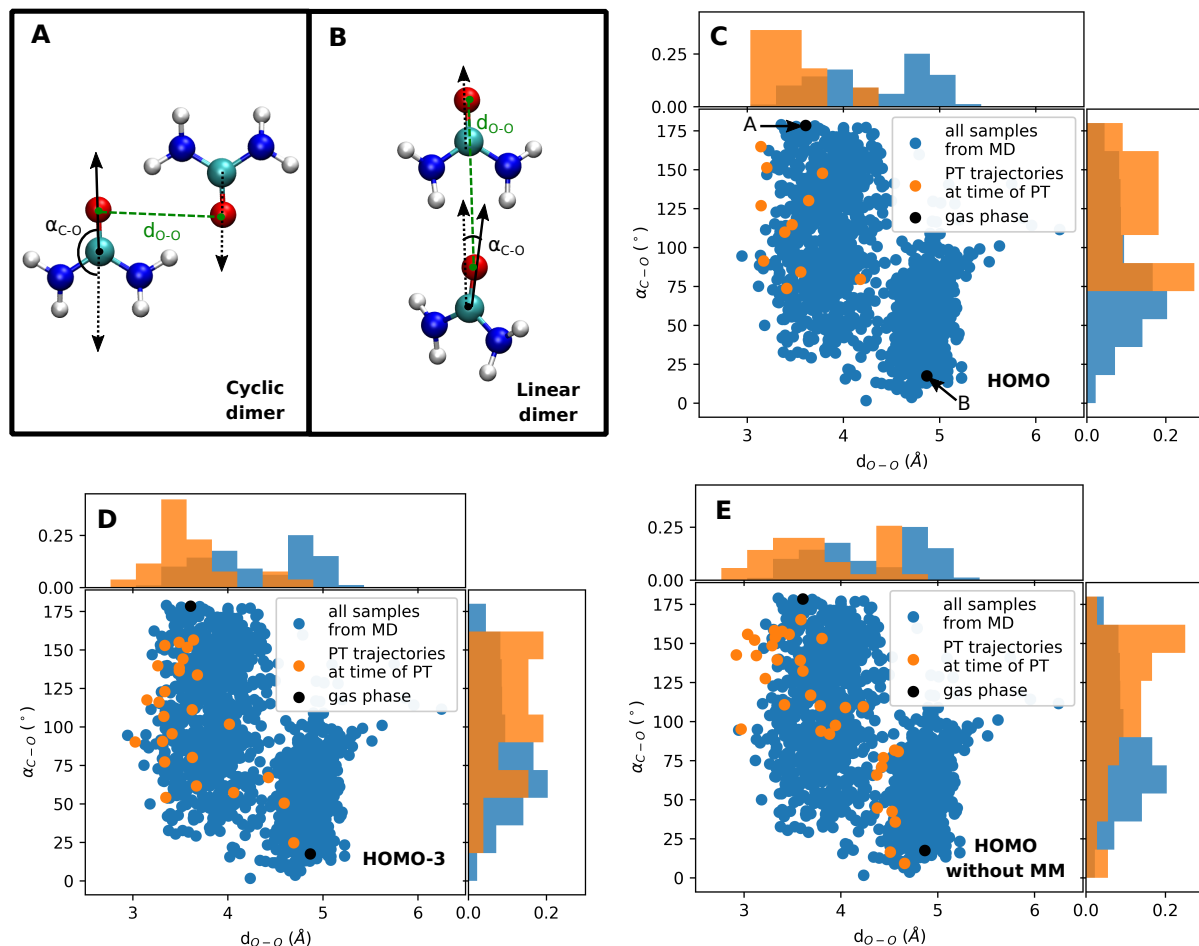


FIGURE 4.12: Geometrical distribution of urea dimers. Panels A and B show two dimer structures in vacuum. Two geometrical parameters are highlighted: the distance between oxygens of the two ureas (d_{O-O}) and the angle between carbon-oxygen bond vectors of the two ureas (α_{C-O}). Panels C, D, and E show the scatter plot between d_{O-O} and α_{C-O} for dimers in the 10M aqueous solution. The blue dots show the distribution for dimers in equilibrium. The black dots show the parameters for the geometrical conformations of the vacuum structures shown in panels A and B. The orange dots indicate the geometrical conformation at the time when PT occurs following ionization in (C) HOMO and (D) HOMO-3, and (E) following ionization in HOMO, where the MM environment has been removed. Panels C, D, and E also show normalized histograms for the two employed geometrical parameters on the top and left side of each scatter plot. Figure taken from Ref. [193].

For comparison, I also show the two vacuum geometries, namely, the cyclic and the linear dimer geometry, as black dots (the geometries are also shown in Figs. 4.12A and 4.12B). These vacuum geometries have been obtained by geometry optimization using HF with the 6-31+G(d) basis set. The cyclic dimer corresponds to a large α_{C-O} and small d_{O-O} , whereas the linear dimer corresponds to a small α_{C-O} but large d_{O-O} . After HOMO ionization (panel C), proton transfer preferentially occurs at geometries with relatively small d_{O-O} and at α_{C-O} larger than 75° . This finding is in accordance with the preference for hydrogen bonds via the H_{proximal} hydrogen atoms shown in Fig. 4.11 as they also fulfill these criteria.

As opposed to the trajectories after HOMO ionization where the described geometrical selectivity is pronounced (Fig. 4.12C), for the trajectories following HOMO-3 ionization, a few PT reactions can also be seen at geometries with $d_{O-O} > 4.3 \text{ \AA}$ and $\alpha_{C-O} < 75^\circ$ (see Fig. 4.12D). For the trajectories where the MM environment has been removed, PT seems to be even less selective with respect to the chosen geometry parameters (Fig. 4.12E). I attribute these results to the fact that the larger vibrational energy produced via HOMO-3 ionization helps to overcome the PT barrier. The even larger vibration energy in the scenario where the MM environment has been suddenly stripped off leads to PT at even more diverse geometrical conformations.

4.5 Summary

We have applied solution-phase water-window XAS to resolve in time the electronic and structural dynamics accompanying femtosecond proton transfer in aqueous urea dimers. Specifically, we found that ionization of urea dimers leads to an ultrafast proton transfer to its neighbour, rapidly followed by a rearrangement of the electron-hole density on the donating moiety. The products of this reaction are a protonated urea molecule and a urea radical, deprived of a hydrogen atom. We have found that our method using XAS selectively identifies the rapidly evolving amplitude of the electron-hole wave function at the carbon atom and maps it into the absorption strength of the carbon pre-edge absorption resonance. The transfer of the charged proton, in contrast, is mapped into a shift of the pre-edge absorption feature towards higher energies. These insights and interpretations of the XAS spectra were obtained from QM/MM simulations of ionized aqueous urea, highlighting the need for theoretical simulations in elucidating dynamics captured in the spectra.

Chapter 5

Capturing electronic decoherence in quantum-classical dynamics

This chapter is based on the following manuscript with some changes and restructuring to fit the thesis structure:

- Yashoj Shakya, Ralph Welsch, Ludger Inhester, and Robin Santra, "Capturing electronic decoherence in quantum-classical dynamics using the ring-polymer-surface-hopping-density-matrix approach", *Physical Review A* **107**, 062810 (2023).
<https://doi.org/10.1103/PhysRevA.107.062810>

I developed the new method discussed in this chapter under the supervision of Ralph Welsch, Ludger Inhester, and Robin Santra. I also implemented this method together with Ralph Welsch in our new code named XPACDT, which is a well-documented and tested generalized nonadiabatic dynamics code with multiple methods implemented. I ran the simulations presented in this chapter, did the data analysis, and wrote the manuscript with guidance from Ludger Inhester and Robin Santra.

5.1 Introduction

With recent advances in laser technology, it has become possible to produce coherent, broadband attosecond pulses [211, 212]. These can be used to create coherent superpositions of electronically excited states in a controlled manner and are a prospective tool to investigate electronic wave-packet dynamics in molecules [213–215]. Employing coherent superpositions of electronic states to steer electron dynamics and eventually control chemical bonds is the central goal of the emerging field of atto-chemistry [216]. Several pioneering experiments demonstrated how attosecond pulses can be used to study and control ultrafast processes in atoms [217], in simple diatomic systems such as H₂, D₂ and O₂ [218–221], and in polyatomic systems [222].

These experiments have triggered theoretical simulations that try to model the involved dynamics. Discarding nuclear motion in some of these models, previous works predicted long-lived electron-hole oscillations [222–228]. More recent studies addressed the intricate interplay of the coupled electronic and nuclear dynamics, and described the coherent electronic oscillations and their rapid suppression due to coupling with

nuclear fluctuations [229–235]. It has been shown that by taking into account a distribution of different geometries due to the finite spatial extent of the nuclear wave function and propagating the electronic wave functions just with static geometries already leads to a considerable dephasing and in the ensemble average eventually to a suppression of electronic coherence [232, 233, 236–238]. Further incorporating nuclear motion has been considered via the Ehrenfest method [232, 233], where an ensemble of classical trajectories is propagated via forces averaged over the respective potential energy surfaces. Accordingly, in the Ehrenfest method, nuclear motion is somewhat restricted since trajectories cannot move apart on separating potential energy surfaces. Consequently, nuclear dynamics and ensuing further dephasing are underestimated. More involved methodologies employ full quantum dynamics simulations based on, e.g., the multi-configuration time-dependent Hartree (MCTDH) method [49, 50]. Full quantum dynamics calculation of both electrons and nuclei is computationally more expensive and typically requires precalculated potential energy surfaces. This limits its applicability with respect to the system size and number of potential energy surfaces considered.

One of the simplest models to overcome the mentioned limitation of the Ehrenfest method while still maintaining an efficient classical description of the nuclear dynamics is Tully’s fewest switches surface hopping (FSSH) [66] and variants of it. Owing to its success in describing nonadiabatic dynamics in a cheap manner based on independent trajectories (see Ref. [78] for a list of applications of FSSH), it has become one of the most popular methods for mixed quantum-classical dynamics. However, it suffers from several drawbacks such as a lack of nuclear quantum effects such as tunneling and zero-point energy, and the so-called overcoherence problem [80–82, 85] that refers to the description of the electronic coherence *within a single trajectory*. Several attempts have been made to fix this overcoherence problem [82–87]. Some of them are done by adding an empirical decoherence term in the dynamics [83, 84] or by resetting the electronic density matrix when the nuclear wavepacket splits on two different electronic surfaces [82, 85]. An interesting method that combines FSSH with ring polymer molecular dynamics (RPMD) [88], named ring polymer surface hopping (RPSH) [90], has shown to include nuclear quantum effects [90] and also claims to capture electronic decoherence [239].

In this chapter, I develop a new approach termed ring polymer surface hopping-density matrix approach (RPSH-DM) to describe coupled electronic and nuclear dynamics. This method combines FSSH with RPMD in a particular way such that electronic decoherence is naturally included via the spatial extent of the ring polymer, which mimics the spread of the wave packet and hence incorporates decoherence effects even in a single trajectory. I demonstrate this capability by applying the method to Tully’s one-dimensional model potential as a stringent test where it outperforms FSSH and previous RPSH methods. In this chapter, I first build up on the theoretical background from Chapter 2 with detailed additional theory needed for this chapter and partly extend them in Sec. 5.2. The details of the new method RPSH-DM are

described in Sec. 5.3. In Sec. 5.4, I apply RPSH-DM to Tully's model potential to test for decoherence and compare results with exact quantum calculations as well as other, previously developed methods. A summary is given in Sec. 5.5.

5.2 Theoretical background

5.2.1 Multistate path integral molecular dynamics

The Hamiltonian described in Eq. (2.69) involves only a single PES under the Born-Oppenheimer approximation. To consider multiple coupled electronic states, one has to go beyond this approximation. Accordingly, the Hamiltonian in a given electronic basis is represented by a matrix of operators acting on the nuclear part, which in the following is denoted by underlining, and reads

$$\hat{\underline{H}} = \underline{T}_N(\hat{\underline{P}}) + \underline{V}(\hat{\underline{R}}), \quad (5.1)$$

where $\hat{\underline{R}}$ and $\hat{\underline{P}}$ are the nuclear position and momentum operators, respectively, and \underline{T}_N and \underline{V} are the nuclear kinetic energy and electronic potential, respectively. Similar to the single-state PIMD case from Sec. 2.4.1, only one nuclear degree of freedom (DOF) is considered for simplicity in this chapter; however, generalization to multiple DOFs can easily be done. Furthermore, atomic units are not used in this chapter to explicitly show the equations derived.

To obtain the multistate partition function Z , a procedure similar to Ref. [139] is followed, except for the addition of bead momenta at the end which is needed for molecular dynamics. Taking a trace here also involves a sum over the electronic states $|j; R\rangle$ to give the following

$$\begin{aligned} Z &= \text{Tr} \left[e^{-\beta \hat{\underline{H}}} \right] \\ &= \int dR^{(1)} \sum_{j^{(1)}} \langle R^{(1)}, j^{(1)} | \left(e^{-\frac{\beta}{n} \hat{\underline{H}}} \right)^n | R^{(1)}, j^{(1)} \rangle \\ &= \int dR^{(1)} \sum_{j^{(1)}} \langle R^{(1)}, j^{(1)} | \prod_{\alpha=1}^n \left(e^{-\beta_n \hat{\underline{H}}} \right) | R^{(1)}, j^{(1)} \rangle, \end{aligned} \quad (5.2)$$

where $|R^{(1)}, j^{(1)}\rangle = |R^{(1)}\rangle \otimes |j^{(1)}; R^{(1)}\rangle$ (the \otimes is omitted later for simplicity of notation). The notation $|j; R\rangle$ indicates that the corresponding electronic basis state depends parametrically on R . Corresponding identity operators which now have nuclear and electronic components, denoted by subscripts N and e respectively

$$\hat{\mathbb{1}} = \hat{\mathbb{1}}_N \otimes \hat{\mathbb{1}}_e = \int dR^{(\alpha)} \sum_{j^{(\alpha)}} |R^{(\alpha)}, j^{(\alpha)}\rangle \langle R^{(\alpha)}, j^{(\alpha)}| \quad (5.3)$$

are inserted $n - 1$ times from $\alpha = 2$ to n giving

$$Z = \int d\{R^{(\alpha)}\} \sum_{\{j^{(\alpha)}\}} \left\langle R^{(1)}, j^{(1)} \left| e^{-\beta_n \hat{H}} \right| R^{(2)}, j^{(2)} \right\rangle \left\langle R^{(2)}, j^{(2)} \left| e^{-\beta_n \hat{H}} \right| R^{(3)}, j^{(3)} \right\rangle \dots \left\langle R^{(n)}, j^{(n)} \left| e^{-\beta_n \hat{H}} \right| R^{(1)}, j^{(1)} \right\rangle, \quad (5.4)$$

where $\sum_{\{j^{(\alpha)}\}} = \sum_{j^{(1)} \dots j^{(n)}}$ and $\int d\{R^{(\alpha)}\} = \int dR^{(1)} \dots \int dR^{(n)}$.

Using symmetric Trotter splitting

$$e^{-\beta_n \hat{H}} = e^{-\beta_n \hat{V}/2} e^{-\beta_n \hat{T}_N} e^{-\beta_n \hat{V}/2} + \mathcal{O}(\beta_n^3), \quad (5.5)$$

and ignoring higher order terms of the order β_n^3 , the partition function is still exact in the limit that $n \rightarrow \infty$. In the adiabatic basis, $\underline{V}(\hat{R}) |R^{(\alpha)}, j^{(\alpha)}\rangle = V_{j^{(\alpha)}}^{ad}(R^{(\alpha)}) |R^{(\alpha)}, j^{(\alpha)}\rangle$ where $V_{j^{(\alpha)}}^{ad}(R^{(\alpha)})$ is the adiabatic energy of state $j^{(\alpha)}$ at position $R^{(\alpha)}$. So for one factor in Eq. (5.4)

$$\left\langle R^{(1)}, j^{(1)} \left| e^{-\beta_n \hat{H}} \right| R^{(2)}, j^{(2)} \right\rangle = e^{-\beta_n V_{j^{(1)}}^{ad}(R^{(1)})/2} e^{-\beta_n V_{j^{(2)}}^{ad}(R^{(2)})/2} \left\langle R^{(1)}, j^{(1)} \left| e^{-\beta_n \hat{T}_N} \right| R^{(2)}, j^{(2)} \right\rangle. \quad (5.6)$$

Now inserting the identity again but in momentum and diabatic $|\vec{d}\rangle$ bases

$$\hat{1} = \int dP^{(\alpha)} \sum_{\vec{d}^{(\alpha)}} |P^{(\alpha)}, \vec{d}^{(\alpha)}\rangle \langle P^{(\alpha)}, \vec{d}^{(\alpha)}|, \quad (5.7)$$

and using $\hat{T}_N |P^{(\alpha)}, \vec{d}^{(\alpha)}\rangle = \frac{(P^{(\alpha)})^2}{2M} |P^{(\alpha)}, \vec{d}^{(\alpha)}\rangle$, we obtain

$$\begin{aligned} & \left\langle R^{(1)}, j^{(1)} \left| e^{-\beta_n \hat{H}} \right| R^{(2)}, j^{(2)} \right\rangle \\ &= \int dP^{(1)} \sum_{\vec{d}^{(1)}} e^{-\beta_n \left(V_{j^{(1)}}^{ad}(R^{(1)}) + V_{j^{(2)}}^{ad}(R^{(2)}) \right) / 2} \left\langle R^{(1)}, j^{(1)} \left| P^{(1)}, \vec{d}^{(1)} \right\rangle \left\langle P^{(1)}, \vec{d}^{(1)} \left| e^{-\beta_n \hat{T}_N} \right| R^{(2)}, j^{(2)} \right\rangle \\ &= \int dP^{(1)} e^{-\beta_n \left(\frac{1}{2} \left(V_{j^{(1)}}^{ad}(R^{(1)}) + V_{j^{(2)}}^{ad}(R^{(2)}) \right) + \frac{1}{2M} (P^{(1)})^2 \right)} \left\langle R^{(1)} \left| P^{(1)} \right\rangle \left\langle P^{(1)} \left| R^{(2)} \right\rangle \sum_{\vec{d}^{(1)}} \left\langle j^{(1)} \left| \vec{d}^{(1)} \right\rangle \left\langle \vec{d}^{(1)} \left| j^{(2)} \right\rangle \right. \\ &= \frac{1}{2\pi\hbar} \int dP^{(1)} e^{-\beta_n \left(\frac{1}{2} \left(V_{j^{(1)}}^{ad}(R^{(1)}) + V_{j^{(2)}}^{ad}(R^{(2)}) \right) + \frac{1}{2M} (P^{(1)})^2 \right)} e^{\frac{i}{\hbar} P^{(1)} (R^{(1)} - R^{(2)})} \left\langle j^{(1)} \left| j^{(2)} \right\rangle. \end{aligned}$$

In the last line $\sum_{\vec{d}^{(1)}} |\vec{d}^{(1)}\rangle \langle \vec{d}^{(1)}| = \hat{1}_e$ is used since there is no other dependence on $\vec{d}^{(1)}$, and also $\langle R|P\rangle = \sqrt{\frac{1}{2\pi\hbar}} e^{iP \cdot R/\hbar}$. The result obtained is quite similar to the single-state PIMD case except for the state-dependent potential and the overlap of electronic states at the end. Hence, following similar steps as for a single state, that is completing the square in the exponential, integrating out the momenta, and inserting Gaussian integrals in bead momenta for a single term in Eq. (5.4), and finally

combining all the terms gives the following

$$Z = \lim_{n \rightarrow \infty} \left(\frac{1}{2\pi\hbar} \right)^n \sum_{\{j^{(\alpha)}\}} \int d\{R^{(\alpha)}\} \int d\{P^{(\alpha)}\} e^{-\beta_n H_n(\{R^{(\alpha)}\}, \{P^{(\alpha)}\}, \{j^{(\alpha)}\})} \times \prod_{\alpha} \langle j^{(\alpha)}; R^{(\alpha)} | j^{(\alpha+1)}; R^{(\alpha+1)} \rangle, \quad (5.8)$$

where $\alpha = n + 1$ means $\alpha = 1$ and the resulting ring polymer Hamiltonian is

$$H_n(\{R^{(\alpha)}\}, \{P^{(\alpha)}\}, \{j^{(\alpha)}\}) = \sum_{\alpha=1}^n \left(\frac{(P^{(\alpha)})^2}{2M} + \frac{1}{2} M \omega_n^2 (R^{(\alpha)} - R^{(\alpha+1)})^2 + V_{j^{(\alpha)}}^{ad}(R^{(\alpha)}) \right) \quad (5.9)$$

which now depends on the respective adiabatic state index $j^{(\alpha)}$ of each bead and where $\omega_n = \frac{1}{\beta_n \hbar}$. This expression is similar to the one derived in Ref. [139], except that the momenta are added back into the equation. Generalization to the diabatic basis has been presented in Ref. [240]. However, in this basis, the expression for the ring-polymer Hamiltonian becomes more cumbersome to handle.

The product of electronic state overlaps in Eq. (5.8) fully captures nonadiabatic effects. However, in this form, they are unsuitable for dynamics calculations. In the following, I explain how surface hopping can be used in the framework of RPMD.

5.2.2 Previous ring polymer surface hopping variants

With the hope of incorporating nuclear quantum effects into multiple electronic state dynamics, previous attempts to combine RPMD and FSSH led to the so-called ring-polymer surface hopping (RPSH) method [90]. Two variants for RPSH were originally proposed: the centroid approximation (CA) and the bead approximation (BA). Both treat the ring polymer effectively as a single unit with one electronic state expansion coefficient. Accordingly, at a given time the whole ring polymer is propagated on the same PES. The electronic coefficients are connected to an adiabatic basis, similar to Eq. (2.10), although the two approaches differ in the specific way the electronic expansion coefficients are propagated. For RPSH-CA, the potential and the nonadiabatic coupling (NAC) are evaluated at the centroid position $\bar{R} = 1/n \sum_{\alpha} R^{(\alpha)}$ yielding

$$\dot{c}_k = -\frac{i}{\hbar} V_k^{ad}(\bar{R}) c_k - \sum_j \dot{\bar{R}} \cdot d_{kj}(\bar{R}) c_j, \quad (5.10)$$

whereas for RPSH-BA, respective bead averaging is employed, i.e.,

$$\dot{c}_k = -\frac{i}{\hbar} \left(\frac{1}{n} \sum_{\alpha=1}^n V_k^{ad}(R^{(\alpha)}) \right) c_k - \sum_j \left(\frac{1}{n} \sum_{\alpha=1}^n \dot{R}^{(\alpha)} \cdot d_{kj}(R^{(\alpha)}) \right) c_j. \quad (5.11)$$

Although these methods have been shown to include nuclear quantum effects in quantum-classical nonadiabatic dynamics [90], the choice of using either one of the two approximations is arbitrary. Additionally, in RPSH-BA the propagation Eq. (5.11)

cannot be derived from a pure electronic Schrödinger equation unlike in FSSH or RPSH-CA.

5.3 New ring polymer surface hopping-density matrix method

Electronic decoherence is captured in FSSH, RPSH-CA, and RPSH-BA through averaging over many trajectories. In particular, when all FSSH trajectories start with the same initial conditions, decoherence in the ensemble only arises due to the stochastic nature of the hops leading to differing trajectories. However, since each trajectory is independent and does not have access to this ensemble decoherence, this leads to the electronic state of each trajectory being essentially fully coherent and thus decoherence effects cannot be incorporated for the evaluation of hopping probabilities. This issue is well known in the literature as the overcoherence problem in FSSH, and a number of techniques have been developed to solve it [81].

I propose here a new approach, termed ring-polymer surface-hopping density matrix (RPSH-DM) approach, to alleviate this issue. By associating with each bead a separate electronic wave packet, I aim to utilize the spread of the ring polymer to naturally incorporate electronic decoherence effects on a single trajectory-level whilst still providing an efficient independent-trajectory method. In addition, nuclear quantum effects should be captured through the use of RPMD. To this end, I employ Eq. (2.10) for each bead labelled by α :

$$\dot{c}_k^{(\alpha)} = -\frac{i}{\hbar} c_k^{(\alpha)} V_k^{ad}(R^{(\alpha)}) - \sum_j \dot{R}^{(\alpha)} \cdot d_{kj}(R^{(\alpha)}) c_j^{(\alpha)}. \quad (5.12)$$

Although each bead is propagated coherently, decoherence is included for the whole ring polymer through the creation of a ring polymer reduced electronic density matrix $\underline{\rho}$ by averaging over the individual beads. Owing to the spatial spread of the ring polymer, the pure-state electronic density matrix for each bead can have different phase properties and this would cause decoherence when averaging over them. Special care has to be taken here for the averaging since each individual electronic coefficient refers to the adiabatic basis that parametrically depends on the individual bead position. Hence, the electronic density matrix for each bead has to be transformed into a common basis using a position-dependent unitary transformation matrix. A natural choice for the ring polymer is to transform to the common adiabatic basis at the centroid position. Accordingly, I calculate the ring polymer reduced electronic density matrix as

$$\underline{\rho} = \frac{1}{n} \sum_{\alpha=1}^n \tilde{\underline{\rho}}^{(\alpha)}, \quad (5.13)$$

where

$$\tilde{\underline{\rho}}^{(\alpha)} = \underline{U}^{(\alpha)} \underline{\rho}^{(\alpha)} \underline{U}^{(\alpha)\dagger}, \quad (5.14)$$

with $\rho_{kj}^{(\alpha)} = c_k^{(\alpha)} c_j^{*(\alpha)}$ as the density matrix element for each individual bead and $U_{kj}^{(\alpha)} = \langle k; \bar{R} | j; R^{(\alpha)} \rangle$ denoting a transformation matrix element to change to the centroid adiabatic basis.

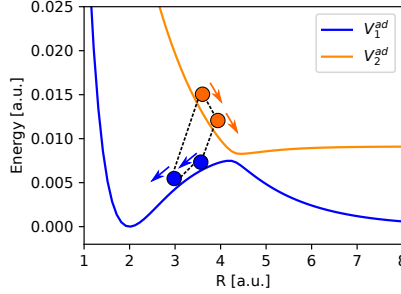


FIGURE 5.1: Schematic of a ring polymer on two PESs, where each bead is propagated on a different PES. Since the beads of the ring polymer interact via harmonic potentials (shown by harmonic springs as dashed lines between the beads), the ring polymer is trapped close to the intersection of the PES since the forces (shown as arrows) effectively cancel each other out. Figure taken from Ref. [241]. ©2023 American Physical Society.

Following the logic of FSSH, it remains to specify on which PES each bead is propagated. Although allowing each bead to be on different surfaces has been considered in the context of equilibrium situations [139, 240], I refrain from this logic because it might lead to skewed dynamics. This is exemplified in Fig. 5.1, where some beads are on the upper and some on the lower PES. Due to the springs connecting the different beads, the ring polymer cannot split up and is therefore forced to stay close to the coupling region until all beads are on the same surface. I, therefore, propagate all beads on a common PES and during hopping, all of the beads change to the same other PES. Following a strategy similar to single-state RPMD, the Hamiltonian from Eq. (5.9) derived in Sec. 5.2.1 for the multiple state case is used to propagate the ring polymer.

5.3.1 Hopping probability

I now derive a hopping criterion for the new method RPSH-DM. To that end, using the product rule, the time derivative of $\underline{\rho}$ from Eq. (5.13) is given by

$$\dot{\underline{\rho}} = \frac{1}{n} \sum_{\alpha=1}^n \left[\dot{\underline{U}}^{(\alpha)} \underline{\rho}^{(\alpha)} \underline{U}^{(\alpha)\dagger} + \underline{U}^{(\alpha)} \dot{\underline{\rho}}^{(\alpha)} \underline{U}^{(\alpha)\dagger} + \underline{U}^{(\alpha)} \underline{\rho}^{(\alpha)} \dot{\underline{U}}^{(\alpha)\dagger} \right]. \quad (5.15)$$

For each bead density matrix $\underline{\rho}^{(\alpha)}$, since the coefficients are propagated using Eq. (5.12), we get

$$\begin{aligned}\dot{\rho}_{kj}^{(\alpha)} &= \dot{c}_k^{(\alpha)} c_j^{*(\alpha)} + c_k^{(\alpha)} \dot{c}_j^{*(\alpha)} \\ &= -\frac{i}{\hbar} c_k^{(\alpha)} c_j^{*(\alpha)} V_k^{ad}(R^{(\alpha)}) - \sum_l \dot{R}^{(\alpha)} \cdot d_{kl}(R^{(\alpha)}) c_l^{(\alpha)} c_j^{*(\alpha)} \\ &\quad + \frac{i}{\hbar} c_k^{(\alpha)} c_j^{*(\alpha)} V_j^{ad}(R^{(\alpha)}) + \sum_l \dot{R}^{(\alpha)} \cdot d_{lj}(R^{(\alpha)}) c_k^{(\alpha)} c_l^{*(\alpha)}.\end{aligned}$$

In matrix form, this can be compactly written as

$$\dot{\underline{\rho}}^{(\alpha)} = -\frac{i}{\hbar} \left[\underline{H}_{\text{eff}}(R^{(\alpha)}), \underline{\rho}^{(\alpha)} \right], \quad (5.16)$$

where I define

$$\underline{H}_{\text{eff}}(R^{(\alpha)}) = \sum_{k,j} \left(V_k^{ad}(R^{(\alpha)}) \delta_{kj} - i\hbar \dot{R}^{(\alpha)} \cdot d_{kj}(R^{(\alpha)}) \right) |k^{(\alpha)}\rangle \langle j^{(\alpha)}| \quad (5.17)$$

as an effective Hamiltonian for a particular bead.

After inserting some identity operators in Eq. (5.15), and using $\underline{1} = \underline{U}^{(\alpha)} \underline{U}^{(\alpha)\dagger}$ and $\underline{\dot{U}}^{(\alpha)} \underline{U}^{(\alpha)\dagger} = -\underline{U}^{(\alpha)} \underline{\dot{U}}^{(\alpha)\dagger}$, leads to

$$\begin{aligned}\dot{\underline{\rho}} &= \frac{1}{n} \sum_{\alpha=1}^n \left(\underline{\dot{U}}^{(\alpha)} \underline{U}^{(\alpha)\dagger} \underline{U}^{(\alpha)} \underline{\rho}^{(\alpha)} \underline{U}^{(\alpha)\dagger} + \underline{U}^{(\alpha)} \dot{\underline{\rho}}^{(\alpha)} \underline{U}^{(\alpha)\dagger} + \underline{U}^{(\alpha)} \underline{\rho}^{(\alpha)} \underline{U}^{(\alpha)\dagger} \underline{U}^{(\alpha)} \underline{\dot{U}}^{(\alpha)\dagger} \right) \\ &= \frac{1}{n} \sum_{\alpha=1}^n \left(-\underline{U}^{(\alpha)} \underline{\dot{U}}^{(\alpha)\dagger} \underline{U}^{(\alpha)} \underline{\rho}^{(\alpha)} \underline{U}^{(\alpha)\dagger} - \frac{i}{\hbar} \underline{U}^{(\alpha)} \underline{H}_{\text{eff}}(R^{(\alpha)}) \underline{U}^{(\alpha)\dagger} \underline{U}^{(\alpha)} \underline{\rho}^{(\alpha)} \underline{U}^{(\alpha)\dagger} \right. \\ &\quad \left. + \frac{i}{\hbar} \underline{U}^{(\alpha)} \underline{\rho}^{(\alpha)} \underline{U}^{(\alpha)\dagger} \underline{U}^{(\alpha)} \underline{H}_{\text{eff}}(R^{(\alpha)}) \underline{U}^{(\alpha)\dagger} + \underline{U}^{(\alpha)} \underline{\rho}^{(\alpha)} \underline{U}^{(\alpha)\dagger} \underline{U}^{(\alpha)} \underline{\dot{U}}^{(\alpha)\dagger} \right).\end{aligned}$$

Now defining a rotated basis Hamiltonian

$$\tilde{H}^{(\alpha)} = \underline{U}^{(\alpha)} \underline{H}_{\text{eff}}(R^{(\alpha)}) \underline{U}^{(\alpha)\dagger} - i\hbar \underline{U}^{(\alpha)} \underline{\dot{U}}^{(\alpha)\dagger} \quad (5.18)$$

and using Eq. (5.14) gives

$$\dot{\underline{\rho}} = -\frac{i}{n\hbar} \sum_{\alpha=1}^n \left[\tilde{H}^{(\alpha)}, \tilde{\underline{\rho}}^{(\alpha)} \right]. \quad (5.19)$$

Accordingly, the rate of population change for state k is given by

$$\dot{\rho}_{kk} = -\frac{2}{n\hbar} \sum_{\alpha=1}^n \sum_{l \neq k} \text{Im} \left(\tilde{\rho}_{kl}^{(\alpha)} \tilde{H}_{lk}^{(\alpha)} \right). \quad (5.20)$$

Similar to the FSSH method, the hopping criterion for RPSH-DM is chosen according to the probability to hop from state k to j in a time step Δ , i.e.,

$$P_{kj} = \frac{\int_t^{t+\Delta} b_{jk}(t') dt'}{\rho_{kk}(t)}, \quad (5.21)$$

where

$$b_{jk} = \frac{2}{n\hbar} \sum_{\alpha=1}^n \text{Im} \left(\tilde{\rho}_{kj}^{(\alpha)} \tilde{H}_{jk}^{(\alpha)} \right). \quad (5.22)$$

Note that in the limit of a single bead, the usual FSSH hopping probability is recovered. If this probability is larger than a uniform random number ranging between 0 and 1, a particular hop $k \rightarrow j$ takes place, provided that the ring polymer has sufficient energy for it.

5.3.2 Momentum rescaling

In the case of a surface hop, I employ a similar momentum rescaling strategy as in FSSH. The bead momenta are rescaled along the NAC with rescaling parameter γ_{kj} when hopping from state k to j as follows:

$$P_f^{(\alpha)} = P_{in}^{(\alpha)} - \gamma_{kj} d_{kj}(R^{(\alpha)}), \quad (5.23)$$

where $P_{in}^{(\alpha)}$ and $P_f^{(\alpha)}$ is the momentum of bead α before and after the hop, respectively. Requiring conservation of the ring polymer Hamiltonian value [Eq. (5.9)], the following equation is obtained for γ_{kj}

$$\gamma_{kj} = \frac{B_{kj} \pm \sqrt{B_{kj}^2 + 4A_{kj} \cdot C_{kj}}}{2A_{kj}}, \quad (5.24)$$

where

$$\begin{aligned} A_{kj} &= \frac{1}{2M} \sum_{\alpha} \left(d_{kj}(R^{(\alpha)}) \right)^2, \\ B_{kj} &= \frac{1}{M} \sum_{\alpha} P_{in}^{(\alpha)} \cdot d_{kj}(R^{(\alpha)}), \\ C_{kj} &= \sum_{\alpha} \left(V_k^{ad}(R^{(\alpha)}) - V_j^{ad}(R^{(\alpha)}) \right), \end{aligned}$$

and the sign in Eq. (5.24) is chosen such that the smallest change in momenta is obtained. In case

$$B_{kj}^2 + 4A_{kj} \cdot C_{kj} < 0, \quad (5.25)$$

the hop is rejected since this implies that the ring polymer does not have sufficient energy for the hop.

An alternative rescaling can be done by requiring conservation of centroid energy [239]. However, bead rescaling chosen here is more consistent since it conserves

the propagating Hamiltonian value which is the ring polymer Hamiltonian. Hence, bead rescaling is used throughout in this work.

5.4 Application to Tully’s model potential

The two-state one-dimensional model potentials introduced by Tully [66] have become a standard scenario for testing quantum-classical methods. This is especially the case for Tully’s model C, that is the extended-coupling-with-reflection-model, as it provides a stringent test requiring decoherence in the reduced electronic subsystem dynamics and thus serves as a good verification for the effectiveness of FSSH variants incorporating electronic decoherence effects. Hence, Tully’s model C is also the choice here to test the new RPSH-DM method. In the underlying diabatic basis, the potential as a function of the single nuclear coordinate R is

$$\begin{aligned} V_{11} &= A \\ V_{22} &= -A \\ V_{12} &= B \exp(CR), \text{ if } R < 0 \\ V_{12} &= B [2 - \exp(-CR)], \text{ if } R > 0, \end{aligned} \quad (5.26)$$

where $A = 0.0006$, $B = 0.1$, and $C = 0.9$. Figure 5.2 shows the potential and coupling matrix elements in the adiabatic and diabatic bases.

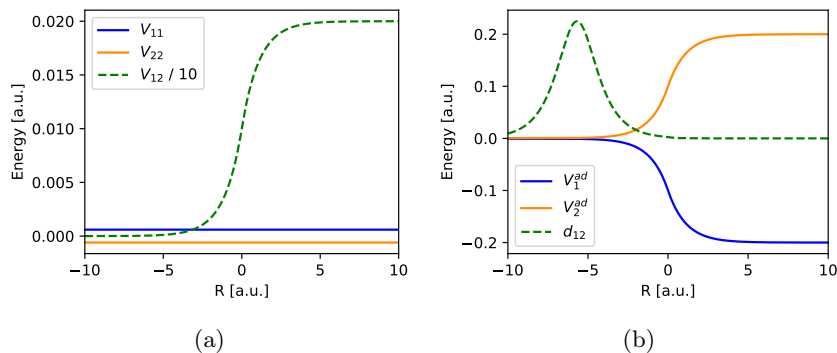


FIGURE 5.2: Tully’s model C potential: extended-coupling-with-reflection in (a) diabatic and (b) adiabatic basis. Solid lines are diagonal potential terms and dashed lines are the off-diagonal potential (a) or the NAC (b), respectively. Figure taken from Ref. [241]. ©2023 American Physical Society.

5.4.1 Simulation details and parameters

I propagated trajectories for this model using FSSH, RPSH-CA, and RPSH-DM, and compare the results obtained to full quantum dynamics calculations using the Heidelberg MCTDH package, version 84 [49, 50, 242]. For all simulations, I used a mass of $M = 2000$ a.u. The full quantum dynamics calculations were initiated at

$t = 0$ fs with a Gaussian wave packet

$$\psi(R, 0) = \left(\frac{2}{\pi\sigma^2} \right)^{1/4} \exp(iP_o(R - R_o)/\hbar) \exp(-(R - R_o)^2/\sigma^2), \quad (5.27)$$

where $R_o = -15$ a.u. and $\sigma = 2$ a.u. (the same parameters have been used before in Ref. [239]). A momentum kick of $P_o = 20$ a.u. was chosen.

For FSSH and the two RPSH methods, 5000 trajectories were used. In FSSH, the trajectories were initialized at position $R = R_o$ and a fixed momentum of P_o . For the RPSH methods, 64 beads were employed and their initial positions and momenta were sampled with path integral molecular dynamics (PIMD) simulations using a harmonic potential $V(R) = \frac{1}{2}M\omega^2(R - R_o)^2$ with $\omega = \frac{2\hbar}{M\sigma^2}$. The centroid was fixed at $R = R_o$. After this sampling, an initial momentum kick of P_o was added to each bead as was done before in similar non-equilibrium RPMD contexts [135–138]. This way the sampled ring polymers cover the phase space distribution

$$W(R, P) = \frac{1}{\pi\hbar} \exp\left(-\frac{(P - P_o)^2}{2(\hbar/\sigma)^2 \coth(\beta\hbar\omega/2)} - \frac{2(R - R_o)^2}{\sigma^2 \coth(\beta\hbar\omega/2)}\right), \quad (5.28)$$

which converges in the low-temperature limit ($\beta \rightarrow \infty$) to the Wigner distribution of the wave packet in Eq. (5.27). For the simulations, $\beta = 10520$ a.u. (corresponding to a temperature of about 30 K) was chosen if not stated otherwise. The same value for β was used for the initial PIMD preparation and the propagation of the ring polymers, as is common in non-equilibrium RPMD [135]. Note that the way the ring polymer is initialized is different than in Ref. [239]. The implications of these different initializations are discussed at the end of Sec. 5.4.2.

All FSSH and RPSH simulations were performed in the adiabatic basis starting in the lower adiabatic state and the trajectories were propagated until they reached a region far away from the coupling region.

5.4.2 Results

To compare the different simulation methods in terms of electronic dynamics, I compare the evolution of the reduced electron density matrix $\underline{\rho}$ as a function of time. I use the diabatic basis to compute the reduced electron density matrix since the adiabatic basis depends on the nuclear position, which becomes problematic when tracing out the nuclear DOF to get the reduced density matrix. More specifically in the case of FSSH and RPSH methods, the ensemble-averaged density matrix is obtained by transforming the single-trajectory density matrix at each time step to the diabatic representation and then averaging over all trajectories. I also inspect the purity

$$\text{Tr}(\underline{\rho}^2) = \rho_{11}^2 + \rho_{22}^2 + 2|\rho_{12}|^2, \quad (5.29)$$

which is a basis-independent quantity, i.e., diabatic and adiabatic bases yield the same result.

Density matrix results

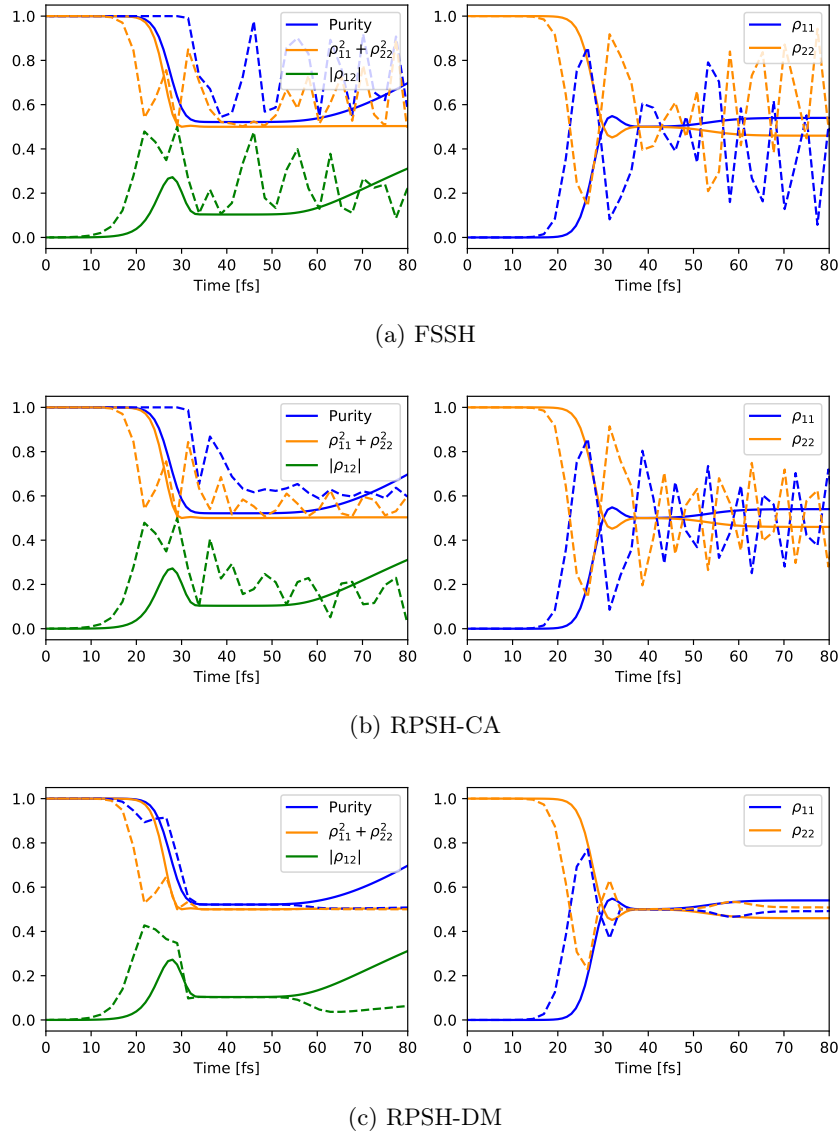


FIGURE 5.3: Reduced electronic density matrix in diabatic representation over time for Tully model C using (a) FSSH, (b) RPSH-CA, and (c) RPSH-DM (dashed lines) along with full quantum results (solid lines). Purity, sum of square of populations ($\rho_{11}^2 + \rho_{22}^2$), and absolute value of coherences ($|\rho_{12}|$) are shown in the left figures; populations are shown on the right. 64 beads were used for both RPSH methods. Figure taken from Ref. [241]. ©2023 American Physical Society.

The results for purity and density matrix elements are shown in Fig. 5.3. Results for FSSH, RPSH-CA, and RPSH-DM are given by dashed lines in each respective subfigure, and the full quantum dynamics results are shown as solid lines for comparison. To interpret the results, I will first describe the evolution of the full quantum dynamics. As one can see from the increase in $|\rho_{12}|$, at around 20 fs the wave packet enters the region where coupling between the two electronic states occurs. A decline in ρ_{22} and an increase in ρ_{11} indicates a corresponding population transfer. This

transfer in population is accompanied by a loss of purity. At around 28 fs, the wave packet components on the two surfaces start to dephase leading to some decline of $|\rho_{12}|$. After the wave packet has traversed the coupling region it enters the region near $R = 0$ a.u., where there is a steep potential rise in the upper adiabat and a decline in the lower adiabat [see Fig. 5.2(b)]. The initial momentum kick of $P_o = 20$ a.u. for the wave packet is insufficient to overcome the potential barrier and therefore part of the wave packet in the upper adiabat is reflected and only the part in the lower adiabat passes through. Finally, the reflected wave packet re-enters the coupling region at around 55 fs. Due to this, there is further coupling between the electronic states that leads to an increase in $|\rho_{12}|$ and some population transfer from the upper to the lower adiabatic state.

I now compare the full quantum dynamics with the results from FSSH, RPSH-CA, and RPSH-DM. The first thing to notice for all three methods is that the gain in coherence and population transfer occurs earlier, already at around 10 fs. I attribute this discrepancy to the fact that the dynamics are computed in the adiabatic basis where the rise in NAC is earlier than the off-diagonal coupling in the diabatic basis (see Fig. 5.2). This early rise in coherence in the adiabatic basis is carried forward to $|\rho_{12}|$ in the diabatic basis of the reduced density matrix. This artifact is inherent to surface hopping methods where results in adiabatic and diabatic bases are in general not fully equivalent [63].

As can be seen from Fig. 5.3(a) and Fig. 5.3(b), the FSSH and RPSH-CA results show strong discrepancies to the full quantum dynamics results. For both methods, populations (ρ_{11} and ρ_{22}) as well as $|\rho_{12}|$ oscillate. The purity declines considerably later than for the full quantum dynamics and also oscillates for FSSH. Apart from the aforementioned early onset of coherence, the RPSH-DM method reproduces the full quantum dynamics better than the other two methods [see Fig. 5.3(c)]. After having passed the coupling region at $t > 30$ fs, all the reduced density matrix elements are almost precisely at the value of the full quantum dynamics. However, for times $t > 55$ fs discrepancies arise. RPSH-DM does not capture the increase of purity and ρ_{12} at around 55 fs and instead shows a decline at $t > 55$ fs.

Note that using FSSH with an ensemble of trajectories with initial positions and momenta sampled according to the Wigner distribution of the initial wave packet in Eq. (5.27) does give better results with well-reproduced reduced density matrix elements, similar to RPSH-DM (results are not shown here). Additionally, I note here that the results presented here for RPSH-CA are somewhat different as compared to those in Ref. [239] due to different initialization. This aspect is further discussed later in this results section.

Single-trajectory analysis

To further understand why FSSH and RPSH-CA fail to reproduce full quantum dynamics results and in order to point out the relevant mechanisms present in RPSH-DM to capture electronic decoherence, I investigate a single trajectory that is reflected at

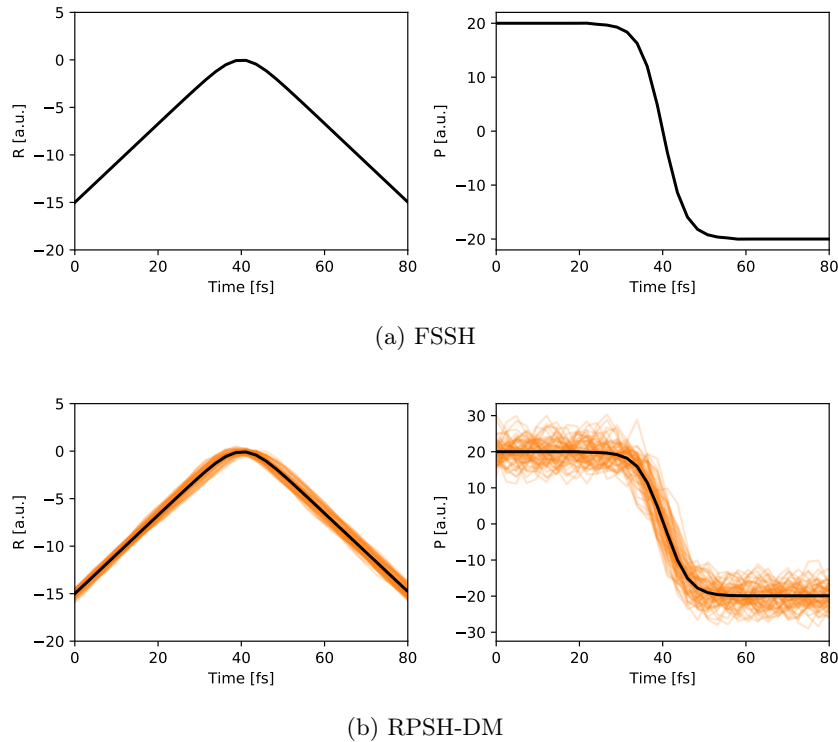


FIGURE 5.4: Position R (left) and momentum P (right) over time of a single trajectory that is reflected back in Tully model C with 20 a.u. initial momentum using (a) FSSH and (b) RPSH-DM with $\beta = 10520$ a.u. For RPSH-DM, individual bead quantities are shown in semi-transparent orange and the centroid quantity is shown as a solid black line. Figure taken from Ref. [241]. ©2023 American Physical Society.

the potential barrier. The position R and momentum P over time for such a trajectory are shown in Fig. 5.4 for FSSH and RPSH-DM (individual bead quantities are shown as orange lines and the centroid quantity is shown in black). As can be seen, the trajectories start at $R = -15$ a.u. and $P = 20$ a.u. and become reflected by the potential wall at around 40 fs. Through the multiple beads, the ring polymer describes a spatial spread in position and momentum, the average position and momentum follow similar dynamics as for the FSSH trajectory.

To further demonstrate the mechanism of decoherence captured within a single trajectory in RPSH-DM, I plot the individual bead density matrix elements for the same exemplary trajectory from Fig. 5.4. Figure 5.5 shows the populations ρ_{11} and ρ_{22} as well as the absolute value and phase of ρ_{12} . The values after averaging over the beads are shown in black. Due to the variations in the bead positions shown in Fig. 5.4(b), some variation in the density matrix elements of each bead can be seen. At the onset of coupling at about 20 fs, the population ρ_{22} declines, ρ_{11} increases, and the absolute value of ρ_{12} increases as well. All density matrix elements are still relatively close in absolute value and phase up to 25 fs. But soon after this, the absolute value of the bead-averaged ρ_{12} declines because the different beads cover different phases, which leads to diminished ρ_{12} upon averaging. The individual bead populations start to spread and oscillate over the whole range of values from 0 to 1 causing the averaged

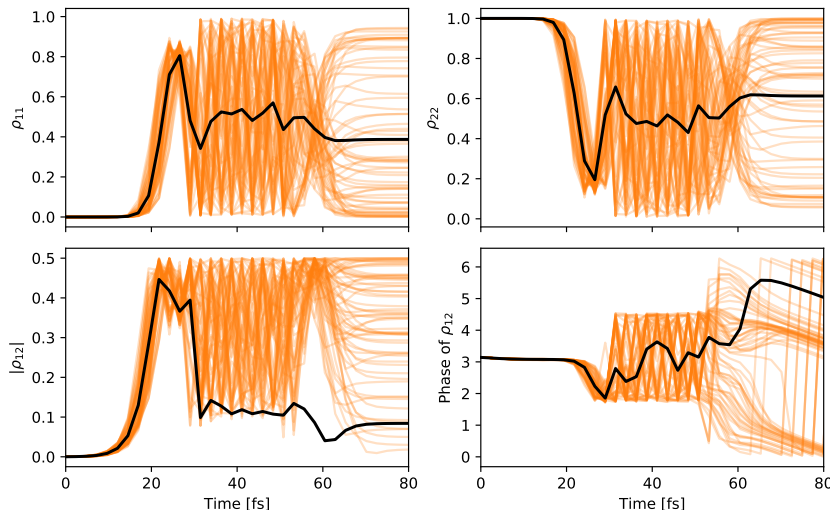


FIGURE 5.5: Individual bead density matrix elements in diabatic representation over time using RPSH-DM for the single trajectory shown in Fig. 5.4(b). Individual bead quantities are shown in semi-transparent orange and the bead averaged quantity is shown as a solid black line. Figure taken from Ref. [241]. ©2023 American Physical Society.

populations to be around 0.5.

After the ring polymer has traversed the coupling region, it gets reflected by the potential wall since this trajectory propagates on the upper adiabatic surface and re-enters the coupling region. At around 55 fs, there is a dip in $|\rho_{12}|$, and afterwards the populations remain constant as the ring polymer leaves the coupling region. This decrease in coherence is also seen in the ensemble case in Fig. 5.3(c), which is opposite to the increase seen in quantum dynamics. This discrepancy is due to the fact that in quantum dynamics, part of the wave packet is reflected on the upper adiabat and the other part is transmitted on the lower adiabat, and the reflected wave packet is initially only on a single surface. This is not captured by a single trajectory where even after reflecting, the electronic state contains populations on both states leading to different electronic dynamics. Strategies to overcome this problem would require additional resetting of the density matrix when the wave packet splits into contributions on two different surfaces.

Emphasis should be given to the fact that only RPSH-DM is able to incorporate decoherence in the nonadiabatic hopping dynamics as a consequence of ring polymer spreading mimicking the width of the wave packet. Since hopping probabilities are evaluated for each trajectory independently, FSSH and RPSH-CA cannot account for any decoherence in a single trajectory, owing to the fact that they employ only a single set of coherent electronic coefficients.

Varying the β parameter

I further discuss the dependence of RPSH-DM ensemble-average results on β . Figure 5.6 shows the electronic density matrix using RPSH-DM with β values of 100 a.u., 1052 a.u., and 50000 a.u. compared to the exact quantum results. The results for $\beta = 100$ a.u. exhibit highly oscillating density matrix elements. The results for this low β value are very similar to the conventional FSSH method. With higher β the RPSH-DM results show convergence. One can see that the results for $\beta = 50000$ a.u. are very similar compared to $\beta = 10520$ a.u. [see Fig. 5.3(c)]. The low-temperature limit results also become similar to the full quantum dynamics.

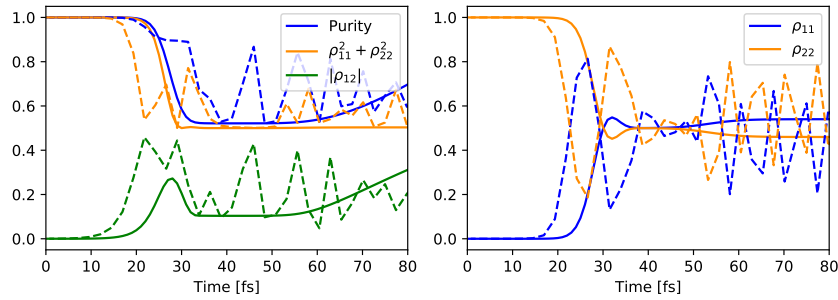
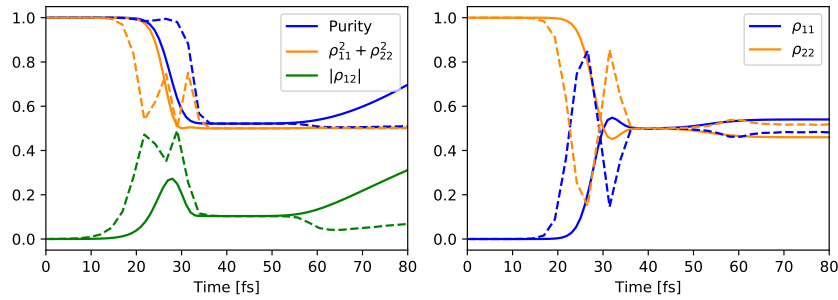
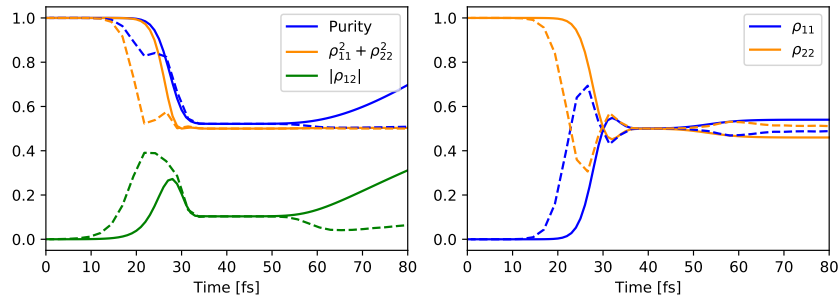
(a) RPSH-DM, $\beta = 100$ (b) RPSH-DM, $\beta = 1052$ (c) RPSH-DM, $\beta = 50000$

FIGURE 5.6: Reduced electronic density matrix in diabatic representation over time for Tully model C with 20 a.u. initial momentum using RPSH-DM with β values of (a) 100 a.u., (b) 1052 a.u., and (c) 50000 a.u. (dashed lines) along with quantum results (solid lines). 64 beads were used for all calculations. Figure taken from Ref. [241].

This finding can also be justified by understanding what the β parameter influences: β determines the spread of the ring polymer in the initial sampling as it determines the harmonic coupling between the beads of the ring polymer. To quantify this spread in position, I define the radius of gyration r_G for the ring polymer as

$$r_G = \sqrt{\frac{1}{n} \sum_{\alpha} |R^{(\alpha)} - \bar{R}|^2}. \quad (5.30)$$

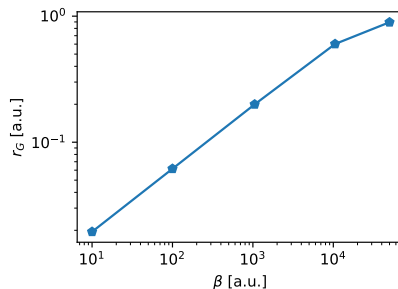


FIGURE 5.7: Ensemble-averaged radius of gyration for various β values obtained from PIMD sampling of the harmonic potential employed using 64 beads. Note that a log scale is used for both axes. Figure taken from Ref. [241]. ©2023 American Physical Society.

Figure 5.7 shows the ensemble-averaged r_G for different β values from the initial harmonic potential sampling done to initialize the ring polymer before propagating on Tully's model C potential. As can be seen from the figure, increasing β leads to an increase in the radius of gyration. Saturation is reached at very high β values due to the harmonic potential that eventually limits the extent of the ring polymer. This is different compared to a free ring polymer without any potential, whose radius of gyration keeps increasing with β . Using a small β simply leads to a shrinking of the ring polymer to a classical particle. Accordingly, RPSH-DM with small β is similar to performing FSSH. A larger β causes the ring polymer to spread in position and momentum space, thus leading to a better description of decoherence. Hence, the β -dependence demonstrated in Fig. 5.6 reflects a smooth transition from semiclassical dynamics to a full quantum dynamics description.

Previous RPSH-CA initialization and results

Here I discuss the results using RPSH-CA for Tully's model C again but using a different initialization than the one previously used in this chapter. Following Ref. [239], 32 beads and 20,000 samples are used and the momentum of *each* ring polymer bead is initially fixed to 20 a.u. The bead positions are sampled from the initial quantum Gaussian distribution in Eq. (5.27) with the same width and centered around -15 a.u. For the dynamics, since β was not set in the initialization, $\beta = 1/P_o$ is chosen and for

the case of $P_o = 20$ a.u., $\beta = 0.05$ a.u. is used. Centroid rescaling, which conserves centroid energy, is used when there is a surface hop instead of bead rescaling.

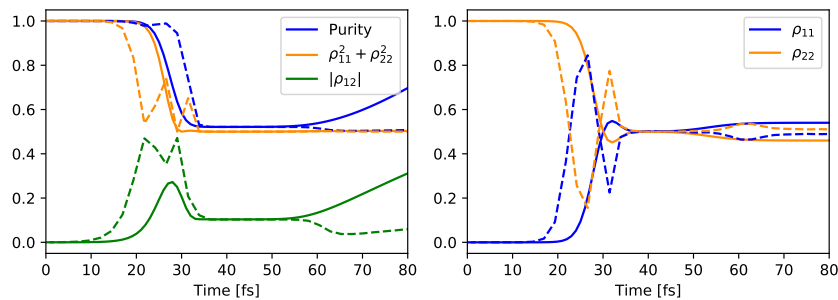


FIGURE 5.8: Reduced electronic density matrix in diabatic representation over time for Tully model C with 20 a.u. initial momentum using RPSH-CA (dashed lines) along with quantum results (solid lines). 32 beads were used and a different initialization than in Fig. 5.3 is used.

Figure taken from Ref. [241]. ©2023 American Physical Society.

Figure 5.8 shows the results using RPSH-CA with this initialization, leading to a significant improvement compared to the RPSH-CA results using the initialization presented before [see Fig. 5.3(b)] and is comparable to the RPSH-DM results with $\beta = 1052$ a.u. [see Fig. 5.6(b)]. At first glance, it appears to capture decoherence occurring at around 30 fs, even though a single trajectory only propagates a coherent electronic state. Taking a closer look at a single trajectory and how it is initialized reveals the issue with setting up the ring polymer this way.

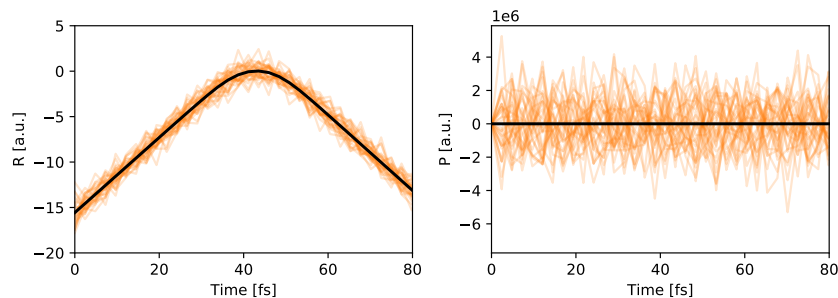


FIGURE 5.9: Position R (left) and momentum P (right) over time of a single trajectory that is reflected back in Tully model C with 20 a.u. initial centroid momentum using RPSH-CA with the initialization employed in Ref [239]. Individual bead quantities are shown in semi-transparent orange and the centroid quantity is shown as a solid black line. Figure taken from Ref. [241]. ©2023 American Physical Society.

Figure 5.9 shows bead positions and momenta for a trajectory that is reflected back with bead quantities shown in orange and the centroid in black. The bead positions have a small fluctuation around the centroid, but the momenta show very large fluctuations because of how the system is initialized. Using a very small β of 0.05 a.u. should result almost in a classical particle with a very small radius of gyration

(see Fig. 5.7). However, the position distribution is artificially made to resemble the quantum Gaussian distribution, which results in an extremely large ring polymer energy, and hence, very high bead momenta. Although this initialization does not match the quantum setup, it still gives width to the centroid position and momentum distributions in the ensemble case. This ultimately leads to the observed decoherence in Fig. 5.8 since in RPSH-CA only the centroid position matters for the electronic coefficient propagation. However, it was already shown by Tully in his original work in Ref. [66] that applying a Gaussian distribution for the momenta instead of a fixed momentum leads to better results for model C.

5.5 Summary

In summary, I presented my new RPSH-DM method, which provides improved surface hopping dynamics giving a better description of the reduced electron density matrix. This is done by combining RPMD and FSSH in a specific manner by using the spread of the ring polymer to mimic the width of the quantum nuclear wave packet. By doing so, I showed that decoherence through dephasing of different nuclear wave packet components is captured by the construction of a reduced electronic density matrix. Applying the new method to Tully's extended-coupling-with-reflection model (model C), I showed the ability to capture this mechanism of decoherence as opposed to FSSH or a previous attempt for RPSH, namely RPSH-CA [90]. Additionally, since the reduced electronic density matrix is calculated for each trajectory separately, every independent trajectory also shows decoherence in its time evolution, which naturally allows for incorporating decoherence in the hopping probabilities within each trajectory. This is not the case for FSSH and RPSH-CA since coherent electronic states are propagated.

Chapter 6

Conclusion and outlook

The dream of following the motion of nuclei and electrons in real time is turning into a reality with advances in laser technologies. Aided by theoretical simulations, these technologies can unravel the ultrafast processes initiated by excitation or ionization. In this thesis, I performed *ab initio* quantum-classical dynamics simulations using Tully's fewest switches surface hopping (FSSH) to simulate time-resolved x-ray absorption spectra (TRXAS) of ionized urea in both gas and liquid phases, and showed how information about nuclear and electronic dynamics can be extracted from the spectra. In addition, I also developed a new method ring polymer surface hopping-density matrix approach (RPSH-DM) that improves upon FSSH to describe electronic coherences more accurately. Now I will discuss the conclusions drawn and outlook for all of these different studies, first individually and then for the overall thesis.

In Chapter 3, I demonstrated how valuable insights can be obtained through TRXAS into the ultrafast dynamics occurring upon valence ionization of urea monomer and dimer in vacuum, which was simulated by applying FSSH with Koopmans' theorem. Both nuclear and electronic dynamics left distinct marks on the TRXAS, namely as intensity variations and a blueshift on the spectra, respectively. By providing a detailed description of how the dynamics of a simple, yet biologically relevant molecule are reflected in the TRXAS, I demonstrated in this work how statistical analysis tools, namely partial least square regression (PLSR), can be used to unravel the often complicated relationship between the dynamics and the spectra. To be precise, PLSR yielded collective coordinates that explain most of the intensity variance in the spectra, which were identified as some specific vibrations for the monomer and proton transfer for the dimer. This step becomes particularly crucial when large molecules are addressed, where the numerous vibrational degrees of freedom prohibits a clear interpretation via visual inspection of the simulated trajectories. In future work, it would be interesting to calculate other time-resolved spectra such as photoemission or resonant inelastic X-ray scattering (RIXS) for urea and analyze them using the PLSR method outlined here, as they provide complementary information to TRXAS on the dynamics. Additionally, the simulation and analysis methods developed here will be applicable to gain insights into the effects of ionizing radiation on larger biological systems such as DNA base pairs.

Extending the previous study to ionized urea in aqueous solution using quantum

mechanics/molecular mechanics (QM/MM) scheme in Chapter 4 added a lot of complexity due to interactions with the solvent and random orientation of ureas present. However, I showed that one can follow proton transfer between two hydrogen-bonded ureas, even in the case of aqueous urea using TRXAS. By looking at the carbon pre-edge absorption resonance, in particular, we were able to identify blueshift and rising intensity in the spectra as an effect of proton transfer and electronic hole rearrangement, respectively. Our simulated spectra agreed qualitatively well with recent experimental work on aqueous urea. These results thus establish the potential of water-window XAS for disentangling electronic and structural dynamics in ultrafast nonadiabatic dynamics of complex systems in a liquid environment.

Returning to the established significance of concentrated urea solutions in understanding the origin of life as discussed at the beginning of Chapter 4, our measurements identify the primary quantum mechanical events of ionization-induced chemistry in such prebiotically relevant systems. This reaction was also observed for the dimer in vacuum as shown in Chapter 3, but the timescale in the liquid phase is slower in comparison due to the effect of the aqueous surrounding. Furthermore, this is also remarkably similar in its nature to proton transfer in ionized water (bulk or clusters) [35, 168, 243], $\text{H}_2\text{O}\cdots\text{HOH}^+ \rightarrow \text{H}_3\text{O}^+\cdots\text{OH}$ and in ionized alcohols [28], $\text{ROH}\cdots\text{HOR}^+ \rightarrow \text{ROH}_2^+\cdots\text{OR}$, where R stands for the organic rest of the alcohol molecule. However, the proton transfer in the ionized urea dimer is notably slower than in ionized water or alcohols. Our results, therefore, identify an interesting similarity in the earliest steps of ionization-induced ultrafast chemistry of hydrogen-bonded systems. The identified urea-radical product is indeed unlikely to be stable, and will probably react further, just as OH radicals in ionized liquid water. Hence, our results establish the most elementary steps in reaction sequences that are likely to lie at the origin of life on earth. Future work can now be envisaged to address the subsequent reaction steps and understand how malonic acid and nucleobases are being formed after ionizing urea. Another aspect to consider for the future would be to use more sophisticated QM/MM schemes such as electrostatic embedding as discussed in Sec. 2.3 instead of the simple subtractive ONIOM approach taken in this work. This would include polarization from the MM region on the QM calculations, allowing for a more accurate description of the effect of the environment on the reaction dynamics and the spectra.

Finally, I presented the new RPSH-DM method in Chapter 5 developed to solve the overcoherence problem in FSSH, giving a more accurate description of electronic coherence and decoherence phenomena, as shown by applying this method to a one-dimensional Tully's model potential. By evaluating hopping probabilities through a density matrix formalism, this new method is capable of capturing electronic decoherence through dephasing mechanism, even for the case of a single trajectory. This is not the case for FSSH or previous RPSH methods [90]. However, RPSH-DM does not capture certain decoherence mechanisms such as due to a reduction of nuclear

wave packet overlap on different potential energy surfaces (PES), in contrast to methods that reset the density matrix when the wave packet starts to separate on two surfaces [85]. By finding a suitable way to combine RPSH-DM with these resetting methods, future work could incorporate this decoherence mechanism as well. An alternative would be to spawn a ring polymer on the second PES instead of hopping when it enters the nonadiabatic coupling (NAC) region such that the two ring polymers can move independently of each other. This would be similar to the *ab initio* multiple spawning method [58]. The computational cost of full quantum methods limits exact simulations of coupled electronic and nuclear dynamics to rather small systems and short time scales [229–231]. The available mixed quantum-classical dynamics methods such as FSSH lacked proper decoherence mechanisms [82, 85], which can be a critical issue for interpreting results for attosecond science. The inclusion of decoherence via the RPSH-DM method developed in the present work prospectively allows simulations of larger molecules and for longer time scales. Such a tool can be vital in simulating ultrafast electronic processes such as charge migration in polyatomic molecules and support the interpretation of attosecond experiments [222]. The next logical step to be done in future works could be to test the capabilities of the RPSH-DM method beyond model systems as done in this work and go to molecules such as water and phenylalanine, where exact quantum results already exists [229, 244].

This thesis overall contributes by providing an efficient quantum-classical dynamics method developed to obtain a better description of electronic coherences, and showing how nuclear and electronic dynamical features can be mapped onto time-resolved spectra which can then be compared with experiments. Combining these two parts, one can envision extending TRXAS in both gas and liquid phases to the attosecond time scale. Experimentally this has been done in the gas phase [29]. With the advances from this thesis, it should be possible to have reliable simulations for large molecules in the liquid phase and get a good interpretation of their spectra. Attosecond TRXAS can address the influence of electronic coherences on the dynamics, for instance, the impact on proton transfer reaction due to coherences between multiple electronic states created in valence ionization of ureas, and also study the possibility for electronic control [229, 230, 245] of such fundamental bio-relevant reactions.

Appendix A

Experimental details

A.1 Setup

The experimental setup consists of a laser-light source providing ultrashort laser pulses, a soft-X-ray (SXR) high-harmonic source, a liquid-flat-jet absorption chamber and a flat-field SXR spectrometer. The laser source consists of a titanium:sapphire laser system with an average power of 17 W, delivering ~ 40 fs pulses centered at 800 nm. This laser beam is split in a 90:10 ratio with the more intense part directed to a commercial optical parametric amplifier to generate ~ 45 fs, passively carrier-envelope-phase-stable idler pulses centered at 1800 nm. These pulses are further compressed via two-stage spectral broadening in filaments and compression in bulk glass down to ~ 12 fs and used for HHG in a high-pressure He gas target, as described in Ref. [195]. The weaker part of the beam is frequency-doubled in a beta-barium-borate (BBO) crystal to 400 nm, focused with a 1 m focal length and recombined with the broadband soft X-ray beam by means of a perforated mirror. The SXR beam transmitted through the liquid jet is dispersed via a variable-line-spacing (VLS) grating from Hitachi (2400 lines/mm) and recorded with an X-ray CCD camera from Andor. Additional details on the experimental setup can be found in Ref. [28].

A.2 Sample Preparation and Delivery

The various concentrated urea solutions were prepared from >99 % purity urea samples purchased from Sigma Aldrich and dissolved in purified liquid water with an electrical resistivity of ~ 18.0 M Ω cm. The flat jet is created by collision of two cylindrical jets emanating from quartz capillaries with orifices of about 18 μm and crossed at an angle of 48° . The thickness of the flatjet in the laser/SXR propagation direction is around 500 nm. The urea solution is delivered into the interaction region via an HPLC pump. A more comprehensive description of the flat jet including sheet shape, thickness and temperature measurements can be found in Refs. [194, 246, 247].

A.3 Energy Calibration

X-ray absorption K-edges of carbon and nitrogen from urea solutions measured at synchrotron facilities were utilized as reference energy points for the energy calibration

in this work. The carbon K-edge of aqueous urea was previously measured to be at 289.8 eV [206] and the nitrogen K-edge at 402.0 eV [197].

Bibliography

- [1] M. Dantus, M. J. Rosker, and A. H. Zewail, “Real-time femtosecond probing of “transition states” in chemical reactions”, *The Journal of Chemical Physics*, vol. 87, no. 4, pp. 2395–2397, 1987.
- [2] A. H. Zewail, “Laser femtochemistry”, *Science*, vol. 242, no. 4886, pp. 1645–1653, 1988.
- [3] A. H. Zewail, “Femtochemistry: 1667em Atomic-Scale Dynamics of the Chemical Bond”, *J. Phys. Chem. A*, vol. 104, no. 24, pp. 5660–5694, Jun. 2000, ISSN: 1089-5639. DOI: [10.1021/jp001460h](https://doi.org/10.1021/jp001460h).
- [4] T Pfeifer, C. Spielmann, and G Gerber, “Femtosecond x-ray science”, *Reports on Progress in Physics*, vol. 69, no. 2, p. 443, 2006.
- [5] K. Yamane, Z. Zhang, K. Oka, R. Morita, M. Yamashita, and A. Suguro, “Optical pulse compression to 3.4 fs in the monocycle region by feedback phase compensation”, *Optics Letters*, vol. 28, no. 22, pp. 2258–2260, 2003.
- [6] W. C. Röntgen, “On a new kind of rays”, *Science*, vol. 3, no. 59, pp. 227–231, 1896.
- [7] R. Schoenlein, S Chattopadhyay, H. Chong, T. Glover, P. Heimann, C. Shank, A. Zholents, and M. Zolotarev, “Generation of femtosecond pulses of synchrotron radiation”, *Science*, vol. 287, no. 5461, pp. 2237–2240, 2000.
- [8] R Mitzner, A. Sorokin, B Siemer, S Roling, M Rutkowski, H Zacharias, M Neeb, T Noll, F Siewert, W Eberhardt, *et al.*, “Direct autocorrelation of soft-x-ray free-electron-laser pulses by time-resolved two-photon double ionization of He”, *Physical Review A*, vol. 80, no. 2, p. 025 402, 2009.
- [9] R. Moshhammer, T. Pfeifer, A. Rudenko, Y. Jiang, L. Foucar, M. Kurka, K. Kühnel, C. D. Schröter, J Ullrich, O. Herrwerth, *et al.*, “Second-order autocorrelation of xuv fel pulses via time resolved two-photon single ionization of He”, *Optics express*, vol. 19, no. 22, pp. 21 698–21 706, 2011.
- [10] W. Helml, A. Maier, W Schweinberger, I. Grguraš, P Radcliffe, G Doumy, C Roedig, J. Gagnon, M Messerschmidt, S Schorb, *et al.*, “Measuring the temporal structure of few-femtosecond free-electron laser x-ray pulses directly in the time domain”, *Nature photonics*, vol. 8, no. 12, pp. 950–957, 2014.

- [11] S Serkez, G Geloni, S Tomin, G Feng, E. Gryzlova, A. Grum-Grzhimailo, and M Meyer, “Overview of options for generating high-brightness attosecond x-ray pulses at free-electron lasers and applications at the european XFEL”, *Journal of Optics*, vol. 20, no. 2, p. 024 005, 2018.
- [12] N Hartmann, G Hartmann, R Heider, M. Wagner, M Ilchen, J Buck, A. Lindahl, C Benko, J Grünert, J Krzywinski, *et al.*, “Attosecond time–energy structure of x-ray free-electron laser pulses”, *Nature Photonics*, vol. 12, no. 4, pp. 215–220, 2018.
- [13] J. Duris, S. Li, T. Driver, E. G. Champenois, J. P. MacArthur, A. A. Lutman, Z. Zhang, P. Rosenberger, J. W. Aldrich, R. Coffee, *et al.*, “Tunable isolated attosecond x-ray pulses with gigawatt peak power from a free-electron laser”, *Nature Photonics*, vol. 14, no. 1, pp. 30–36, 2020.
- [14] E. Goulielmakis, M. Schultze, M Hofstetter, V. S. Yakovlev, J. Gagnon, M Uiberacker, A. L. Aquila, E. Gullikson, D. T. Attwood, R. Kienberger, *et al.*, “Single-cycle nonlinear optics”, *Science*, vol. 320, no. 5883, pp. 1614–1617, 2008.
- [15] J. Li, X. Ren, Y. Yin, K. Zhao, A. Chew, Y. Cheng, E. Cunningham, Y. Wang, S. Hu, Y. Wu, *et al.*, “53-attosecond x-ray pulses reach the carbon K-edge”, *Nature communications*, vol. 8, no. 1, pp. 1–5, 2017.
- [16] T. Gaumnitz, A. Jain, Y. Pertot, M. Huppert, I. Jordan, F. Ardana-Lamas, and H. J. Wörner, “Streaking of 43-attosecond soft-X-ray pulses generated by a passively CEP-stable mid-infrared driver”, *Optics express*, vol. 25, no. 22, pp. 27 506–27 518, 2017.
- [17] P. Wernet, K. Kunnus, I. Josefsson, I. Rajkovic, W. Quevedo, M. Beye, S. Schreck, S. Grübel, M. Scholz, D. Nordlund, *et al.*, “Orbital-specific mapping of the ligand exchange dynamics of Fe(CO)₅ in solution”, *Nature*, vol. 520, no. 7545, pp. 78–81, 2015.
- [18] S. Baker, J. S. Robinson, C. Haworth, H Teng, R. Smith, C. C. Chirila, M. Lein, J. Tisch, and J. P. Marangos, “Probing proton dynamics in molecules on an attosecond time scale”, *Science*, vol. 312, no. 5772, pp. 424–427, 2006.
- [19] P. M. Kraus, M. Zürch, S. K. Cushing, D. M. Neumark, and S. R. Leone, “The ultrafast x-ray spectroscopic revolution in chemical dynamics”, *Nature Reviews Chemistry*, vol. 2, no. 6, pp. 82–94, 2018.
- [20] L. X. Chen, X Zhang, and M. Shelby, “Recent advances on ultrafast x-ray spectroscopy in the chemical sciences”, *Chemical Science*, vol. 5, no. 11, pp. 4136–4152, 2014.
- [21] J. J. Rehr and R. C. Albers, “Theoretical approaches to x-ray absorption fine structure”, *Reviews of modern physics*, vol. 72, no. 3, p. 621, 2000.

- [22] E. Goulielmakis, Z.-H. Loh, A. Wirth, R. Santra, N. Rohringer, V. S. Yakovlev, S. Zherebtsov, T. Pfeifer, A. M. Azzeer, M. F. Kling, *et al.*, “Real-time observation of valence electron motion”, *Nature*, vol. 466, no. 7307, pp. 739–743, 2010.
- [23] A. R. Attar, A. Bhattacharjee, C. Pemmaraju, K. Schnorr, K. D. Closser, D. Prendergast, and S. R. Leone, “Femtosecond x-ray spectroscopy of an electrocyclic ring-opening reaction”, *Science*, vol. 356, no. 6333, pp. 54–59, 2017.
- [24] Y. Pertot, C. Schmidt, M. Matthews, A. Chauvet, M. Huppert, V. Svoboda, A. Von Conta, A. Tehlar, D. Baykusheva, J.-P. Wolf, and H. J. Wörner, “Time-resolved x-ray absorption spectroscopy with a water window high-harmonic source”, *Science*, vol. 355, no. 6322, pp. 264–267, 2017.
- [25] U. Bergmann and P. Glatzel, “X-ray emission spectroscopy”, *Photosynthesis research*, vol. 102, no. 2, pp. 255–266, 2009.
- [26] A. Stolow, A. E. Bragg, and D. M. Neumark, “Femtosecond Time-Resolved Photoelectron Spectroscopy”, *Chem. Rev.*, vol. 104, no. 4, pp. 1719–1758, Apr. 2004, ISSN: 0009-2665. DOI: [10.1021/cr020683w](https://doi.org/10.1021/cr020683w).
- [27] Y. Kobayashi, K. F. Chang, T. Zeng, D. M. Neumark, and S. R. Leone, “Direct mapping of curve-crossing dynamics in ibr by attosecond transient absorption spectroscopy”, *Science*, vol. 365, no. 6448, pp. 79–83, 2019.
- [28] A. D. Smith, T. Balčiūnas, Y.-P. Chang, C. Schmidt, K. Zinchenko, F. B. Nunes, E. Rossi, V. Svoboda, Z. Yin, J.-P. Wolf, and H. J. Wörner, “Femtosecond Soft-X-ray Absorption Spectroscopy of Liquids with a Water-Window High-Harmonic Source”, *J. Phys. Chem. Lett.*, vol. 11, no. 6, pp. 1981–1988, Mar. 2020. DOI: [10.1021/acs.jpcllett.9b03559](https://doi.org/10.1021/acs.jpcllett.9b03559).
- [29] K. S. Zinchenko, F. Ardana-Lamas, I. Seidu, S. P. Neville, J. van der Veen, V. U. Lanfaloni, M. S. Schuurman, and H. J. Wörner, “Sub-7-femtosecond conical-intersection dynamics probed at the carbon k-edge”, *Science*, vol. 371, no. 6528, pp. 489–494, 2021.
- [30] C. Bressler, C. Milne, V.-T. Pham, A. ElNahas, R. M. van der Veen, W. Gawelda, S. Johnson, P. Beaud, D. Grolimund, M. Kaiser, C. N. Borca, G. Ingold, R. Abela, and M. Chergui, “Femtosecond XANES Study of the Light-Induced Spin Crossover Dynamics in an Iron(II) Complex”, *Science*, vol. 323, no. 5913, pp. 489–492, Jan. 2009, ISSN: 0036-8075, 1095-9203. DOI: [10.1126/science.1165733](https://doi.org/10.1126/science.1165733).
- [31] H. T. Lemke, C. Bressler, L. X. Chen, D. M. Fritz, K. J. Gaffney, A. Galler, W. Gawelda, K. Haldrup, R. W. Hartsock, H. Ihee, J. Kim, K. H. Kim, J. H. Lee, M. M. Nielsen, A. B. Stickrath, W. Zhang, D. Zhu, and M. Cammarata, “Femtosecond X-ray Absorption Spectroscopy at a Hard X-ray Free Electron Laser: Application to Spin Crossover Dynamics”, *J. Phys. Chem. A*, vol. 117, no. 4, pp. 735–740, Jan. 2013, ISSN: 1089-5639. DOI: [10.1021/jp312559h](https://doi.org/10.1021/jp312559h).

- [32] Y. Ogi, Y. Obara, T. Katayama, Y.-I. Suzuki, S. Y. Liu, N. C.-M. Bartlett, N. Kurahashi, S. Karashima, T. Togashi, Y. Inubushi, K. Ogawa, S. Owada, M. Rubešová, M. Yabashi, K. Misawa, P. Slavíček, and T. Suzuki, “Ultraviolet photochemical reaction of $[\text{Fe}(\text{III})(\text{C}_2\text{O}_4)_3]^{3-}$ in aqueous solutions studied by femtosecond time-resolved X-ray absorption spectroscopy using an X-ray free electron laser”, *Structural Dynamics*, vol. 2, no. 3, p. 034901, Apr. 2015. DOI: [10.1063/1.4918803](https://doi.org/10.1063/1.4918803).
- [33] M. Levantino, H. T. Lemke, G. Schirò, M. Glowina, A. Cupane, and M. Cammarata, “Observing heme doming in myoglobin with femtosecond X-ray absorption spectroscopy”, *Structural Dynamics*, vol. 2, no. 4, p. 041713, May 2015. DOI: [10.1063/1.4921907](https://doi.org/10.1063/1.4921907).
- [34] M. L. Shelby, P. J. Lestrangle, N. E. Jackson, K. Haldrup, M. W. Mara, A. B. Stickrath, D. Zhu, H. T. Lemke, M. Chollet, B. M. Hoffman, X. Li, and L. X. Chen, “Ultrafast Excited State Relaxation of a Metalloporphyrin Revealed by Femtosecond X-ray Absorption Spectroscopy”, *J. Am. Chem. Soc.*, vol. 138, no. 28, pp. 8752–8764, Jul. 2016, ISSN: 0002-7863. DOI: [10.1021/jacs.6b02176](https://doi.org/10.1021/jacs.6b02176).
- [35] Z.-H. Loh, G. Doumy, C. Arnold, L. Kjellsson, S. H. Southworth, A. A. Haddad, Y. Kumagai, M.-F. Tu, P. J. Ho, A. M. March, R. D. Schaller, M. S.B. M. Yusof, T. Debnath, M. Simon, R. Welsch, L. Inhester, K. Khalili, K. Nanda, A. I. Krylov, S. Moeller, G. Coslovich, J. Koralek, M. P. Minitti, W. F. Schlotter, J.-E. Rubensson, R. Santra, and L. Young, “Observation of the fastest chemical processes in the radiolysis of water”, *Science*, vol. 367, no. 6474, pp. 179–182, Jan. 2020, ISSN: 0036-8075, 1095-9203. DOI: [10.1126/science.aaz4740](https://doi.org/10.1126/science.aaz4740).
- [36] Z. Li, M. E.-A. Madjet, O. Vendrell, and R. Santra, “Core-level transient absorption spectroscopy as a probe of electron hole relaxation in photoionized $\text{H}+(\text{H}_2\text{O})_n$ ”, *Faraday Discuss.*, vol. 171, no. 0, pp. 457–470, Nov. 2014, ISSN: 1364-5498. DOI: [10.1039/C4FD00078A](https://doi.org/10.1039/C4FD00078A).
- [37] S. P. Neville, V. Averbukh, M. Ruberti, R. Yun, S. Patchkovskii, M. Chergui, A. Stolow, and M. S. Schuurman, “Excited state X-Ray absorption spectroscopy: Probing both electronic and structural dynamics”, *J. Chem. Phys.*, vol. 145, no. 14, p. 144307, Oct. 2016, ISSN: 0021-9606. DOI: [10.1063/1.4964369](https://doi.org/10.1063/1.4964369).
- [38] S. P. Neville, M. Chergui, A. Stolow, and M. S. Schuurman, “Ultrafast x-ray spectroscopy of conical intersections”, *Phys. Rev. Lett.*, vol. 120, no. 24, p. 243001, 2018.
- [39] W. Hua, S. Mukamel, and Y. Luo, “Transient X-ray Absorption Spectral Fingerprints of the S1 Dark State in Uracil”, *J. Phys. Chem. Lett.*, vol. 10, no. 22, pp. 7172–7178, Nov. 2019. DOI: [10.1021/acs.jpcllett.9b02692](https://doi.org/10.1021/acs.jpcllett.9b02692).

- [40] K. Khalili, L. Inhester, C. Arnold, R. Welsch, J. W. Andreasen, and R. Santra, “Hole dynamics in a photovoltaic donor-acceptor couple revealed by simulated time-resolved X-Ray absorption spectroscopy”, *Struct. Dyn.*, vol. 6, no. 4, p. 044 102, 2019.
- [41] K. Khalili, L. Inhester, C. Arnold, A. S. Gertsen, J. W. Andreasen, and R. Santra, “Simulation of time-resolved x-Ray absorption spectroscopy of ultrafast dynamics in particle-hole-excited 4-(2-Thienyl)-2,1,3-Benzothiadiazole”, *Struct. Dyn.*, vol. 7, no. 4, p. 044 101, Jul. 2020. DOI: [10.1063/4.0000016](https://doi.org/10.1063/4.0000016).
- [42] N. H. List, A. L. Dempwolff, A. Dreuw, P. Norman, and T. J. Martínez, “Probing competing relaxation pathways in malonaldehyde with transient x-ray absorption spectroscopy”, *Chemical science*, vol. 11, no. 16, pp. 4180–4193, 2020.
- [43] U. N. Morzan, P. E. Videla, M. B. Soley, E. T. Nibbering, and V. S. Batista, “Vibronic dynamics of photodissociating ICN from simulations of ultrafast x-ray absorption spectroscopy”, *Angewandte Chemie*, vol. 132, no. 45, pp. 20 219–20 223, 2020.
- [44] Y. Shakya, L. Inhester, C. Arnold, R. Welsch, and R. Santra, “Ultrafast time-resolved x-ray absorption spectroscopy of ionized urea and its dimer through ab initio nonadiabatic dynamics”, *Struct. Dyn.*, vol. 8, no. 3, p. 034 102, May 2021. DOI: [10.1063/4.0000076](https://doi.org/10.1063/4.0000076).
- [45] C. Kleine, M. Ekimova, G. Goldsztejn, S. Raabe, C. Strüber, J. Ludwig, S. Yarlagadda, S. Eisebitt, M. J. J. Vrakking, T. Elsaesser, E. T. J. Nibbering, and A. Rouzée, “Soft X-ray Absorption Spectroscopy of Aqueous Solutions Using a Table-Top Femtosecond Soft X-ray Source”, *The Journal of Physical Chemistry Letters*, vol. 10, no. 1, pp. 52–58, 2019, ISSN: 1948-7185. DOI: [10.1021/acs.jpcllett.8b03420](https://doi.org/10.1021/acs.jpcllett.8b03420). [Online]. Available: <http://pubs.acs.org/doi/10.1021/acs.jpcllett.8b03420>.
- [46] D. Polli, P. Altoe, O. Weingart, K. M. Spillane, C. Manzoni, D. Brida, G. Tomasello, G. Orlandi, P. Kukura, R. A. Mathies, *et al.*, “Conical intersection dynamics of the primary photoisomerization event in vision”, *Nature*, vol. 467, no. 7314, pp. 440–443, 2010.
- [47] S. J. Cotton and W. H. Miller, “The symmetrical quasi-classical model for electronically non-adiabatic processes applied to energy transfer dynamics in site-exciton models of light-harvesting complexes”, *Journal of chemical theory and computation*, vol. 12, no. 3, pp. 983–991, 2016.
- [48] G. Groenhof, V. Modi, and D. Morozov, “Observe while it happens: Catching photoactive proteins in the act with non-adiabatic molecular dynamics simulations”, *Current Opinion in Structural Biology*, vol. 61, pp. 106–112, 2020.
- [49] H.-D. Meyer, U. Manthe, and L. S. Cederbaum, “The multi-configurational time-dependent Hartree approach”, *Chemical Physics Letters*, vol. 165, no. 1, pp. 73–78, 1990.

- [50] M. H. Beck, A. Jäckle, G. A. Worth, and H.-D. Meyer, “The multiconfiguration time-dependent Hartree (MCTDH) method: A highly efficient algorithm for propagating wavepackets”, *Physics reports*, vol. 324, no. 1, pp. 1–105, 2000.
- [51] H.-D. Meyer, “Studying molecular quantum dynamics with the multiconfiguration time-dependent Hartree method”, *Wiley Interdisciplinary Reviews: Computational Molecular Science*, vol. 2, no. 2, pp. 351–374, 2012.
- [52] H. Wang and M. Thoss, “Multilayer formulation of the multiconfiguration time-dependent Hartree theory”, *The Journal of chemical physics*, vol. 119, no. 3, pp. 1289–1299, 2003.
- [53] H. Wang, “Multilayer multiconfiguration time-dependent Hartree theory”, *The Journal of Physical Chemistry A*, vol. 119, no. 29, pp. 7951–7965, 2015.
- [54] E. J. Heller, “Time-dependent approach to semiclassical dynamics”, *The Journal of Chemical Physics*, vol. 62, no. 4, pp. 1544–1555, 1975.
- [55] E. J. Heller, “Frozen Gaussians: A very simple semiclassical approximation”, *The Journal of Chemical Physics*, vol. 75, no. 6, pp. 2923–2931, 1981.
- [56] T. J. Martínez, M Ben-Nun, and G. Ashkenazi, “Classical/quantal method for multistate dynamics: A computational study”, *The Journal of chemical physics*, vol. 104, no. 8, pp. 2847–2856, 1996.
- [57] T. J. Martínez and R. Levine, “Non-adiabatic molecular dynamics: Split-operator multiple spawning with applications to photodissociation”, *Journal of the Chemical Society, Faraday Transactions*, vol. 93, no. 5, pp. 941–947, 1997.
- [58] M. Ben-Nun, J. Quenneville, and T. J. Martínez, “Ab Initio Multiple Spawning: 1667em Photochemistry from First Principles Quantum Molecular Dynamics”, *J. Phys. Chem. A*, vol. 104, no. 22, pp. 5161–5175, Jun. 2000, ISSN: 1089-5639. DOI: [10.1021/jp994174i](https://doi.org/10.1021/jp994174i).
- [59] G. A. Worth and I. Burghardt, “Full quantum mechanical molecular dynamics using Gaussian wavepackets”, *Chemical physics letters*, vol. 368, no. 3-4, pp. 502–508, 2003.
- [60] G. Worth, M. Robb, and I Burghardt, “A novel algorithm for non-adiabatic direct dynamics using variational Gaussian wavepackets”, *Faraday discussions*, vol. 127, pp. 307–323, 2004.
- [61] D. V. Shalashilin, “Quantum mechanics with the basis set guided by Ehrenfest trajectories: Theory and application to spin-boson model”, *The Journal of chemical physics*, vol. 130, no. 24, p. 244 101, 2009.
- [62] B. F. Curchod and T. J. Martínez, “Ab initio nonadiabatic quantum molecular dynamics”, *Chemical reviews*, vol. 118, no. 7, pp. 3305–3336, 2018.
- [63] J. Tully, “Mixed quantum–classical dynamics”, *Faraday Discuss.*, vol. 110, pp. 407–419, 1998.

- [64] A. McLachlan, “A variational solution of the time-dependent Schrödinger equation”, *Molecular Physics*, vol. 8, no. 1, pp. 39–44, 1964.
- [65] S.-I. Sawada, A. Nitzan, and H. Metiu, “Mean-trajectory approximation for charge-and energy-transfer processes at surfaces”, *Physical Review B*, vol. 32, no. 2, p. 851, 1985.
- [66] J. C. Tully, “Molecular dynamics with electronic transitions”, *J. Chem. Phys.*, vol. 93, no. 2, pp. 1061–1071, 1990.
- [67] S. Hammes-Schiffer and J. C. Tully, “Proton transfer in solution: Molecular dynamics with quantum transitions”, *J. Chem. Phys.*, vol. 101, no. 6, pp. 4657–4667, 1994.
- [68] J. C. Tully and R. K. Preston, “Trajectory surface hopping approach to nonadiabatic molecular collisions: The reaction of H⁺ with D₂”, *The Journal of Chemical Physics*, vol. 55, no. 2, pp. 562–572, 1971.
- [69] C. Fermanian Kammerer and C. Lasser, “Single switch surface hopping for molecular dynamics with transitions”, *The Journal of chemical physics*, vol. 128, no. 14, p. 144102, 2008.
- [70] R. Crespo-Otero and M. Barbatti, “Recent advances and perspectives on nonadiabatic mixed quantum–classical dynamics”, *Chemical reviews*, vol. 118, no. 15, pp. 7026–7068, 2018.
- [71] I. Tavernelli, “Nonadiabatic molecular dynamics simulations: Synergies between theory and experiments”, *Accounts of chemical research*, vol. 48, no. 3, pp. 792–800, 2015.
- [72] J.-Y. Fang and S. Hammes-Schiffer, “Comparison of surface hopping and mean field approaches for model proton transfer reactions”, *The Journal of chemical physics*, vol. 110, no. 23, pp. 11166–11175, 1999.
- [73] M. Barbatti, M. Vazdar, A. J. Aquino, M. Eckert-Maksić, and H. Lischka, “The nonadiabatic deactivation paths of pyrrole”, *The Journal of chemical physics*, vol. 125, no. 16, p. 164323, 2006.
- [74] M. Eckert-Maksić, M. Vazdar, M. Ruckebauer, M. Barbatti, T. Müller, and H. Lischka, “Matrix-controlled photofragmentation of formamide: Dynamics simulation in argon by nonadiabatic QM/MM method”, *Physical Chemistry Chemical Physics*, vol. 12, no. 39, pp. 12719–12726, 2010.
- [75] C. Ciminelli, G. Granucci, and M. Persico, “The photoisomerization mechanism of azobenzene: A semiclassical simulation of nonadiabatic dynamics”, *Chemistry—A European Journal*, vol. 10, no. 9, pp. 2327–2341, 2004.
- [76] X. Li, D. Hu, Y. Xie, and Z. Lan, “Analysis of trajectory similarity and configuration similarity in on-the-fly surface-hopping simulation on multi-channel nonadiabatic photoisomerization dynamics”, *The Journal of Chemical Physics*, vol. 149, no. 24, p. 244104, 2018.

- [77] M. S. Topaler, M. D. Hack, T. C. Allison, Y.-P. Liu, S. L. Mielke, D. W. Schwenke, and D. G. Truhlar, “Validation of trajectory surface hopping methods against accurate quantum mechanical dynamics and semiclassical analysis of electronic-to-vibrational energy transfer”, *The Journal of chemical physics*, vol. 106, no. 21, pp. 8699–8709, 1997.
- [78] M. Barbatti, “Nonadiabatic dynamics with trajectory surface hopping method”, *Wiley Interdiscip. Rev. Comput. Mol. Sci.*, vol. 1, no. 4, pp. 620–633, 2011.
- [79] J. E. Subotnik, W. Ouyang, and B. R. Landry, “Can we derive Tully’s surface-hopping algorithm from the semiclassical quantum liouville equation? almost, but only with decoherence”, *The Journal of chemical physics*, vol. 139, no. 21, p. 211 101, 2013.
- [80] L. Wang, A. Akimov, and O. V. Prezhdo, “Recent progress in surface hopping: 2011–2015”, *J. Phys. Chem. Lett.*, vol. 7, no. 11, pp. 2100–2112, 2016.
- [81] J. E. Subotnik, A. Jain, B. Landry, A. Petit, W. Ouyang, and N. Bellonzi, “Understanding the Surface Hopping View of Electronic Transitions and Decoherence”, *Annu. Rev. Phys. Chem.*, vol. 67, no. 1, pp. 387–417, 2016. DOI: [10.1146/annurev-physchem-040215-112245](https://doi.org/10.1146/annurev-physchem-040215-112245).
- [82] J.-Y. Fang and S. Hammes-Schiffer, “Improvement of the internal consistency in trajectory surface hopping”, *J. Phys. Chem. A*, vol. 103, no. 47, pp. 9399–9407, 1999.
- [83] K. F. Wong and P. J. Rossky, “Dissipative mixed quantum-classical simulation of the aqueous solvated electron system”, *J. Chem. Phys.*, vol. 116, no. 19, pp. 8418–8428, 2002.
- [84] G. Granucci, M. Persico, and A. Zocante, “Including quantum decoherence in surface hopping”, *J. Chem. Phys.*, vol. 133, no. 13, p. 134 111, 2010.
- [85] J. E. Subotnik and N. Shenvi, “A new approach to decoherence and momentum rescaling in the surface hopping algorithm”, *J. Chem. Phys.*, vol. 134, no. 2, p. 024 105, 2011.
- [86] N. Shenvi, J. E. Subotnik, and W. Yang, “Phase-corrected surface hopping: Correcting the phase evolution of the electronic wavefunction”, *J. Chem. Phys.*, vol. 135, no. 2, p. 024 101, 2011.
- [87] J.-K. Ha, I. S. Lee, and S. K. Min, “Surface hopping dynamics beyond nonadiabatic couplings for quantum coherence”, *J. Phys. Chem. Lett.*, vol. 9, no. 5, pp. 1097–1104, 2018.
- [88] I. R. Craig and D. E. Manolopoulos, “Quantum statistics and classical mechanics: Real time correlation functions from ring polymer molecular dynamics”, *J. Chem. Phys.*, vol. 121, no. 8, pp. 3368–3373, 2004.
- [89] R. P. Feynman and A. R. Hibbs, *Quantum Mechanics and Path Integrals*. McGraw-Hill, 1965.

- [90] P. Shushkov, R. Li, and J. C. Tully, “Ring polymer molecular dynamics with surface hopping”, *J. Chem. Phys.*, vol. 137, no. 22, 22A549, 2012.
- [91] R. Kapral and G. Ciccotti, “Mixed quantum-classical dynamics”, *The Journal of chemical physics*, vol. 110, no. 18, pp. 8919–8929, 1999.
- [92] S. Nielsen, R. Kapral, and G. Ciccotti, “Non-adiabatic dynamics in mixed quantum-classical systems”, *Journal of Statistical Physics*, vol. 101, no. 1, pp. 225–242, 2000.
- [93] H.-D. Meyer and W. H. Miller, “A classical analog for electronic degrees of freedom in nonadiabatic collision processes”, *The Journal of Chemical Physics*, vol. 70, no. 7, pp. 3214–3223, 1979.
- [94] G. Stock and M. Thoss, “Semiclassical description of nonadiabatic quantum dynamics”, *Physical review letters*, vol. 78, no. 4, p. 578, 1997.
- [95] M. Thoss and G. Stock, “Mapping approach to the semiclassical description of nonadiabatic quantum dynamics”, *Physical Review A*, vol. 59, no. 1, p. 64, 1999.
- [96] R. E. Wyatt, C. L. Lopreore, and G. Parlant, “Electronic transitions with quantum trajectories”, *The Journal of Chemical Physics*, vol. 114, no. 12, pp. 5113–5116, 2001.
- [97] F. Agostini, A. Abedi, Y. Suzuki, and E. Gross, “Mixed quantum-classical dynamics on the exact time-dependent potential energy surface: A fresh look at non-adiabatic processes”, *Molecular Physics*, vol. 111, no. 22-23, pp. 3625–3640, 2013.
- [98] A. R. Leach, *Molecular modelling: principles and applications*. Pearson education, 2001.
- [99] A. Warshel and M. Levitt, “Theoretical studies of enzymic reactions: Dielectric, electrostatic and steric stabilization of the carbonium ion in the reaction of lysozyme”, *Journal of molecular biology*, vol. 103, no. 2, pp. 227–249, 1976.
- [100] M. Born and K. Huang, *Dynamical theory of crystal lattices*. Oxford University Press, 1954.
- [101] M. Born and J. Oppenheimer, “Zur Quantentheorie der Molekeln”, *Annalen der Physik*, vol. 389, no. 20, pp. 457–484, 1927.
- [102] H. Hellmann, *Einführung in die Quantenchemie*. Franz Deuticke, Leipzig, 1937.
- [103] R. P. Feynman, “Forces in molecules”, *Physical review*, vol. 56, no. 4, p. 340, 1939.
- [104] W. C. Swope, H. C. Andersen, P. H. Berens, and K. R. Wilson, “A computer simulation method for the calculation of equilibrium constants for the formation of physical clusters of molecules: Application to small water clusters”, *The Journal of chemical physics*, vol. 76, no. 1, pp. 637–649, 1982.

- [105] R. Santra, "Concepts in x-ray physics", *J. Phys. B*, vol. 42, no. 2, p. 023 001, 2008.
- [106] A. Szabo and N. S. Ostlund, *Modern quantum chemistry: introduction to advanced electronic structure theory*. Dover Publications Inc., 1996.
- [107] D. J. Tannor, *Introduction to quantum mechanics: a time-dependent perspective*. University Science Books, 2007.
- [108] H. M. Senn and W. Thiel, "QM/MM methods for biomolecular systems", *Angewandte Chemie International Edition*, vol. 48, no. 7, pp. 1198–1229, 2009.
- [109] E. Brunk and U. Rothlisberger, "Mixed quantum mechanical/molecular mechanical molecular dynamics simulations of biological systems in ground and electronically excited states", *Chemical reviews*, vol. 115, no. 12, pp. 6217–6263, 2015.
- [110] W. D. Cornell, P. Cieplak, C. I. Bayly, I. R. Gould, K. M. Merz, D. M. Ferguson, D. C. Spellmeyer, T. Fox, J. W. Caldwell, and P. A. Kollman, "A second generation force field for the simulation of proteins, nucleic acids, and organic molecules", *Journal of the American Chemical Society*, vol. 117, no. 19, pp. 5179–5197, 1995.
- [111] A. D. MacKerell Jr, D. Bashford, M. Bellott, R. L. Dunbrack Jr, J. D. Evanseck, M. J. Field, S. Fischer, J. Gao, H Guo, S. Ha, *et al.*, "All-atom empirical potential for molecular modeling and dynamics studies of proteins", *The journal of physical chemistry B*, vol. 102, no. 18, pp. 3586–3616, 1998.
- [112] W. L. Jorgensen and J. Tirado-Rives, "The OPLS [optimized potentials for liquid simulations] potential functions for proteins, energy minimizations for crystals of cyclic peptides and crambin", *Journal of the American Chemical Society*, vol. 110, no. 6, pp. 1657–1666, 1988.
- [113] C. L. Brooks III, D. A. Case, S. Plimpton, B. Roux, D. Van Der Spoel, and E. Tajkhorshid, "Classical molecular dynamics", *The Journal of chemical physics*, vol. 154, no. 10, p. 100 401, 2021.
- [114] Y. Han, D. Jiang, J. Zhang, W. Li, Z. Gan, and J. Gu, "Development, applications and challenges of ReaxFF reactive force field in molecular simulations", *Frontiers of Chemical Science and Engineering*, vol. 10, no. 1, pp. 16–38, 2016.
- [115] F. Maseras and K. Morokuma, "IMOMM: A new integrated ab initio plus molecular mechanics geometry optimization scheme of equilibrium structures and transition states", *Journal of Computational Chemistry*, vol. 16, no. 9, pp. 1170–1179, 1995.
- [116] M. Svensson, S. Humbel, R. D. J. Froese, T. Matsubara, S. Sieber, and K. Morokuma, "ONIOM:.1667em A Multilayered Integrated MO + MM Method for Geometry Optimizations and Single Point Energy Predictions. A Test for Diels-Alder Reactions and Pt(P(t-Bu)₃)₂ + H₂ Oxidative Addition", *J. Phys.*

- Chem.*, vol. 100, no. 50, pp. 19 357–19 363, Jan. 1996, ISSN: 0022-3654. DOI: [10.1021/jp962071j](https://doi.org/10.1021/jp962071j).
- [117] C. I. Bayly, P. Cieplak, W. Cornell, and P. A. Kollman, “A well-behaved electrostatic potential based method using charge restraints for deriving atomic charges: The RESP model”, *The Journal of Physical Chemistry*, vol. 97, no. 40, pp. 10 269–10 280, 1993.
- [118] M. J. Field, P. A. Bash, and M. Karplus, “A combined quantum mechanical and molecular mechanical potential for molecular dynamics simulations”, *Journal of computational chemistry*, vol. 11, no. 6, pp. 700–733, 1990.
- [119] A. Warshel, P. K. Sharma, M. Kato, Y. Xiang, H. Liu, and M. H. Olsson, “Electrostatic basis for enzyme catalysis”, *Chemical reviews*, vol. 106, no. 8, pp. 3210–3235, 2006.
- [120] G. Groenhof, “Introduction to QM/MM simulations”, *Biomolecular Simulations*, pp. 43–66, 2013.
- [121] D. Chandler and P. G. Wolynes, “Exploiting the isomorphism between quantum theory and classical statistical mechanics of polyatomic fluids”, *The Journal of Chemical Physics*, vol. 74, no. 7, pp. 4078–4095, 1981.
- [122] M. Parrinello and A. Rahman, “Study of an F center in molten KCl”, *The Journal of chemical physics*, vol. 80, no. 2, pp. 860–867, 1984.
- [123] J. A. Barker, “A quantum-statistical Monte Carlo method; path integrals with boundary conditions”, *The Journal of Chemical Physics*, vol. 70, no. 6, pp. 2914–2918, 1979.
- [124] D. M. Ceperley, “Path integrals in the theory of condensed helium”, *Reviews of Modern Physics*, vol. 67, no. 2, p. 279, 1995.
- [125] B. J. Berne and D. Thirumalai, “On the simulation of quantum systems: Path integral methods”, *Annual Review of Physical Chemistry*, vol. 37, no. 1, pp. 401–424, 1986.
- [126] T. E. Markland and M. Ceriotti, “Nuclear quantum effects enter the mainstream”, *Nature Reviews Chemistry*, vol. 2, no. 3, pp. 1–14, 2018.
- [127] R. Kubo, “Statistical-mechanical theory of irreversible processes. I. general theory and simple applications to magnetic and conduction problems”, *Journal of the Physical Society of Japan*, vol. 12, no. 6, pp. 570–586, 1957.
- [128] I. R. Craig and D. E. Manolopoulos, “Chemical reaction rates from ring polymer molecular dynamics”, *J. Chem. Phys.*, vol. 122, no. 8, p. 084 106, 2005.
- [129] R. Collepardo-Guevara, Y. V. Suleimanov, and D. E. Manolopoulos, “Bimolecular reaction rates from ring polymer molecular dynamics”, *J. Chem. Phys.*, vol. 130, no. 17, p. 174 713, 2009.

- [130] T. F. Miller III and D. E. Manolopoulos, “Quantum diffusion in liquid parahydrogen from ring-polymer molecular dynamics”, *J. Chem. Phys.*, vol. 122, no. 18, p. 184503, 2005.
- [131] T. E. Markland, S. Habershon, and D. E. Manolopoulos, “Quantum diffusion of hydrogen and muonium atoms in liquid water and hexagonal ice”, *J. Chem. Phys.*, vol. 128, no. 19, p. 194506, 2008.
- [132] S. Habershon and D. E. Manolopoulos, “Zero point energy leakage in condensed phase dynamics: An assessment of quantum simulation methods for liquid water”, *The Journal of chemical physics*, vol. 131, no. 24, p. 244518, 2009.
- [133] T. J. Hele, M. J. Willatt, A. Muolo, and S. C. Althorpe, “Boltzmann-conserving classical dynamics in quantum time-correlation functions: “Matsubara dynamics””, *The Journal of Chemical Physics*, vol. 142, no. 13, p. 134103, 2015.
- [134] T. J. Hele, M. J. Willatt, A. Muolo, and S. C. Althorpe, “Communication: Relation of centroid molecular dynamics and ring-polymer molecular dynamics to exact quantum dynamics”, *The Journal of Chemical Physics*, vol. 142, no. 19, p. 191101, 2015.
- [135] R. Welsch, K. Song, Q. Shi, S. C. Althorpe, and T. F. Miller III, “Nonequilibrium dynamics from RPMD and CMD”, *J. Chem. Phys.*, vol. 145, no. 20, p. 204118, 2016.
- [136] A. Marjollet and R. Welsch, “Nuclear quantum effects in state-selective scattering from ring polymer molecular dynamics”, *J. Chem. Phys.*, vol. 152, no. 19, p. 194113, May 2020, ISSN: 0021-9606. DOI: [10.1063/5.0004179](https://doi.org/10.1063/5.0004179).
- [137] A. Marjollet, L. Inhester, and R. Welsch, “Initial state-selected scattering for the reactions $H + CH_4/CHD_3$ and $F + CHD_3$ employing ring polymer molecular dynamics”, *J. Chem. Phys.*, vol. 156, no. 4, p. 044101, Jan. 2022, ISSN: 0021-9606. DOI: [10.1063/5.0076216](https://doi.org/10.1063/5.0076216).
- [138] A. Marjollet and R. Welsch, “State-selective cross sections from ring polymer molecular dynamics”, *Int. J. Quantum Chem.*, vol. 121, no. 3, e26447, 2021, ISSN: 1097-461X. DOI: [10.1002/qua.26447](https://doi.org/10.1002/qua.26447).
- [139] J. Schmidt and J. C. Tully, “Path-integral simulations beyond the adiabatic approximation”, *J. Chem. Phys.*, vol. 127, no. 9, p. 094103, 2007.
- [140] N. Ananth, “Mapping variable ring polymer molecular dynamics: A path-integral based method for nonadiabatic processes”, *The Journal of chemical physics*, vol. 139, no. 12, p. 124102, 2013.
- [141] J. O. Richardson and M. Thoss, “Communication: Nonadiabatic ring-polymer molecular dynamics”, *The Journal of Chemical Physics*, vol. 139, no. 3, p. 031102, 2013.

- [142] J. O. Richardson, P. Meyer, M.-O. Pleinert, and M. Thoss, “An analysis of nonadiabatic ring-polymer molecular dynamics and its application to vibronic spectra”, *Chemical Physics*, vol. 482, pp. 124–134, 2017.
- [143] M. Baumann, M. Krause, J. Overgaard, J. Debus, S. M. Bentzen, J. Daartz, C. Richter, D. Zips, and T. Bortfeld, “Radiation oncology in the era of precision medicine”, *Nat. Rev. Cancer*, vol. 16, no. 4, pp. 234–249, Apr. 2016, ISSN: 1474-1768. DOI: [10.1038/nrc.2016.18](https://doi.org/10.1038/nrc.2016.18).
- [144] R. Neutze, R. Wouts, D. Van der Spoel, E. Weckert, and J. Hajdu, “Potential for biomolecular imaging with femtosecond X-ray pulses”, *Nature*, vol. 406, no. 6797, pp. 752–757, 2000.
- [145] F. E. Garrett-Bakelman, M. Darshi, S. J. Green, R. C. Gur, L. Lin, B. R. Macias, M. J. McKenna, C. Meydan, T. Mishra, J. Nasrini, B. D. Piening, L. F. Rizzardì, K. Sharma, J. H. Siamwala, L. Taylor, M. H. Vitaterna, M. Afkarian, E. Afshinnekoo, S. Ahadi, A. Ambati, M. Arya, D. Bezdán, C. M. Callahan, S. Chen, A. M. K. Choi, G. E. Chlipala, K. Contrepois, M. Covington, B. E. Crucian, I. De Vivo, D. F. Dinges, D. J. Ebert, J. I. Feinberg, J. A. Gandara, K. A. George, J. Goutsias, G. S. Grills, A. R. Hargens, M. Heer, R. P. Hillary, A. N. Hoofnagle, V. Y. H. Hook, G. Jenkinson, P. Jiang, A. Keshavarzian, S. S. Laurie, B. Lee-McMullen, S. B. Lumpkins, M. MacKay, M. G. Maienschein-Cline, A. M. Melnick, T. M. Moore, K. Nakahira, H. H. Patel, R. Pietrzyk, V. Rao, R. Saito, D. N. Salins, J. M. Schilling, D. D. Sears, C. K. Sheridan, M. B. Stenger, R. Tryggvadottir, A. E. Urban, T. Vaisar, B. Van Espen, J. Zhang, M. G. Ziegler, S. R. Zwart, J. B. Charles, C. E. Kundrot, G. B. I. Scott, S. M. Bailey, M. Basner, A. P. Feinberg, S. M. C. Lee, C. E. Mason, E. Mignot, B. K. Rana, S. M. Smith, M. P. Snyder, and F. W. Turek, “The NASA Twins Study: A multidimensional analysis of a year-long human spaceflight”, *Science*, vol. 364, no. 6436, Apr. 2019, ISSN: 1095-9203. DOI: [10.1126/science.aau8650](https://doi.org/10.1126/science.aau8650).
- [146] B. Ziaja, D. van der Spoel, A. Szöke, and J. Hajdu, “Auger-electron cascades in diamond and amorphous carbon”, *Phys. Rev. B*, vol. 64, no. 21, p. 214 104, Nov. 2001. DOI: [10.1103/PhysRevB.64.214104](https://doi.org/10.1103/PhysRevB.64.214104).
- [147] N. Tîmneanu, C. Caleman, J. Hajdu, and D. van der Spoel, “Auger electron cascades in water and ice”, *Chemical Physics*, *Ultrafast Science with X-Rays and Electrons*, vol. 299, no. 2, pp. 277–283, Apr. 2004, ISSN: 0301-0104. DOI: [10.1016/j.chemphys.2003.10.011](https://doi.org/10.1016/j.chemphys.2003.10.011).
- [148] C. Caleman, C. Ortiz, E. Marklund, F. Bultmark, M. Gabrysch, F. G. Parak, J. Hajdu, M. Klintonberg, and N. Tîmneanu, “Radiation damage in biological material: Electronic properties and electron impact ionization in urea”, *EPL*, vol. 85, no. 1, p. 18 005, Jan. 2009, ISSN: 0295-5075. DOI: [10.1209/0295-5075/85/18005](https://doi.org/10.1209/0295-5075/85/18005).

- [149] V. Stumpf, K. Gokhberg, and L. S. Cederbaum, “The role of metal ions in X-ray-induced photochemistry”, *Nat. Chem.*, vol. 8, no. 3, pp. 237–241, Mar. 2016, ISSN: 1755-4349. DOI: [10.1038/nchem.2429](https://doi.org/10.1038/nchem.2429).
- [150] M. E.-A. Madjet, O. Vendrell, and R. Santra, “Ultrafast Dynamics of Photoionized Acetylene”, *Phys. Rev. Lett.*, vol. 107, no. 26, p. 263 002, Dec. 2011. DOI: [10.1103/PhysRevLett.107.263002](https://doi.org/10.1103/PhysRevLett.107.263002).
- [151] S. Bazzi, R. Welsch, O. Vendrell, and R. Santra, “Challenges in XUV Photochemistry Simulations: A Case Study on Ultrafast Fragmentation Dynamics of the Benzene Radical Cation”, *J. Phys. Chem. A*, vol. 122, no. 4, pp. 1004–1010, Feb. 2018, ISSN: 1089-5639. DOI: [10.1021/acs.jpca.7b11543](https://doi.org/10.1021/acs.jpca.7b11543).
- [152] F. Wöhler, “Ueber künstliche Bildung des Harnstoffs”, *Ann. Phys.*, vol. 88, no. 2, pp. 253–256, 1828, ISSN: 1521-3889. DOI: [10.1002/andp.18280880206](https://doi.org/10.1002/andp.18280880206).
- [153] P. J. Ramberg, “The Death of Vitalism and The Birth of Organic Chemistry: Wohler’s Urea Synthesis and the Disciplinary Identity of Organic Chemistry”, *Ambix*, vol. 47, no. 3, pp. 170–195, Nov. 2000, ISSN: 0002-6980. DOI: [10.1179/amb.2000.47.3.170](https://doi.org/10.1179/amb.2000.47.3.170).
- [154] Y. Hao, L. Inhester, K. Hanasaki, S.-K. Son, and R. Santra, “Efficient electronic structure calculation for molecular ionization dynamics at high x-ray intensity”, *Struct. Dyn.*, vol. 2, no. 4, p. 041 707, 2015. DOI: <http://dx.doi.org/10.1063/1.4919794>.
- [155] L. Inhester, K. Hanasaki, Y. Hao, S.-K. Son, and R. Santra, “X-ray multiphoton ionization dynamics of a water molecule irradiated by an x-ray free-electron laser pulse”, *Phys. Rev. A*, vol. 94, no. 2, p. 023 422, Aug. 2016. DOI: [10.1103/PhysRevA.94.023422](https://doi.org/10.1103/PhysRevA.94.023422).
- [156] R. Ditchfield, W. J. Hehre, and J. A. Pople, “Self-consistent molecular-orbital methods. IX. An extended gaussian-type basis for molecular-orbital studies of organic molecules”, *J. Chem. Phys.*, vol. 54, 1971. DOI: [10.1063/1.1674902](https://doi.org/10.1063/1.1674902).
- [157] W. J. Hehre, R. Ditchfield, and J. A. Pople, “Self-Consistent Molecular Orbital Methods. XII. Further Extensions of Gaussian-Type Basis Sets for Use in Molecular Orbital Studies of Organic Molecules”, *J. Chem. Phys.*, vol. 56, no. 5, pp. 2257–2261, 1972. DOI: [10.1063/1.1677527](https://doi.org/10.1063/1.1677527).
- [158] P. C. Hariharan and J. A. Pople, “The influence of polarization functions on molecular orbital hydrogenation energies”, *Theor. Chim. Acta*, vol. 28, no. 3, pp. 213–222, 1973, ISSN: 1432-2234. DOI: [10.1007/BF00533485](https://doi.org/10.1007/BF00533485).
- [159] T. Clark, J. Chandrasekhar, G. W. Spitznagel, and P. V. R. Schleyer, “Efficient diffuse function-augmented basis sets for anion calculations. III. The 3-21+G basis set for first-row elements, Li–F”, *J. Comput. Chem.*, vol. 4, no. 3, pp. 294–301, 1983, ISSN: 1096-987X. DOI: [10.1002/jcc.540040303](https://doi.org/10.1002/jcc.540040303).

- [160] J. Gerratt and I. M. Mills, “Force Constants and Dipole-Moment Derivatives of Molecules from Perturbed Hartree–Fock Calculations. I”, *J. Chem. Phys.*, vol. 49, no. 4, pp. 1719–1729, Aug. 1968, ISSN: 0021-9606. DOI: [10.1063/1.1670299](https://doi.org/10.1063/1.1670299).
- [161] J. A. Pople, R. Krishnan, H. B. Schlegel, and J. S. Binkley, “Derivative studies in hartree-fock and møller-plesset theories”, *Int. J. Quantum Chem.*, vol. 16, no. S13, pp. 225–241, Mar. 1979, ISSN: 1097-461X. DOI: [10.1002/qua.560160825](https://doi.org/10.1002/qua.560160825).
- [162] B. Paizs and I. Mayer, “Coupled perturbed Hartree—Fock equations. An alternative derivation and generalization to non-orthogonal orbitals”, *Chem. Phys. Lett.*, vol. 220, no. 1-2, pp. 97–101, Mar. 1994, ISSN: 00092614. DOI: [10.1016/0009-2614\(94\)00139-1](https://doi.org/10.1016/0009-2614(94)00139-1).
- [163] T. H. Lee and J. W. Rabalais, “X-ray photoelectron spectra and electronic structure of some diamine compounds”, *J. Electron Spectrosc. Relat. Phenom.*, vol. 11, no. 1, pp. 123–127, Jan. 1977, ISSN: 0368-2048. DOI: [10.1016/0368-2048\(77\)85052-4](https://doi.org/10.1016/0368-2048(77)85052-4).
- [164] D. Dougherty, K. Wittel, J. Meeks, and S. P. McGlynn, “Photoelectron spectroscopy of carbonyls. Ureas, uracils, and thymine”, *J. Am. Chem. Soc.*, vol. 98, no. 13, pp. 3815–3820, Jun. 1976, ISSN: 0002-7863. DOI: [10.1021/ja00429a013](https://doi.org/10.1021/ja00429a013).
- [165] W. Humphrey, A. Dalke, and K. Schulten, “VMD – Visual Molecular Dynamics”, *J. Mol. Graph.*, vol. 14, pp. 33–38, 1996.
- [166] S. Wold, M. Sjöström, and L. Eriksson, “PLS-Regression: A basic tool of chemometrics”, *Chemom. Intell. Lab. Syst., PLS Methods*, vol. 58, no. 2, pp. 109–130, Oct. 2001, ISSN: 0169-7439. DOI: [10.1016/S0169-7439\(01\)00155-1](https://doi.org/10.1016/S0169-7439(01)00155-1).
- [167] C. Lee, E. A. Stahlberg, and G. Fitzgerald, “Chemical structure of urea in water”, *J. Phys. Chem.*, vol. 99, no. 50, pp. 17737–17741, 1995.
- [168] O. Marsalek, C. G. Elles, P. A. Pieniazek, E. Pluhařová, J. VandeVondele, S. E. Bradforth, and P. Jungwirth, “Chasing charge localization and chemical reactivity following photoionization in liquid water”, *J. Chem. Phys.*, vol. 135, no. 22, p. 224510, Dec. 2011, ISSN: 0021-9606. DOI: [10.1063/1.3664746](https://doi.org/10.1063/1.3664746).
- [169] S. L. Miller and H. C. Urey, “Organic compound synthesis on the primitive earth”, *Science*, vol. 130, no. 3370, pp. 245–251, 1959.
- [170] J. Oró and A. Kimball, “Synthesis of purines under possible primitive earth conditions. i. adenine from hydrogen cyanide”, *Archives of biochemistry and biophysics*, vol. 94, no. 2, pp. 217–227, 1961.
- [171] R. Navarro-Gonzalez, A. Negron-Mendoza, and E Chacon, “The γ -irradiation of aqueous solutions of urea. implications for chemical evolution”, *Origins of Life and Evolution of the Biosphere*, vol. 19, no. 2, pp. 109–118, 1989.

- [172] C. Menor Salván, M. Bouza, D. M. Fialho, B. T. Burcar, F. M. Fernández, and N. V. Hud, “Prebiotic origin of pre-rna building blocks in a urea “warm little pond” scenario”, *ChemBioChem*, vol. 21, no. 24, pp. 3504–3510, 2020.
- [173] H. Okamura, A. Crisp, S. Hübner, S. Becker, P. Rovó, and T. Carell, “Proto-urea-rna (wöhler rna) containing unusually stable urea nucleosides”, *Angewandte Chemie*, vol. 131, no. 51, pp. 18 864–18 869, 2019.
- [174] D. W. Deamer and G. R. Fleischaker, *Origins of life : the central concepts*. Boston: Jones and Bartlett Publishers, 1994, ISBN: 0867201819 9780867201819.
- [175] C. Menor-Salván, “From the dawn of organic chemistry to astrobiology: Urea as a foundational component in the origin of nucleobases and nucleotides”, in *Prebiotic Chemistry and Chemical Evolution of Nucleic Acids*, Springer, 2018, pp. 85–142.
- [176] J. F. Kasting, “Earth’s early atmosphere”, *Science*, vol. 259, no. 5097, pp. 920–926, 1993.
- [177] C. S. Cockell, “The ultraviolet radiation environment of earth and mars: Past and present”, in *Astrobiology*, Springer, 2002, pp. 219–232.
- [178] J. Florian and J. Leszczyński, “Spontaneous dna mutations induced by proton transfer in the guanine cytosine base pairs: An energetic perspective”, *Journal of the American Chemical Society*, vol. 118, no. 12, pp. 3010–3017, 1996.
- [179] P. H. Yancey, M. E. Clark, S. C. Hand, R. D. Bowlus, and G. N. Somero, “Living with Water Stress: Evolution of Osmolyte Systems”, *Science*, vol. 217, no. 4566, pp. 1214–1222, Sep. 1982. DOI: [10.1126/science.7112124](https://doi.org/10.1126/science.7112124).
- [180] P. Ganguly, J. Polák, N. Van Der Vegt, J. Heyda, and J.-E. Shea, “Protein Stability in TMAO and Mixed Urea-TMAO Solutions”, *J. Phys. Chem. B*, vol. 124, no. 29, pp. 6181–6197, 2020. DOI: [10.1021/acs.jpccb.0c04357](https://doi.org/10.1021/acs.jpccb.0c04357).
- [181] F. G. Hopkins, “Denaturation of proteins by urea and related substances”, *Nature*, vol. 126, pp. 328–+, Jul. 1930, ISSN: 0028-0836. DOI: [10.1038/126328a0](https://doi.org/10.1038/126328a0).
- [182] J. F. Brandts and L. Hunt, “Thermodynamics of protein denaturation. III. Denaturation of ribonuclease in water and in aqueous urea and aqueous ethanol mixtures”, *J. Am. Chem. Soc.*, vol. 89, no. 19, pp. 4826–4838, Sep. 1967, ISSN: 0002-7863. DOI: [10.1021/ja00995a002](https://doi.org/10.1021/ja00995a002).
- [183] M. Auton and D. W. Bolen, “Predicting the energetics of osmolyte-induced protein folding/unfolding”, *PNAS*, vol. 102, no. 42, pp. 15 065–15 068, Oct. 2005, ISSN: 0027-8424, 1091-6490. DOI: [10.1073/pnas.0507053102](https://doi.org/10.1073/pnas.0507053102).
- [184] J. L. England and G. Haran, “Role of solvation effects in protein denaturation: From thermodynamics to single molecules and back”, *Annual review of physical chemistry*, vol. 62, pp. 257–277, 2011.

- [185] D. R. Canchi and A. E. García, “Cosolvent effects on protein stability”, *Annual Review of Physical Chemistry*, vol. 64, no. 1, pp. 273–293, 2013, PMID: 23298246. DOI: [10.1146/annurev-physchem-040412-110156](https://doi.org/10.1146/annurev-physchem-040412-110156).
- [186] Y. Rezus and H. Bakker, “Effect of urea on the structural dynamics of water”, *Proc. Natl. Acad. Sci.*, vol. 103, no. 49, pp. 18 417–18 420, 2006.
- [187] A. K. Soper, E. W. Castner, and A. Luzar, “Impact of urea on water structure: A clue to its properties as a denaturant?”, *Biophys Chem*, vol. 105, no. 2-3, pp. 649–666, Sep. 2003, ISSN: 0301-4622. DOI: [10.1016/s0301-4622\(03\)00095-4](https://doi.org/10.1016/s0301-4622(03)00095-4).
- [188] A. Idrissi, “Molecular structure and dynamics of liquids: Aqueous urea solutions”, *Spectrochimica Acta Part A: Molecular and Biomolecular Spectroscopy*, vol. 61, no. 1, pp. 1–17, Jan. 2005, ISSN: 1386-1425. DOI: [10.1016/j.saa.2004.02.039](https://doi.org/10.1016/j.saa.2004.02.039).
- [189] M. C. Stumpe and H. Grubmüller, “Interaction of urea with amino acids: Implications for urea-induced protein denaturation”, *Journal of the American Chemical Society*, vol. 129, no. 51, pp. 16 126–16 131, 2007, ISSN: 00027863. DOI: [10.1021/ja076216j](https://doi.org/10.1021/ja076216j).
- [190] F. Ramondo, L. Bencivenni, R. Caminiti, A. Pieretti, and L. Gontrani, “Dimerisation of urea in water solution: A quantum mechanical investigation”, *Phys. Chem. Chem. Phys.*, vol. 9, no. 18, pp. 2206–2215, May 2007, ISSN: 1463-9084. DOI: [10.1039/B617837E](https://doi.org/10.1039/B617837E).
- [191] A. Idrissi, P. Damay, K. Yukichi, and P. Jedlovszky, “Self-association of urea in aqueous solutions: A Voronoi polyhedron analysis study”, *J. Chem. Phys.*, vol. 129, no. 16, p. 164 512, Oct. 2008, ISSN: 0021-9606. DOI: [10.1063/1.2996348](https://doi.org/10.1063/1.2996348).
- [192] N. Saito, H. Sannohe, N. Ishii, T. Kanai, N. Kosugi, Y. Wu, A. Chew, S. Han, Z. Chang, and J. Itatani, “Real-time observation of electronic, vibrational, and rotational dynamics in nitric oxide with attosecond soft x-ray pulses at 400 eV”, *Optica*, vol. 6, no. 12, pp. 1542–1546, 2019.
- [193] Z. Yin, Y.-P. Chang, T. Balčiūnas, Y. Shakya, A. Djorović, G. Gaulier, G. Fazio, R. Santra, L. Inhester, J.-P. Wolf, *et al.*, “Femtosecond proton transfer in urea solutions probed by x-ray spectroscopy”, *Nature*, 2023.
- [194] Z. Yin, T. T. Luu, and H. J. Wörner, “Few-cycle high-harmonic generation in liquids: In-operando thickness measurement of flat microjets”, *Journal of Physics: Photonics*, vol. 2, no. 4, p. 044 007, 2020.
- [195] C. Schmidt, Y. Pertot, T. Balciunas, K. Zinchenko, M. Matthews, H. J. Wörner, and J.-P. Wolf, “High-order harmonic source spanning up to the oxygen K-edge based on filamentation pulse compression”, *Optics Express*, vol. 26, no. 9, p. 11 834, 2018, ISSN: 1094-4087. DOI: [10.1364/OE.26.011834](https://doi.org/10.1364/OE.26.011834). [Online]. Available: <https://www.osapublishing.org/abstract.cfm?URI=oe-26-9-11834>.

- [196] S. Urquhart, A. P. Hitchcock, R. Priester, and E. Rightor, “Analysis of polyurethanes using core excitation spectroscopy. part ii: Inner shell spectra of ether, urea and carbamate model compounds”, *Journal of Polymer Science Part B: Polymer Physics*, vol. 33, no. 11, pp. 1603–1620, 1995.
- [197] M. Tesch, R. Golnak, F. Ehrhard, D. Schön, J. Xiao, K. Atak, A. Bande, and E. Aziz, “Analysis of the Electronic Structure of Aqueous Urea and Its Derivatives: A Systematic Soft X-Ray–TD-DFT Approach”, *Chem. - Eur. J.*, vol. 22, no. 34, pp. 12 040–12 049, 2016. DOI: [10.1002/chem.201601235](https://doi.org/10.1002/chem.201601235).
- [198] H. J. Berendsen, D. van der Spoel, and R. van Drunen, “Gromacs: A message-passing parallel molecular dynamics implementation”, *Computer physics communications*, vol. 91, no. 1-3, pp. 43–56, 1995.
- [199] N. Schmid, A. P. Eichenberger, A. Choutko, S. Riniker, M. Winger, A. E. Mark, and W. F. van Gunsteren, “Definition and testing of the gromos force-field versions 54a7 and 54b7”, *European biophysics journal*, vol. 40, no. 7, pp. 843–856, 2011.
- [200] L. J. Smith, H. J. C. Berendsen, and W. F. van Gunsteren, “Computer Simulation of Urea-Water Mixtures: 1667em A Test of Force Field Parameters for Use in Biomolecular Simulation”, *J. Phys. Chem. B*, vol. 108, no. 3, pp. 1065–1071, Jan. 2004, ISSN: 1520-6106. DOI: [10.1021/jp030534x](https://doi.org/10.1021/jp030534x).
- [201] H. Berendsen, J. Grigera, and T. Straatsma, “The missing term in effective pair potentials”, *Journal of Physical Chemistry*, vol. 91, no. 24, pp. 6269–6271, 1987.
- [202] M. C. Stumpe and H. Grubmüller, “Aqueous urea solutions: Structure, energetics, and urea aggregation”, *Journal of Physical Chemistry B*, vol. 111, no. 22, pp. 6220–6228, 2007, ISSN: 15206106. DOI: [10.1021/jp066474n](https://doi.org/10.1021/jp066474n).
- [203] G. Bussi, D. Donadio, and M. Parrinello, “Canonical sampling through velocity rescaling”, *The Journal of chemical physics*, vol. 126, no. 1, p. 014 101, 2007.
- [204] B. Hess, C. Kutzner, D. van der Spoel, and E. Lindahl, “GROMACS 4: Algorithms for highly efficient, load-balanced, and scalable molecular simulation”, *J. Chem. Theory Comput.*, vol. 4, no. 3, pp. 435–447, Mar. 2008. DOI: [10.1021/ct700301q](https://doi.org/10.1021/ct700301q).
- [205] Q. Sun, “Libcint: An efficient general integral library for gaussian basis functions”, *Journal of Computational Chemistry*, vol. 36, pp. 1664–1671, 2015. DOI: [10.1002/jcc.23981](https://doi.org/10.1002/jcc.23981). [Online]. Available: <http://dx.doi.org/10.1002/jcc.23981>.
- [206] N. Ottosson, E. F. Aziz, H. Bergersen, W. Pokapanich, G. Ohrwall, S. Svensson, W. Eberhardt, and O. Bjorneholm, “Electronic rearrangement upon the hydrolyzation of aqueous formaldehyde studied by core- electron spectroscopies”, *The Journal of Physical Chemistry B*, vol. 112, no. 51, pp. 16 642–16 646, 2008.

- [207] B Winter, R Weber, W Widdra, M Dittmar, M Faubel, and I. Hertel, “Full valence band photoemission from liquid water using euv synchrotron radiation”, *The Journal of Physical Chemistry A*, vol. 108, no. 14, pp. 2625–2632, 2004.
- [208] C. F. Perry, P. Zhang, F. B. Nunes, I. Jordan, A. von Conta, and H. J. Worner, “Ionization energy of liquid water revisited”, *The journal of physical chemistry letters*, vol. 11, no. 5, pp. 1789–1794, 2020.
- [209] R. H. Stokes, “Thermodynamics of aqueous urea solutions”, *Aust. J. Chem.*, vol. 20, no. 10, pp. 2087–2100, 1967, ISSN: 1445-0038. DOI: [10.1071/ch9672087](https://doi.org/10.1071/ch9672087).
- [210] D. Lu and G. A. Voth, “Proton Transfer in the Enzyme Carbonic Anhydrase: A *Ab Initio* Study”, *J. Am. Chem. Soc.*, vol. 120, no. 16, pp. 4006–4014, Apr. 1998, ISSN: 0002-7863. DOI: [10.1021/ja973397o](https://doi.org/10.1021/ja973397o).
- [211] P.-M. Paul, E. S. Toma, P. Breger, G. Mullot, F. Augé, P. Balcou, H. G. Muller, and P. Agostini, “Observation of a train of attosecond pulses from high harmonic generation”, *Science*, vol. 292, no. 5522, pp. 1689–1692, 2001.
- [212] M Hentschel, R Kienberger, C. Spielmann, G. A. Reider, N Milosevic, T. Brabec, P. Corkum, U. Heinzmann, M. Drescher, and F. Krausz, “Attosecond metrology”, *Nature*, vol. 414, no. 6863, pp. 509–513, 2001.
- [213] F. Krausz and M. Ivanov, “Attosecond physics”, *Rev. Mod. Phys.*, vol. 81, no. 1, p. 163, 2009.
- [214] F. Lépine, M. Y. Ivanov, and M. J. Vrakking, “Attosecond molecular dynamics: Fact or fiction?”, *Nat. Photonics*, vol. 8, no. 3, pp. 195–204, 2014.
- [215] M. Nisoli, P. Decleva, F. Calegari, A. Palacios, and F. Martín, “Attosecond electron dynamics in molecules”, *Chem. Rev.*, vol. 117, no. 16, pp. 10760–10825, 2017.
- [216] I. C. D. Merritt, D. Jacquemin, and M. Vacher, “Attochemistry: Is Controlling Electrons the Future of Photochemistry?”, *J. Phys. Chem. Lett.*, vol. 12, no. 34, pp. 8404–8415, Sep. 2021. DOI: [10.1021/acs.jpcllett.1c02016](https://doi.org/10.1021/acs.jpcllett.1c02016).
- [217] E. Goulielmakis, Z.-H. Loh, A. Wirth, R. Santra, N. Rohringer, V. S. Yakovlev, S. Zherebtsov, T. Pfeifer, A. M. Azzeer, M. F. Kling, S. R. Leone, and F. Krausz, “Real-time observation of valence electron motion”, *Nature*, vol. 466, no. 7307, pp. 739–743, Aug. 2010, ISSN: 1476-4687. DOI: [10.1038/nature09212](https://doi.org/10.1038/nature09212).
- [218] G. Sansone, F Kelkensberg, J. Pérez-Torres, F. Morales, M. F. Kling, W Siu, O. Ghafur, P. Johnsson, M. Swoboda, E. Benedetti, *et al.*, “Electron localization following attosecond molecular photoionization”, *Nature*, vol. 465, no. 7299, pp. 763–766, 2010.
- [219] F Kelkensberg, W Siu, J. F. Pérez-Torres, F. Morales, G Gademann, A. Rouzée, P. Johnsson, M. Lucchini, F. Calegari, J. L. Sanz-Vicario, *et al.*, “Attosecond control in photoionization of hydrogen molecules”, *Phys. Rev. Lett.*, vol. 107, no. 4, p. 043002, 2011.

- [220] P. Ranitovic, C. W. Hogle, P. Rivière, A. Palacios, X.-M. Tong, N. Toshima, A. González-Castrillo, L. Martin, F. Martín, M. M. Murnane, *et al.*, “Attosecond vacuum UV coherent control of molecular dynamics”, *Proc. Natl. Acad. Sci.*, vol. 111, no. 3, pp. 912–917, 2014.
- [221] W. Siu, F. Kelkensberg, G. Gademann, A. Rouzée, P. Johnsson, D. Dowek, M. Lucchini, F. Calegari, U. De Giovannini, A. Rubio, R. R. Lucchese, H. Kono, F. Lépine, and M. J. J. Vrakking, “Attosecond control of dissociative ionization of O₂ molecules”, *Phys. Rev. A*, vol. 84, no. 6, p. 063412, Dec. 2011. DOI: [10.1103/PhysRevA.84.063412](https://doi.org/10.1103/PhysRevA.84.063412).
- [222] F. Calegari, D. Ayuso, A. Trabattoni, L. Belshaw, S. De Camillis, S. Anumula, F. Frassetto, L. Poletto, A. Palacios, P. Decleva, *et al.*, “Ultrafast electron dynamics in phenylalanine initiated by attosecond pulses”, *Science*, vol. 346, no. 6207, pp. 336–339, 2014.
- [223] L. S. Cederbaum and J. Zobeley, “Ultrafast charge migration by electron correlation”, *Chemical Physics Letters*, vol. 307, no. 3, pp. 205–210, Jul. 1999, ISSN: 0009-2614. DOI: [10.1016/S0009-2614\(99\)00508-4](https://doi.org/10.1016/S0009-2614(99)00508-4).
- [224] J. Breidbach and L. S. Cederbaum, “Migration of holes: Formalism, mechanisms, and illustrative applications”, *J. Chem. Phys.*, vol. 118, no. 9, pp. 3983–3996, Mar. 2003, ISSN: 0021-9606. DOI: [10.1063/1.1540618](https://doi.org/10.1063/1.1540618).
- [225] A. I. Kuleff, J. Breidbach, and L. S. Cederbaum, “Multielectron wave-packet propagation: General theory and application”, *J. Chem. Phys.*, vol. 123, no. 4, p. 044111, Jul. 2005, ISSN: 0021-9606. DOI: [10.1063/1.1961341](https://doi.org/10.1063/1.1961341).
- [226] F. Remacle and R. D. Levine, “An electronic time scale in chemistry”, *Proc. Natl. Acad. Sci.*, vol. 103, no. 18, pp. 6793–6798, May 2006. DOI: [10.1073/pnas.0601855103](https://doi.org/10.1073/pnas.0601855103).
- [227] A. I. Kuleff and L. S. Cederbaum, “Charge migration in different conformers of glycine: The role of nuclear geometry”, *Chem. Phys.*, vol. 338, no. 2-3, pp. 320–328, 2007.
- [228] S. Lünemann, A. I. Kuleff, and L. S. Cederbaum, “Ultrafast charge migration in 2-phenylethyl-N, N-dimethylamine”, *Chem. Phys. Lett.*, vol. 450, no. 4-6, pp. 232–235, 2008.
- [229] C. Arnold, O. Vendrell, and R. Santra, “Electronic decoherence following photoionization: Full quantum-dynamical treatment of the influence of nuclear motion”, *Phys. Rev. A*, vol. 95, no. 3, p. 033425, 2017.
- [230] C. Arnold, O. Vendrell, R. Welsch, and R. Santra, “Control of nuclear dynamics through conical intersections and electronic coherences”, *Phys. Rev. Lett.*, vol. 120, no. 12, p. 123001, 2018.
- [231] M. Vacher, M. J. Bearpark, M. A. Robb, and J. P. Malhado, “Electron dynamics upon ionization of polyatomic molecules: Coupling to quantum nuclear motion and decoherence”, *Phys. Rev. Lett.*, vol. 118, no. 8, p. 083001, 2017.

- [232] M. Vacher, D. Mendive-Tapia, M. J. Bearpark, and M. A. Robb, “Electron dynamics upon ionization: Control of the timescale through chemical substitution and effect of nuclear motion”, *J. Chem. Phys.*, vol. 142, no. 9, p. 094 105, 2015.
- [233] M. Vacher, L. Steinberg, A. J. Jenkins, M. J. Bearpark, and M. A. Robb, “Electron dynamics following photoionization: Decoherence due to the nuclear-wave-packet width”, *Phys. Rev. A*, vol. 92, no. 4, p. 040 502, Oct. 2015. DOI: [10.1103/PhysRevA.92.040502](https://doi.org/10.1103/PhysRevA.92.040502).
- [234] N. V. Golubev, T. Begušić, and J. Vaníček, “On-the-Fly Ab Initio Semiclassical Evaluation of Electronic Coherences in Polyatomic Molecules Reveals a Simple Mechanism of Decoherence”, *Phys. Rev. Lett.*, vol. 125, no. 8, p. 083 001, Aug. 2020. DOI: [10.1103/PhysRevLett.125.083001](https://doi.org/10.1103/PhysRevLett.125.083001).
- [235] V. Despré, N. V. Golubev, and A. I. Kuleff, “Charge Migration in Propiolic Acid: A Full Quantum Dynamical Study”, *Phys. Rev. Lett.*, vol. 121, no. 20, p. 203 002, Nov. 2018. DOI: [10.1103/PhysRevLett.121.203002](https://doi.org/10.1103/PhysRevLett.121.203002).
- [236] M. Vacher, F. E. A. Albertani, A. J. Jenkins, I. Polyak, M. J. Bearpark, and M. A. Robb, “Electron and nuclear dynamics following ionisation of modified bismethylene-adamantane”, *Faraday Discuss.*, vol. 194, no. 0, pp. 95–115, Dec. 2016, ISSN: 1364-5498. DOI: [10.1039/C6FD00067C](https://doi.org/10.1039/C6FD00067C).
- [237] A. J. Jenkins, M. Vacher, M. J. Bearpark, and M. A. Robb, “Nuclear spatial delocalization silences electron density oscillations in 2-phenyl-ethyl-amine (PEA) and 2-phenylethyl-N,N-dimethylamine (PENNA) cations”, *J. Chem. Phys.*, vol. 144, no. 10, p. 104 110, Mar. 2016, ISSN: 0021-9606. DOI: [10.1063/1.4943273](https://doi.org/10.1063/1.4943273).
- [238] A. J. Jenkins, M. Vacher, R. M. Twidale, M. J. Bearpark, and M. A. Robb, “Charge migration in polycyclic norbornadiene cations: Winning the race against decoherence”, *J. Chem. Phys.*, vol. 145, no. 16, p. 164 103, Oct. 2016, ISSN: 0021-9606. DOI: [10.1063/1.4965436](https://doi.org/10.1063/1.4965436).
- [239] F. A. Shakib and P. Huo, “Ring polymer surface hopping: Incorporating nuclear quantum effects into nonadiabatic molecular dynamics simulations”, *J. Phys. Chem. Lett.*, vol. 8, no. 13, pp. 3073–3080, 2017.
- [240] J. Lu and Z. Zhou, “Path integral molecular dynamics with surface hopping for thermal equilibrium sampling of nonadiabatic systems”, *J. Chem. Phys.*, vol. 146, no. 15, p. 154 110, 2017.
- [241] Y. Shakyia, R. Welsch, L. Inhester, and R. Santra, “Capturing electronic decoherence in quantum-classical dynamics using the ring-polymer-surface-hopping-density-matrix approach”, *Physical Review A*, vol. 107, no. 6, p. 062 810, 2023.
- [242] G. A. Worth, M. H. Beck, A. Jäckle, and H.-D. Meyer, *MCTDH Package Version 8.4*, 2007.

- [243] V. Svoboda, R. Michiels, A. C. LaForge, F. Stienkemeier, P. Slavíček, and H. J. Wörner, “Real-time observation of water radiolysis and hydrated electron formation induced by extreme-ultraviolet pulses”, *Science Advances*, vol. 6, no. 3, eaaz0385, 2020.
- [244] C. Arnold, C. Larivière-Loiselle, K. Khalili, L. Inhester, R. Welsch, and R. Santra, “Molecular electronic decoherence following attosecond photoionisation”, *J. Phys. B: At. Mol. Opt. Phys.*, vol. 53, no. 16, p. 164 006, Jun. 2020, ISSN: 0953-4075. DOI: [10.1088/1361-6455/ab9658](https://doi.org/10.1088/1361-6455/ab9658).
- [245] M. Vacher, J. Meisner, D. Mendive-Tapia, M. J. Bearpark, and M. A. Robb, “Electronic control of initial nuclear dynamics adjacent to a conical intersection”, *J. Phys. Chem. A*, vol. 119, no. 21, pp. 5165–5172, 2015.
- [246] T. T. Luu, Z. Yin, A. Jain, T. Gaumnitz, Y. Pertot, J. Ma, and H. J. Wörner, “Extreme-ultraviolet high-harmonic generation in liquids”, *Nature Communications*, vol. 9, no. 1, p. 3723, 2018, ISSN: 2041-1723. DOI: [10.1038/s41467-018-06040-4](https://doi.org/10.1038/s41467-018-06040-4). [Online]. Available: <http://www.nature.com/articles/s41467-018-06040-4>.
- [247] Y.-P. Chang, Z. Yin, T. Balciunas, H. J. Wörner, and J.-P. Wolf, “Temperature measurements of liquid flat jets in vacuum”, *Structural Dynamics*, vol. 9, no. 1, p. 014 901, 2022.